Ministry of Higher Education and Scientific Research
Hassiba Benbouali University of Chlef
Faculty of Technology
Department of Mechanical Engineering

THESIS

To obtain the degree of "DOCTORATE OF SCIENCE"

In Mechanical Engineering

NUMERICAL SIMULATION OF HEMODYNAMICS IN AORTIC ANEURYSM AND COARCTATION OF THE AORTA: GEOMETRIC PARAMETERS EFFECT

SIMULATION NUMERIQUE DE L'HEMODYNAMIQUE AU NIVEAU D'UN ANEVRISME ET LA COARCTATION DE L'AORTE : EFFET DES PARAMETRES GEOMETRIQUES

By
Djelloul BELKACEMI

April 27, 2023,

DOCTORAL COMMITTE:

BELALIA Azeddine	MCA	UHB-Chlef	President
MERIEM BENZIANE Madjid	Professor	UHB-Chlef	Examinator
TOUAIBI Rabah	MCA	UDB-Khemis Miliana	Examinator
BOUKLI HASSAN Fouad	Professor	ESS-Tlemcen	Examinator
TAHAR ABBES Miloud	Professor	UHB-Chlef	Supervisor
LARIBI Boualem	Professor	UDB-Khemis Miliana	Co-Supervisor

Dedications

Dedicated to

My dear Parents

My Wife and my Child

My Brothers,

And My Sisters…

Acknowledgement

First I would like to deeply thank Professor Tahar Abbes Miloud and Professor Laribi Boualem for giving me the opportunity to work under their supervision.

Special thanks to all the biomechanics group members in Politecnico Di Milano; special thanks to Professor Alberto Redaelli for giving me the opportunity to join his team as an invited PhD student and spend nine months in the lab, Doctor Filippo Piatti and Doctor Francesco Sturla for their support.

I wish also to thank Doctor Mohammad Al-Rawi from Center for Engineering and Industrial Design, Waikato Institute of Technology (Hamilton, New Zealand), and Professor Ahmed Al-Jumaily from the Institute of Biomedical Technologies, Auckland University of Technology (Auckland, New Zealand) for their continuous help.

I would like to express my gratitude to MD. Sofiane Bachene from "Centre d'Imagerie Médicale" (Radiologie, Cheraga, Algiers, Algeria), for the clinical data and the data facilities.

Finally, I would like to warmly thank all my friends and colleagues.

Djelloul Belkacemi
Algiers, 27Th April 2023

Abstract

Cardiovascular diseases could affect children as they can affect elderly persons, they could be either acquired or congenital. The mortality rate from cardiovascular disease is higher in middle- and low-income countries compared to developed countries. In Algeria studies related to the management of cardiovascular diseases, the integration and the use of the newest technologies in the management of patients are still lacking. Computational fluid dynamic (CFD) methods present the advantage of giving the possibility to investigate non-invasively the cardiovascular disease and consequently present a good tool for clinicians. With the development of computing capabilities, high-performance calculations and medical imaging technologies, the use of computational fluid dynamic models in clinical use gained attention. Two diseases are studied in this thesis, namely abdominal aortic aneurysm AAA and aortic coarctation CoA. Using CFD the effect of asymmetry of AAA is studied. A detailed parametric analysis of flow dynamics using five virtual AAA models was performed. Flow behaviour and wall shear stress derivatives (time-averaged wall shear stress TAWSS, and oscillating shear stress OSI) were investigated. Secondly, an investigation of the co-localization and relationship between intraluminal thrombus ILT and WSS-based hemodynamic parameters (TAWSS, OSI, Transversal WSS transWSS, relative residence time RRT and Endothelial cell activation potential ECAP) was carried out. Computed Tomography CT data of three AAA patients were used. The model was validated against in-vitro data and a new approach was suggested to predict ILT deposition and growth based on WSS indexes in the thin and thick ILT areas. Finally, a workflow combining *in-vivo* (4D flow) and *in-silico* (CFD) data in the case of patients suffering from aortic coarctation (CoA) was presented. The verification and cross-validation of the two techniques confirm CFD's robustness and its ability to mimic realistic 3D blood flow and wall parameters with high spatial and temporal resolution.

Keywords: CFD, AAA, CoA, CT scan, 4D Flow MRI, WSS derivatives, AAA Asymmetry Effect, ILT, TAWSS, OSI, RRT, ECAP, TransWSS.

Résumé

Les maladies cardiovasculaires peuvent affecter les enfants comme elles peuvent affecter les personnes âgées, elles peuvent être acquises ou congénitales. Le taux de mortalité par maladies cardiovasculaires est plus élevé dans les pays à revenu intermédiaire et faible que dans les pays développés. En Algérie, les études liées à la prise en charge des maladies cardiovasculaires, l'intégration et l'utilisation des technologies les plus récentes dans la prise en charge des patients font encore défaut. Les méthodes de dynamique des fluides computationnelles présentent l'avantage de donner la possibilité d'étudier de manière non-invasive les maladies cardiovasculaires et constituent par conséquent un bon outil pour les cliniciens. Avec le développement des capacités informatiques, du calcul haut performance et des technologies d'imagerie médicale, l'utilisation de modèles informatiques de dynamique des fluides dans les routines cliniques a attiré l'attention ces dernières années. Deux maladies sont étudiées dans cette thèse, à savoir l'anévrisme de l'aorte abdominale AAA et la coarctation aortique CoA. En utilisant la CFD, l'effet de l'asymétrie de l'AAA est étudié. Une analyse paramétrique détaillée de la dynamique des flux à l'aide de cinq modèles d'AAA virtuels a été réalisée. Le comportement de l'écoulement et les dérivés de la contrainte de cisaillement de la paroi (contrainte de cisaillement moyenne dans le temps TAWSS et l'indice d'oscillation des contrainte de cisaillement OSI) ont été étudiés. Deuxièmement, une étude de la co-localisation et de la relation entre d'une part sur le thrombus infraliminal ILT et les paramètres hémodynamiques basés sur les WSS (TAWSS, OSI, Transversal WSS TransWSS, le temps de séjour relatif des particules RRT et le potentiel d'activation des cellules endothéliales ECAP) a été réalisée. Les données de tomodensitométrie de trois patients atteints d'AAA ont été utilisées. Le modèle a été validé par rapport aux données *in-vitro* et une nouvelle approche a été suggérée dans le but de prédire le dépôt et la croissance de l'ILT sur la base des indices WSS dans les zones ILT minces et épaisses. Enfin, un flux de travail combinant *in-vivo* (IRM flux 4D) et *in-silico* (CFD) dans le cas d'un patient souffrant de coarctation aortique (CoA) ont été présentées. La vérification et la validation croisée des deux techniques confirment la robustesse de CFD et sa capacité à imiter et à reproduire des paramètres réalistes de flux sanguin et de paroi en 3D avec une haute résolution spatio-temporelle.

Mots clés : CFD, AAA, CoA, CT scan, flux 4D, dérivés des contraintes de cisaillement, effet de l'asymétrie de l'AAA, ILT, TAWSS, OSI, RRT, ECAP, TransWSS.

الملخص

يمكن أن تصيب أمراض القلب والأوعية الدموية الأطفال كما يمكن أن تصيب كبار السن ، وقد تكون مكتسبة أو خلقية. معدل الوفيات من أمراض القلب والأوعية الدموية أعلى في البلدان ذات الدخل المتوسط والمنخفض مقارنة بالدول المتقدمة. في الجزائر ، لا تزال الدراسات المتعلقة بإدارة أمراض القلب والأوعية الدموية ناقصة خاصة في استخدام أحدث التقنيات في معالجة المرضى. تقدم الطرق الديناميكية الحاسوبية للسوائل ميزة إعطاء إمكانية التحقيق في أمراض القلب والأوعية الدموية بشكل بدون تدخل جراحي وبالتالي تقدم أداة مساعدة جيدة للأطباء. مع تطور قدرات الحوسبة والحسابات عالية الأداء وتقنيات التصوير الطبي ، اكتسب استخدام النماذج الديناميكية الحاسوبية للسوائل في الاستخدام السريري الاهتمام في اخر الدراسات العلمية. تمت دراسة مرضين في هذه الأطروحة ، وهما تمدد الأوعية الدموية للشريان الأبهري البطني AAA وتضيق الشريان الأبهر (CoA).باستخدام CFD تم دراسة تأثير عدم تناسق شكل AAA و قد تم إجراء تحليل معلمي مفصل لديناميات التدفق باستخدام خمسة نماذج AAA افتراضية. تم التحقيق في سلوك التدفق ومشتقات إجهاد قص الجدار (إجهاد قص الجدار متوسط الوق TAWSS، و درجة تذبذب إجهاد القص OSI). ثانيًا ، تم إجراء تحقيق في التوطين المشترك بين الخثرة داخل لمعة الشريان ILT وعلاقتها مع معلمات الدورة الدموية المستندة إلى إجهاد القص WSS (TAWSS، OSI، transWSS Transversal WSS و وقت الإقامة النسبي RRT وإمكانية تنشيط الخلايا البطانية ECAP) حيث تم استخدام بيانات التصوير المقطعي المحوسب CT scan لثلاثة مرضى مصابين بتمدد الأوعية الدموية الأبهري البطنيAAA. تم التحقق من صحة النموذج مقابل البيانات المختبرية وتم اقتراح نهج جديد بهدف التنبؤ بترسب ILT ونموه بناءً على مؤشرات WSS في مناطق ILT الرقيقة والسميكة. أخيرًا ، تم تقديم نموذج سيرعمل يجمع بين البيانات في الجسم الحي (الرنين المغناطيسي ذو التدفق رباعي الأبعاد) والسيليكو (CFD) في حالة المرضى الذين يعانون من تضيق الأبهر(CoA) . يؤكد التحقق و من صحة الطريقتين على متانة نماذج CFD وقدرتها على محاكاة تدفق الدم الواقعي ثلاثي الأبعاد ومعلمات الجدار بدقة مكانية وزمنية عالية.

الكلمات المفتاحية :النماذج الديناميكية الحاسوبية للسوائل ،تمدد الشريان الأبهري البطيني AAA وتضيق الأبهر CoA ، بيانات التصوير المقطعي المحوسب ، التدفق رباعي الأبعاد بالرنين المغناطيسي ،مشتقات إجهاد قص الجدار ،دور عدم تناسق تمدد الشريان الأبهري البطيني.

Publications

Journal Papers

Djelloul Belkacemi, Miloud Tahar Abbes, Mohammad Al-Rawi, Ahmed M. Al-Jumaily, Sofiane Bachene MD, Boualem Laribi. Intraluminal Thrombus Characteristics in AAA Patients: Non-Invasive Diagnosis Using CFD. Bioengineering 10.5 (2023): 540.

https://doi.org/10.3390/bioengineering10050540. **Published.**

Djelloul Belkacemi , Mohammad Al-Rawi, Miloud Tahar Abbes, Boualem Laribi (2022). Flow Behaviour and Wall Shear Stress Derivatives in Abdominal Aortic Aneurysm Models: a Detailed CFD Analysis into Asymmetry Effect. CFD Letters, 14(9), 60-74.

https://doi.org/10.37934/cfdl.14.9.6074. **Published.**

Publications as collaboration on related subject during thesis

Al-Rawi, Mohammad, Ahmed M. Al-Jumaily, and **Djelloul Belkacemi**. Non-invasive diagnostics of blockage growth in the descending aorta-computational approach. Med Biol Eng Comput (2022) : 1-15.

https://doi.org/10.1007/s11517-022-02665-2. **Published.**

Indexed conference Papers

D. Belkacemi, F. Piatti, M. Tahar Abbes, A. Caimi, F. Sturla, C. Geppert, D. Giese, F. Pluchinotta, M. Carminati, S. Chouaki, B. Laribi and A. Redaelli. Combined 4D Flow MRI and CFD Simulation in Aortic Coarctation.
First International Conference on Innovation in Biomechanics and Biomaterials ICIBAB-2019. Oran, 10-11 Avril 2019.

F. Piatti*, **D. Belkacemi***, A. Caimi, F. Sturla, A. Greiser, F. Pluchinotta, M. Carminati, and A. Redaelli. On the potential of 4D Flow in guiding CFD analyses: a case study of aortic coartaction
Proceedings VII Meeting Italian Chapter of the European Society of Biomechanics (ESB-ITA 2017) 28-29 September 2017, Rome - Italy ISBN: 978-88-6296-000-7

* indicates the co-first authorship

Indexed conference papers as collaboration on related subject during thesis

Al-Rawi, Mohammad, Ahmed Al-Jumaily, and **Djelloul Belkacemi**. "Do Long Aorta Branches Impact on the Rheological Properties?."

Proceedings of the ASME 2021 International Mechanical Engineering Congress and Exposition (IMECE2021). Volume 5: Biomedical and Biotechnology. Virtual, Online. November 1–5, 2021. V005T05A032. ASME. https://doi.org/10.1115/IMECE2021-70565

Al-Rawi, Mohammad, Ahmed Al-Jumaily, and **Djelloul Belkacemi**. "Computational And Mathematical Models To Assess Early Stages Abdominal Aortic Aneurysm (Aaa) Growth "
Proceedings of the ASME 2022 International Mechanical Engineering Congress and Exposition (IMECE2022). Columbus, Ohio -USA. October 30 — November 3, 2022. https://doi.org/10.1115/IMECE2022-94139

TABLE OF CONTENTS

List of tables

Chapter 3

Chapter 6

Chapter 7

List of Figures

Chapter 1

Chapter 2

Chapter 3

Chapter 4

Chapter 5

Chapter 6

Chapter 7

Nomenclature

A
AAA: Abdominal Aortic Aneurysm
AMG: Algebraic Multi-Grid
ANN: Artificial Neural Network
AP: Activated Platelets

C
CFD: Computational Fluid Dynamics

CVD: Cardiovascular Diseases
CoA: Coarctation
C-Y: Carreau-Yasuda
CHD: Congenital Heart Diseases
CT: Computed Tomography

D
D: Diffusion Coefficient
DPM: Discrete Phase Model
D: Maximum Diameter Of The Vessel
D: Diameter Of The Vessel
Δx: Grid Spacing
Δt: Time Step

E
ECAP: Endothelial cell activation potential
EC: Endothelial cells

F
F: Force Vector
FSI: Fluid Structure Interaction
FDA: Food and Drug Administration
FVM: Finite Volume Method

G
Grid: Convergence Index GCI
G: Mass Flow Rate
G: Gravitational Acceleration

H
Ht: Hematocrit
HPC: High-Performance Computing

I
I: Identity Matrix
InvTAWSS: inverse of the TAWSS
ILT: Intraluminal Thrombus

M
M: mass
MRI: Magnetic Resonance Imaging
MRA: magnetic resonance angiography
M: Mach number

N
N: Number Of Iterations
N-S: Navier-Stokes equations
NHS: National Health Survey
NITA: Non-Iterative Temporal Progression Scheme

O
OSI: Oscillating shear index

P
P: Pressure
PDE: Partial Differential Equation
PD: Pressure Drop
PINN: Physics-Informed Neural Network
PC-MRI: Phase-Contrast MRI
PISO: Implicit Operator Splitting Pressure

Q
Q: Flow Rate

R
Re: Reynolds Number
RBC: Red Blood Cells
ROI: Region Of Interest
RRT: Relative Residence Time

S
SIMPLE: Algorithm Semi-Implicit Method for Pressure Linked Equations

T
TTE: Transthoracic Echocardiography
T: Time
TAWSS: Time-Averaged Wall Shear Stress
TransWSS: Transversal Wall Shear Stress

U
U: velocity
u fluid: velocity in the x-direction
v fluid: velocity in the y-direction
w fluid :velocity in the z-direction

V
V : Volume
VR : Vortex Ring
VENC: Velocity Encoding

W
WSS: Wall Shear Stress
WHO: World Health Organization
WSSG: WSS gradients
WBC: White Blood Cells
WSS_max: maximum WSS

General Introduction

GENERAL INTRODUCTION

According to the World Health Organization (WHO), cardiovascular diseases (CVD) are the leading cause of death in the world [1]. The mortality rate from cardiovascular disease is higher in middle- and low-income countries compared to developed countries. In Algeria in 1990 the national institute of public health (INSP) conducted a national health survey (NHS), the survey concluded that CVD represents 18.4% of the overall percentage of disease. However, a second survey was conducted in 2005 and showed that the percentage of cardiovascular diseases has exceeded 31.3%. This decrease could be explained by many socio-economic factors like the ageing of the population compared to precedent decades.

Surveys and statistical analysis are usually conducted by different institutions, hospitals, and laboratories; however, studies related to the management of CVD, the integration, and the use of the newest technologies in cardiovascular diseases are still lacking.

Despite the recent development of technological facilities in the diagnosis, treatment, and management in general in medicine and particularly in cardiovascular diseases, abdominal aortic aneurysms (AAA) remain causing a very high mortality rate, and the decision-making criterion for surgical intervention is still traditional and relies on the measurement of the AAA maximum diameter and the annual rate of progression of the AAA [2, 3]. This work is a contribution to the prediction of AAA rupture. Chapter 5 and Chapter 6 will be devoted to the hemodynamics in idealized (virtual) models of AAA, and patient-specific AAA respectively. Where the effect of the geometry (asymmetry of the aneurysm) on hemodynamic indices (Chapter 5), and the relationship and co-localization between intraluminal thrombosis ILT deposition areas and wall shear stress derivatives (Chapter 6) are investigated.

In this work, a contribution to the investigation of the potential of combining the *in-vivo* data (4D flow MRI) to guide CFD analysis was carried out. Chapter 7 will be

devoted to the study of the capacity of CFD to mimic realistic hemodynamics provided by 4D flow in patients presenting aortic coarctation.

OBJECTIVES AND OUTLINE OF THE THESIS

Computational fluid dynamics (CFD) presents a powerful, non-invasive tool to reproduce flow features in cardiovascular diseases including AAAs and CoA. Using CFD, the behavior of the blood flow under different arterial wall constructions reflecting different characteristics/development of the disease can be modeled without requiring invasively obtained experimental or field data. Flow features including velocity, vorticity, wall shear stress (WSS), and its derivatives can be obtained within the CFD model.

In abdominal aortic aneurysm (AAA) assessing the risk of rupture is extremely important to reduce mortality. Current clinical guidelines suggest considering the maximum diameter as a criterion for planning and surgical intervention; however, this approach is too simplistic and overlooks other morphological parameters that are associated with the risk of rupture. **Chapter 5** aims to study the thrombogenicity and to predict the risk of AAA rupture by taking into consideration the geometrical asymmetry of the aneurysm, studying its effect on blood flow behaviour and vortical structure, spatiotemporal, distribution of wall shear stresses (WSS), and their related parameters. To show the effect of asymmetry on blood flow dynamics and hemodynamic forces, five virtual models are constructed using five values of geometrical asymmetry ratio β ranging from β=0.2 (asymmetric model; AM) to β=1 (symmetric model; SM).

Despite advances in medical imaging and surgery, abdominal aortic aneurysm (AAA) still has high mortality. Over the last decade, the scientific community has devoted considerable research effort to assist clinicians in their decision-making to manage patients with AAA for surgical intervention. Intraluminal thrombus (ILT) is detected in most AAAs and may critically impact their development. Therefore, understanding ILT deposition, growth and its relationship with wall shear stress

derivatives is of practical importance. In **Chapter 6**, the geometries of three patient-specific models of AAA are reconstructed from computed tomography (CT) scans. CFD simulations with a pulsatile non-Newtonian blood flow (Carreau-Yasuda model) enabled non-invasive estimation of the hemodynamic parameters acting on the endothelial cells. Numerical simulations are conducted using the finite volume method with ANSYS-Fluent software. The deposition and thickness of the ILT are estimated by using an open-source software and a custom-built script. The co-localization and relationship between five WSS-based hemodynamic parameters and ILT deposition are examined.

In recent years, hemodynamic biomarkers have attracted attention to facilitate diagnosis, risk stratification and treatment of cardiovascular diseases, in particular focusing on the impact of *in-vivo* blood fluid dynamics. Computational fluid dynamics (CFD) studies provide an interesting and helpful procedure for the understanding of the hemodynamic within the region of interest, their consistency with *in-vivo* data may be hampered by the used boundary conditions and the accuracy of complex patient-specific geometries. 4D Flow MRI is the unique way to measure and visualize full 3D time-dependent *in-vivo* blood flow, but with low spatial and temporal resolution. To this aim, in **Chapter 7**, the potential of *in-vivo* data based on magnetic resonance imaging to guide and verify the reliability of numerical simulations is exploited. A workflow is presented to show the combination of *in-vivo* and *in silico* methods in the case of the management of patients suffering from aortic coarctation (CoA). 4D Flow allowed the validation of the CFD results by comparing the 3D flow field using streamline and velocity distribution in selected cross-sections planes along the aorta. Furthermore, the final aim is to compare CFD pressure drop against catheterization values and/or values estimated by Echocardiography, thus giving the CFD model high fidelity and making it able to reproduce accurate PD estimation lacking in 4D Flow data presenting aliasing in the region of CoA. In addition to the non-invasive estimation of PD, the tailored and validated CFD presents the

advantage of the measure of post-treatment PD and could help clinicians in the management of CoA patients.

To summarize; the aim of this thesis is to estimate hemodynamic indexes in two diseases related to the aorta. Idealized and realistic models of abdominal aortic aneurysm and realistic aortic coarctation are studied using computational fluid dynamics. The general objectives of the thesis are as follows:

- Help clinicians in the stratification and the management of patients with AAA by suggesting supplemental criteria for planning and surgical intervention based on CFD as a non-invasive tool (Chapter 5).

- Improve the prediction of ILT deposition and growth in AAA patients and consequently the progression and rupture of AAA based on hemodynamic indicators using CFD (Chapter 6).

- Use of medical images in CFD models (Chapters 6 and 7).

- Combine and compare CFD models with *in-vivo* data (Chapter 7).

- Herein, we sought to define a 4D Flow-based protocol to guide the CFD reproduction of CoA hemodynamics in patients presenting CoA and allow the validation of the CFD results thus giving the CFD model high fidelity and making it able to reproduce accurate reproduction of main flow behaviour and features present in the *in-vivo* data with the final aim to use the non-invasive advantage of CFD method to estimate the pressure drop presented in CoA patients in the second step.

In **Chapter 1**, a literature review of computational methods in AAA and CoA patients was carried out. This chapter reviews comprehensively the use of computational methods in the management of AAA and CoA. Papers about CFD and FSI in virtual (idealized) AAA models, medical imaging-based studies on AAA, and the

use of 4D-FLOW were detailed, and finally, the use of 4D flow-based CFD in CoA patients was summarized.

In **Chapter 2**, generalities about the cardiovascular system, and cardiovascular diseases (and specifically the two studies diseases AAA and CoA) are presented.

In **Chapter 3** the mathematical model and equations used in our simulations and in the post-processing of the results are presented. **Chapter 4** is devoted to explaining the methodology and workflow adopted to conduct the simulations.

Finally, the key findings of this thesis are discussed. The limitations and the future perspective are also presented in the general conclusion and perspectives.

Chapter 1

Literature Review:
On the use of Computational Methods in the management of AAA and CoA Patients

1.1. INTRODUCTION

The development of computing capabilities and high-performance computing (HPC) has allowed the development and emergence of computational methods in healthcare, particularly in cardiovascular diseases (CVD). These capabilities (.ie. HPC), have enabled the use of complex models that can mimic real conditions in arteries. Computational methods have emerged in the recent decade as a complementary tool to improve the understanding of the blood flow behaviour in healthy and diseased subjects. Computational methods combined with the newest medical imaging technics have allowed the development of validated and well-trusted models. The major advantage of these numerical models is their non-invasive nature, which reduces medical costs and postoperative issues.

This chapter provides a comprehensive review of the use of computational methods in the management of abdominal aortic aneurysm (AAA) patients and aortic coarctation (CoA) patients. The chapter summarizes papers on computational fluid dynamics (CFD) and fluid-structure interaction (FSI) in virtual (idealized) AAA models, medical imaging-based studies on AAA patients, the use of machine learning methods in CVD, and finally the use of 4D flow-based CFD in CoA patients.

1.2. CFD AND FLUID-STRUCTURE INTERACTION IN VIRTUAL AAA MODELS

Several studies were carried out and evaluated numerically the blood flow and hemodynamic parameters through AAA. For parametrical studies, it was found that Virtual (idealized) aneurysm models are more useful compared to realistic patient-specific geometries [4-13]. The effect of aneurysm shape on hemodynamic parameters was studied (see Figure 1.1 [13] as an illustration).

Starting with CFD studies where a no-slip boundary condition is imposed at the wall supposing that it is rigid. In fact, the wall of the AAAs becomes stiffer following the loss of elastin [14] and their compliance is nearly negligible compared to the healthy aorta [15]. This hypothesis was adopted in the majority of the studies concerning AAA [5-8, 16-46]. Whilst in other studies the elasticity effect of the aortic wall was considered using fluid-structure interaction (FSI) [6-8, 10, 22, 47-53].

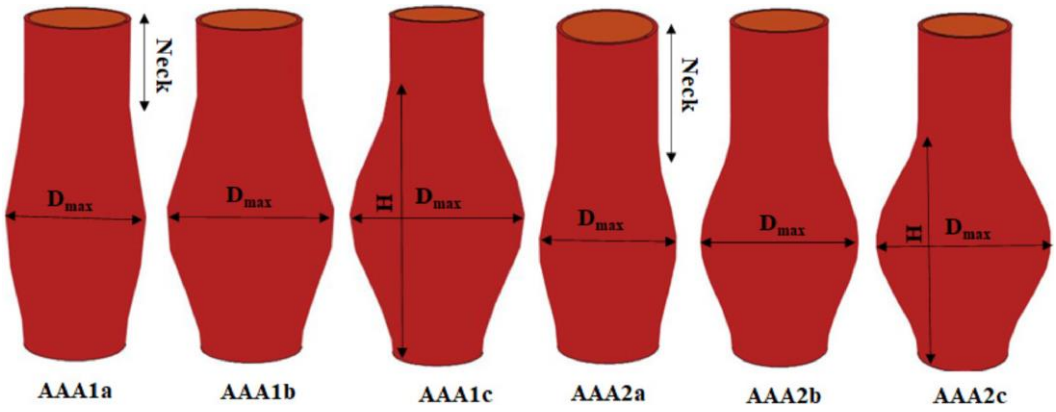

Figure 1.1: Effect of shape of AAA was studied in Philip, Nimmy Thankom et al 2022 [13].

Finol et al 2003-a [16] conducted a CFD study to investigate the hemodynamic change in AAA; in their second study, Finol et al 2003-b [17] the relationship between WSS derivatives and hemodynamics was explored. Peattie, et al 2004 [5] investigated the difference in hemodynamic parameters between small and large idealized models of AAAs. In this work, it was found that turbulence increases in larger aneurysms compared to smaller aneurysms which may increase WSS values and consequently the risk of rupture. Khanafer conducted a study in 2007 [18] where the effect of rest and exercise conditions on fluid flow, WSS and pressure was examined. In O'rourk et al 2008 [19] a comparison between CFD and *in-vivo* data was conducted and the relationship between vortex structure and thrombosis was investigated. The best agreement was found using a simple laminar flow model in CFD simulations. Yosuke Otsuk et al in 2013 [20] in an article entitled "preliminary computational hemodynamics study of double aortic aneurysm under multistage surgical procedures: an idealized model study" numerical simulations were carried out on idealized models with rigid walls in the presence of double aneurysms.

For healthy aorta and small aneurysms modelling the flow as laminar flow is desirable, however, for large aneurysms, the transitional model is preferable according to Vinoth et al 2015 [21]. Javadzadegan et al 2017 [10] conducted a study using idealized models with a rigid wall; the effect of suprarenal vs infrarenal positions was investigated. The results confirm that the suprarenal AAA promotes thrombosis initiation.

Wang et al 2011 [22] conducted a Fluid-structure interaction (FSI) study on the idealized AAA models. The effect of blood viscosity on flow behaviour through

different compartments of aneurysms and its effect on wall displacement and WSS were studied.

Fraser et al 2009 [7] studied the difference between rigid wall assumption (CFD) and FSI modelling in an axially symmetric idealized model of AAA, the error between the two models was found negligible in terms of peak Von Mises stress. These results suggest that the incorporation of CFD modelling is sufficient for mechanical modelling and the evaluation of current rupture probability. A numerical investigation of the fluid-structure interaction of ten idealized AAA models was carried out by Scotti et al 2005 [6] to study the effect of asymmetric bulging and wall thickness. Velocity, pressure and wall displacement were investigated in this study.

1.3. MEDICAL IMAGING BASED STUDIES ON AAA

With the development of medical imaging facilities, several imaging-based numerical studies were carried out with the aim to mimic the realistic flow and understand its behaviour through AAAs. Patient-specific geometries are used based on CT scans or MRI imaging. Computational models were developed to help clinicians in the management of patients suffering from cardiovascular disease including AAA (see an example of CFD simulation based on CT scan images in Figure 1.2).

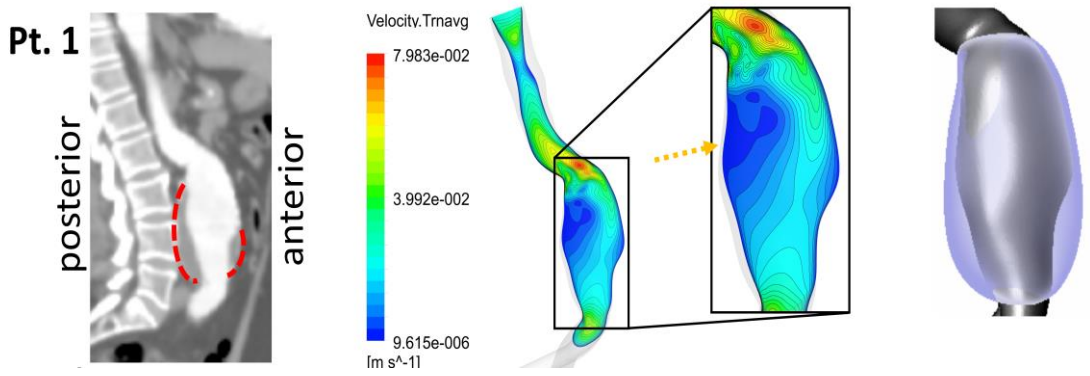

Figure 1.2: Example of CT scan-based simulation in patient with AAA. Right sagittal CT images with dashed red lines showing outer ILT walls (left column). Time-averaged velocity contours at the right view of the mid-sagittal section and magnified in the AAA sac region (middle column); computational domain (grey) and ILT deposition (purple) of AAAs patients in the rightmost column (For more details see chapter 6).

Les et al 2010 [27] conducted a study on a cohort of eight AAA patients with the aim to understand the effect of exercise and rest conditions on hemodynamic parameters and consequently on rupture risk, magnetic resonance imaging and computational fluid dynamics were used in this study. Similarly, Suh et al 2011 [25] used MRI and CFD, in this study, it is suggested that during exercise the augmentation of mean infrarenal may reduce chronic flow stasis that may influence wall thrombus, aneurysm growth and damage and degradation of the aortic wall. Sinead Kelly and Malachy O'Rourke carried out in 2012 [52] a numerical simulation work using the open source code OpenFOAM to compare the different simulation techniques of AAAs with the geometries of three specific patients. The results obtained show that the simulation of the solid part alone is adequate to predict the maximum stresses exerted on the wall of the aneurysm; on the other hand, FSI simulations must be carried out for a better prediction of the WSS. The authors at the end of the article mentioned a study based on a large population must be carried out to validate these results.

Z Macek & al in 2013 [54] in their article entitled "wall shear stress and endothelial cells dysfunction in the context of abdominal aortic aneurysm" suggested that the formation of AAAs is multifactorial and WSS and wall elongation applied directly to the cells of the wall regulate the remodelling of the wall. The effect of mechanical stimulation leads to dysfunction of endothelial cells (EC), in AAAs this phenomenon plays an important role where damage to EC is associated with changes in the endothelial permeability and increased local inflammation, which is the initial stage in the formation of AAAs and their expansion. This study presents results concerning the influence of WSS on EC dysfunction. The results obtained show that high WSS levels are apparently not the only cause of AAA pathology and suggest that WSS gradients (WSSG) play a key role in this disease. The direct study of spatiotemporal changes in WSSGs is a challenge, a discrete phase model (DPM) was developed; this model allows a good evaluation of WSSGs.

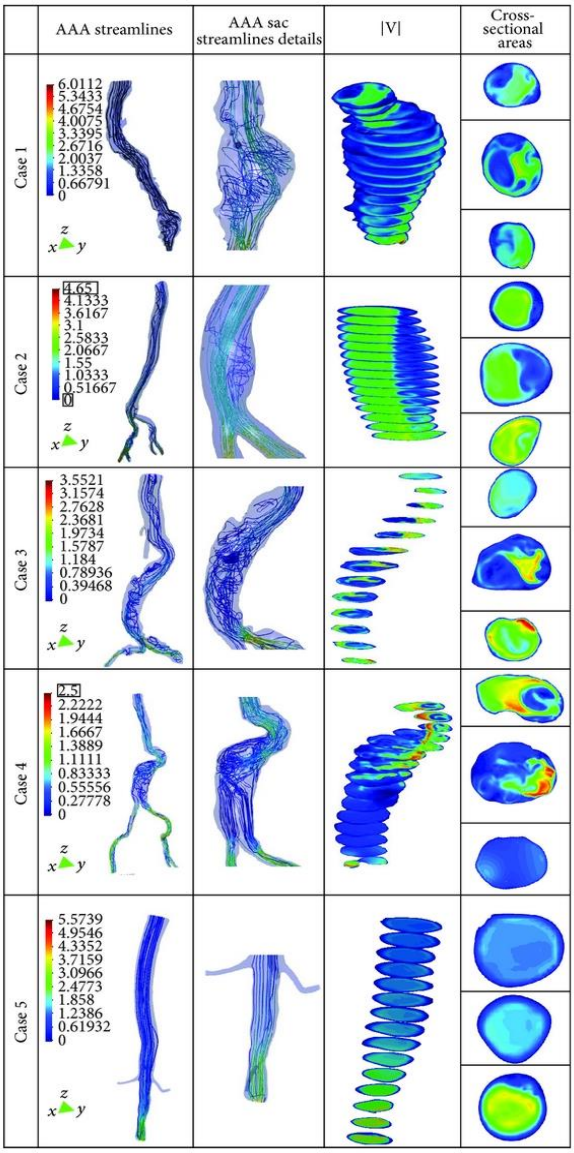

Figure. 1.3: Example of CT scan based CFD simulations on five AAA patients (from Soudah et al 2013 [38]).

Eduardo Soudah & al 2013 [38] published an article whose objective is to find a correlation between on one hand the geometric parameters of AAAs and on the other hand WSS, flow dynamics in aneurysms, intraluminal thrombosis (ILT), and rupture of the wall of the aneurysms. CFD simulations of 3D rigid wall models of five AAA by patients were used (see Figure 1.3). The results obtained show that the WSSmax values in an infrarenal AAA are higher than those in a normal aorta and their values are not directly related to the maximum diameter, which shows the need for the use of real geometries for a better evaluation of the risk of rupture of the aneurysm. Therefore, relying on one or two geometric parameters only to

determine this risk of rupture precisely is insufficient. AAA rupture is a complex situation dependent on maximum diameter, internal pressure, wall stresses, asymmetry, secularity index, ILT thrombosis, and tortuosity among other parameters.

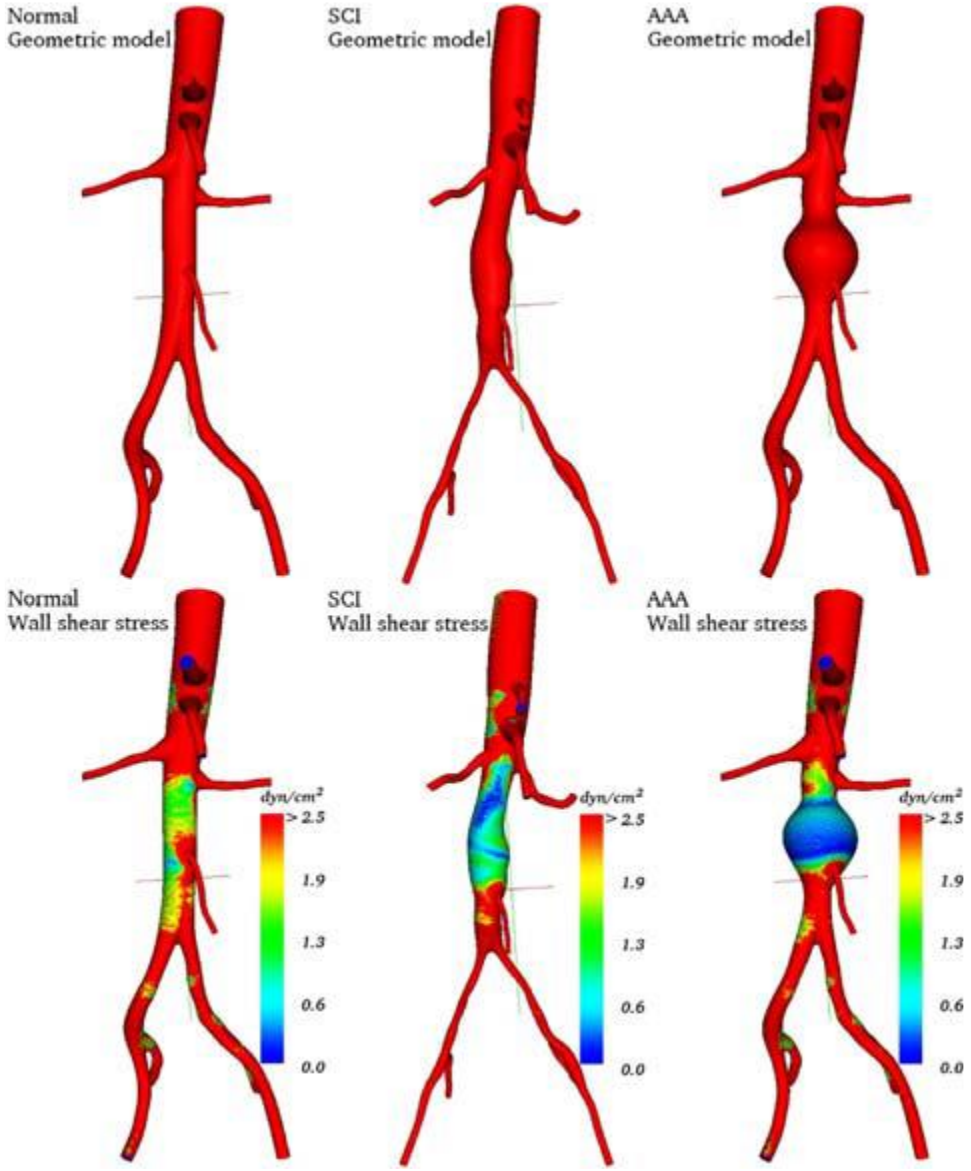

Figure. 1.4: 3D models (top) and WSS in healthy, spinal cord injury (SCI) and AAA subjects [55].

Shabestari et al 2011 [42] in their paper, a three-dimensional abdominal aorta aneurysm model was constructed based on CT-scan/angiography images. The results of this investigation indicate the direct relation between the aneurysm diameter and pressure. Arzani et al 2014-a [23] studied the changes in blood topology during rest and exercise conditions using five patient-specific AAA geometries based on MRI

data with diameters <5cm. In this work it was concluded that the overall residence time is reduced in exercise conditions in all aneurysms. The behaviour of the jet of blood penetrating into the aneurysm during systole is the main factor that is responsible of the change in flow topology from rest to exercise.

In addition to the studies cited above [18,23,25,27], Dalman et al 2006 [55] conducted a study on the effect of exercise on hemodynamic parameters and concluded that exercise reduces the progression of the small AAA (see figure 1.4).

Wan Naimah & al [56] in an article published in 2014 entitled "A perspective review on numerical simulation of hemodynamics in aortic dissection". In this review work, the team made a synthesis of the FSI fluid-structure interaction and rigid wall methods and the effect of taking into account or not the flexibility of the wall on the wall stresses and on the dynamics of the wall.

1.4. PC-MRI AND 4D-FLOW TO MIMIC REALISTIC RESULTS

Whilst available since the 90s, it is mainly used for research purposes in the recent decade 4D flow CMR (also called 4D PC-MRI and 4D flow MRI). During the last decade, 4D flow MRI emerges as a promising tool to visualize and quantify blood flow (in all 3 directions + time). Additionally, 2D PC-CMR allows the visualization and acquisition of spatial distribution of velocity in a two-dimensional plane (2D).

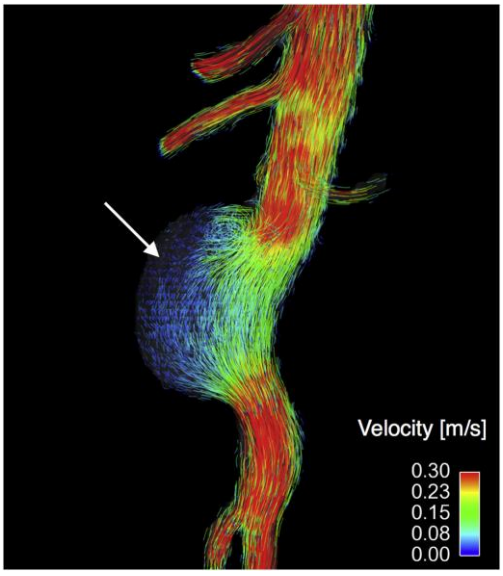

Figure. 1.5: Pathline visualization in AAA patient using 4d flow MRI (from Ziegler et al 2019 [57]).

The development of these technics offers access comprehensively to *in-vivo* flow data. The validation of CFD and FSI models against *in-vivo* data and the use of realistic and patient-specific boundary conditions become possible (see an example in Figure 1.5 from Ziegler et al 2019 [57]). The emergence of these new medical imaging technics allowed also their use in the acquisition and the post-processing of *in-vitro* studies (see an example of 4D flow MRI used phantom models of AAA in figures 1.6 a and b (Wang et al 2016 [58]).

a)

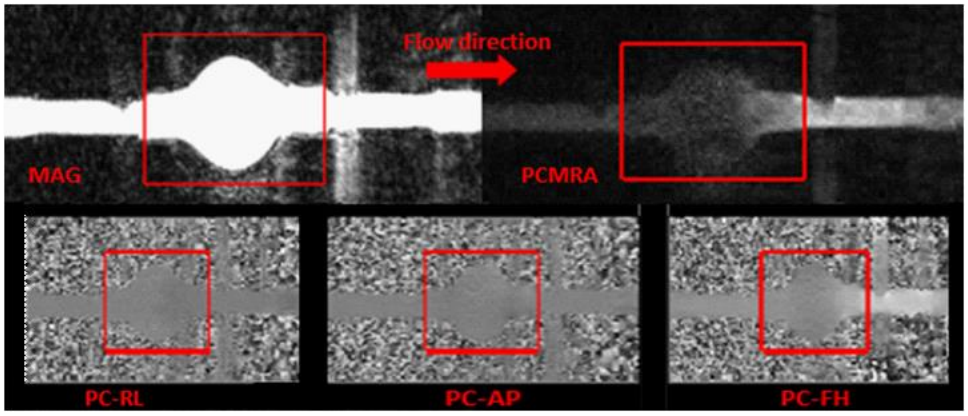

b)

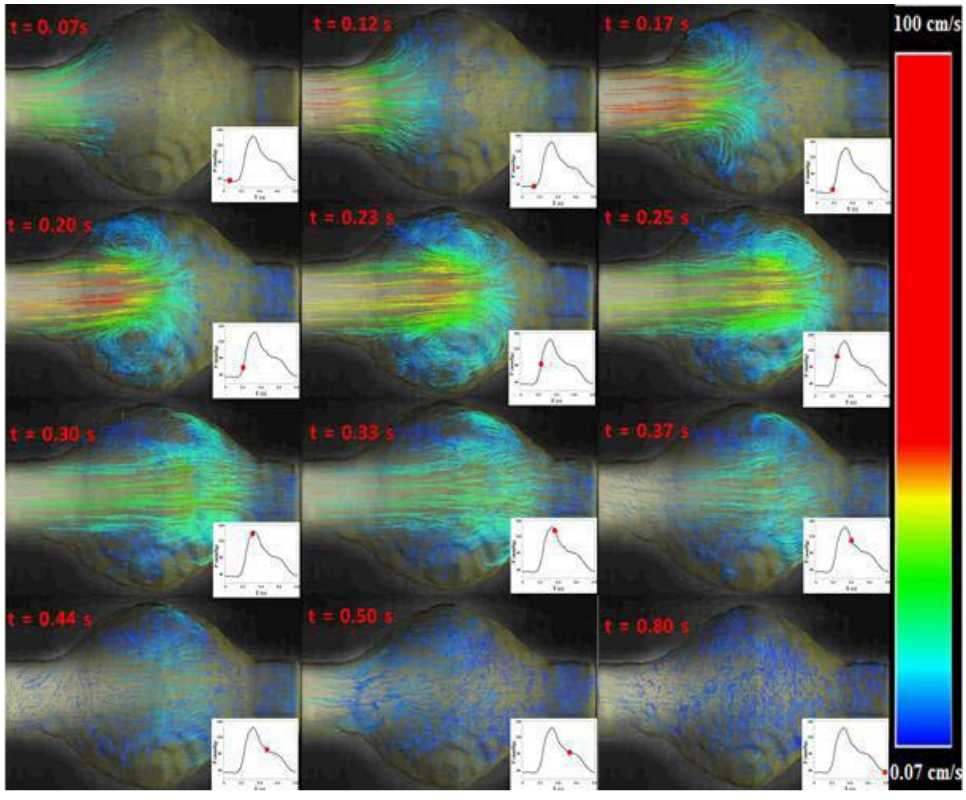

Figure. 1.6: a) Examples of images acquired by 4D flow MRI for an axisymmetric AAA phantom. b) Evolution of velocities fields over time measured by 4D flow MRI for the case of an axisymmetric AAA phantom in silicone [58].

David Hardman & in 2013 [41] in their work presented a comparison between three input condition data in an AAA which are (i) a single component velocity extracted from MRI imaging (ii) a 2D velocity profile with an axial velocity component (iii) 2D velocity profile with 3 velocity components. The results found show that the entrance velocity based on central line velocity obtained for example by Doppler ultrasound leads to very amplified hemodynamic conditions and it is not recommended, a condition at one velocity component is sufficient when we are interested in the general flow characteristics and spatial distribution of WSS wall shear stresses. It is preferable to use a 2D MRI velocity profile with three velocity components in the case where the interest is in the residence time of the particles, the WSSs, and the oscillation shear index. Note that the models used to assume that the wall is rigid.

David Hardman & al [59] published a very interesting article in 2013 following his PhD thesis at the University of Edinburgh. D Hardman counts the biological activity to which the wall of the aorta is exposed and sites the inflammation, the degradation of the matrices metalloproteinase of the extracellular matrices. This process is orchestrated by monocytes affecting the aorta and damaging and weakening the wall and making it vulnerable to rupture. This work deals with the deposition of monocytes using turbulence modelling by large Eddy simulation (LES) and uses a DPM (discrete phase model) under Ansys Fluent. The fluid is assumed as a multiphase medium, the model has been applied first to idealized AAA models and then to specific patient aneurysm geometries, and the wall is assumed to be rigid. The velocity profile at the entrance is 3-component based on MRI data. The results obtained showed that the deposits of monocytes become significant from a critical diameter of AAA equal to 1.8 times the diameter of the entrance of the aneurysm and the adhesion of monocytes is observed in the proximal part for the small aneurysms and in the distal part with the expansion of the AAA (as the expansion progresses). The infiltrations of the monocytes responsible for the weakening of the wall occur in a heterogeneous way. The peak residence time of monocytes increases with the size of the aneurysm sac and the average residence time increases rapidly as soon as the sac exceeds 1.8 times the diameter of the AAA entrance, which

suggests that this is the critical size from which the infiltration of monocytes and the degradation of the wall increases in a significant way.

Ethan Okung et al 2011 [60] carried out an experimental work (*in-vitro*) in a complex patient-specific AAA geometry using real boundary conditions (in rest and in exercise conditions) taking into account the iliac arteries, subsequently, an *in-silico* model was used and the simulation results were compared with the experimental results. A high degree of agreement was found between the experimental measurements and simulated results in all of the pressure and flow waveform shapes and magnitudes.

1.5. CFD IN CLINICAL APPLICATION AND ARTIFICIAL INTELLIGENCE EMERGENCE

The development of computing capabilities and high-performance computing allowed the use of more complex numerical models with lower time consumption in the calculation to reproduce realistic hemodynamic data from computational fluid dynamic models leading for the first time the Food and Drug Administration (FDA) approved for the first time the use of computational models in the clinical use [61].

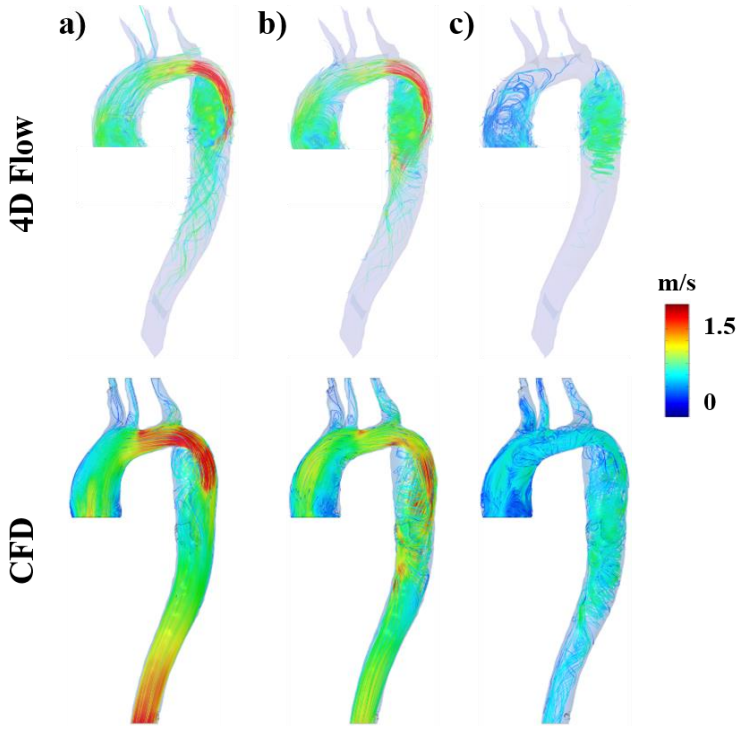

Figure. 1.7. Streamlines computed at different time frame CFD and 4D flow data (from our paper Piatti & Belkacemi et al 2017 [62]).

The numerical models suffer from uncertainty in boundary conditions and blood rheology models. On the other hand, the *in-vivo* data (4D flow) suffer from artifact errors, measurement noise and low spatiotemporal resolution which make the measurement of important hemodynamic indicators not sufficiently accurate (measurement of WSS for example). Chapter 7 have shown in the case of CoA patient, how the combination of *in-vivo* data represented by 4D flow MRI and *in-silico* data represented by CFD simulations are interesting from a clinical point of view in the management of cardiovascular diseases (see figure 1.7 [62]).

The recent development in artificial intelligence models (artificial neural network ANN, physics-informed neural network PINN) gained attention in the last few years. Arzani et al 2021 [63] show how PINN could be a good solution to improve WSS estimation in cardiovascular disease in cases where inlet and outlet boundary conditions were not available. An example of a stenosed artery is shown in Figure 1.8 showing how PINN could be used to obtain an accurate estimation of blood flow near the wall (WSS for example).

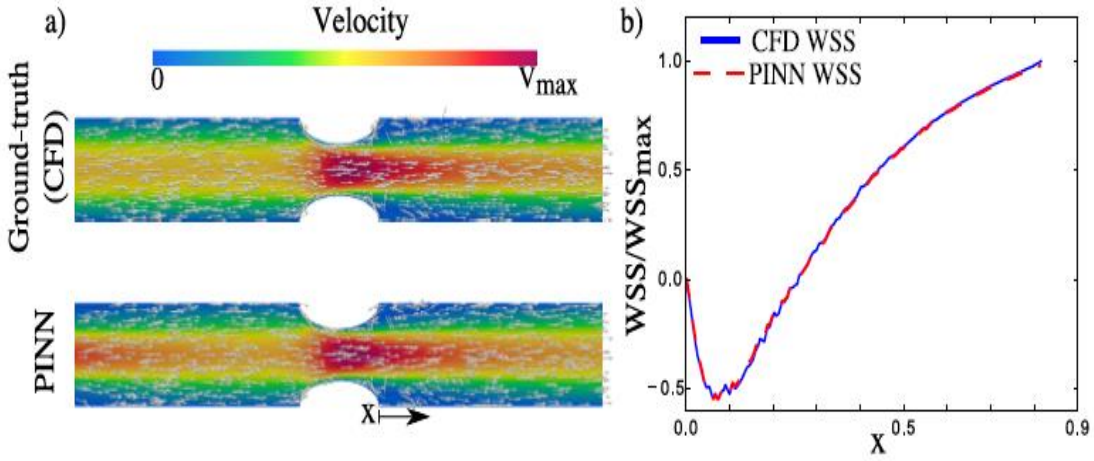

Figure. 1.8: velocity vectors results in the 2D stenosis model and WSS results in the region distal to the stenosis are compared between the CFD and PINN models. Inlet and outlet boundary conditions were not specified in the PINN problem. From Arzani et al 2021 [63].

1.6. ILT IN AAA: ON THE USE OF CFD METHODS

Despite the inexact role of ILT in AAA rupture; the detection of ILT and the prediction of its growth are important for clinicians in the treatment and management of AAA patients. The fact that AAA is often associated with the deposition of blood clots and

cell debris in the ILT, as well as the breakdown of connective tissue in the wall, which plays an important role in the rupture and remodeling of the wall, makes the fluid dynamics in AAA, including the evolution of velocity and wall shear stress (WSS) based hemodynamic parameters, a very promising index to improve the prediction of rupture and ILT accumulation. This has led many studies to investigate the relationship between WSS-based indicators and ILT deposition and growth.

The mechanism of ILT formation suggested by Biasetti et al 2011 [43] is in relation to the vortex formation in the neck creating activated platelets (AP) transported through the aneurysm sac and then released at the distal zone of AAA which then adhere to the wall in this area. The wall shear stress derivatives are hemodynamic parameters acting on the endothelial cells. The nexus between WSS derivatives and ILT deposition and growth gained attention with the aim to understand and predict ILT deposition and growth and consequently AAA progression and rupture.

In addition to their thrombogenic function, the endothelial cells are also the mechano-detecting elements which detect the local blood flow conditions and induce autocrine stimulation. Wall shear stress (WSS) expresses the friction which induces a tangential force and links blood flow to the vessel wall. *In-vivo* and *in-vitro* studies demonstrate the destructive effect of low and oscillatory WSS on endothelial function and their effect on intimal thickening. Unlike the situation where there is a low magnitude of WSS, under high physiologic WSS, the ECs are aligned to the flow direction [64]. Regions of low WSS are also associated with rupture and expansion sites of the AAAs [65], whereas, at high levels of WSS, the atheroprotective endothelial phenotype decreases the expression of the vasoconstrictor. Furthermore, WSS and their derivatives are also correlated to ILT deposition and growth in cardiovascular diseases including AAAs [24, 30, 32, 37, 66-70]. Along with its inexact role in AAA rupture, the ILT process is very complex. The detection and prediction of ILT deposition and growth are of importance for clinicians in the treatment and management of AAA patients and were of significant interest in recent studies [66]. In chapter 6 an investigation is carried out to study the relationship between WSS derivatives and ILT deposition estimated by segmentation from DICOM images. Wall shear stress and related hemodynamic parameters are

obtainable non-invasively using CFD simulations, which is an important advantage from the clinical point of view.

Forneris et al. 2020 [71] suggested a new parameter combining time-averaged wall shear stress (TAWSS) intraluminal thrombus (ILT) thickness based on CFD analysis and wall stress based on strain analysis to score regions and predict regions of possible rupture. This study was limited to one ruptured patient, despite this limitation the study showed an interesting effective application of numerical methods in the management of cardiovascular disease including AAA (see Figure 1.9).

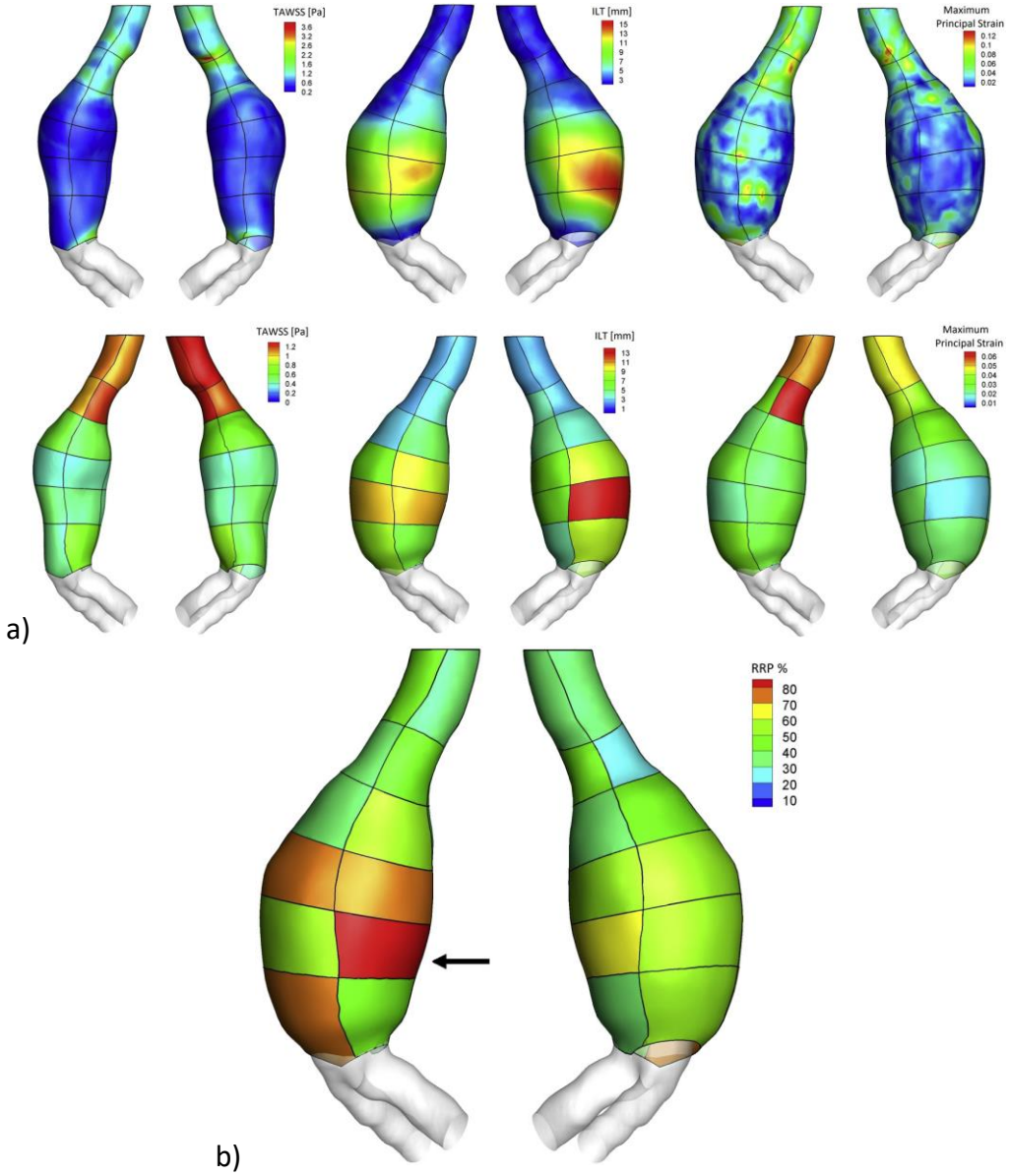

Figure. 1.9: Regional Rupture Potential (*RRP*) index computed based on TAWSS, ILT and maximum strain in AAA patient (from Fourneris et al 2020 [71]) the black *arrow* indicates the site of rupture.

1.7. CONCLUSION

The main objective of using numerical simulations in the study of AAA is to understand the hemodynamics in this disease and consequently define the relationship between on one hand geometric parameters of AAAs and on the other hand wall shear stress derivatives and wall strain. As mentioned earlier the Food and drug administration (FDA) approved the CFD method in clinical use [61]. Additionally, Numerical methods present the advantage of giving the possibility to investigate non-invasively cardiovascular disease including AAAs and consequently present a good tool for clinicians in the management of patients and to better stratify the risk for AAA rupture by determining additional criteria to help surgeons make clinical decisions regarding the surgical intervention of patients with AAA. The current clinical guidelines suggest considering the maximum diameter as a criterion for planning and surgical intervention; this approach is too simplistic and numerical methods could help in addition to overlook other morphological parameters that are associated with the risk of rupture.

The main aim of the other studies is to find an additional and new criterion for planning and surgical intervention using CFD as a non-invasive tool. In our thesis, the effect of aneurysm's asymmetry using idealized models is studied in Chapter 5 and in Chapter 6 realistic models of abdominal aortic aneurysm are used to investigate the relationship between IL and WSS derivatives (TAWSS, OSI, RRT, TransWSS and ECAP) and finally, patient-specific aortic coarctation is investigated in chapter 7 using computational fluid dynamics based on 4D flow MRI data. The simulation results are compared and validated with *in-vivo* data.

Chapter 2

Cardiovascular Diseases

2.1. INTRODUCTION

As it has been shown in the general introduction, According to the World Health Organization (WHO), despite the development of medical imaging and the use of the most efficient technologies in the sector of health care, cardiovascular diseases (CVD) are the leading causes of death in the world [1]. The middle- and low-income countries compared to the developed countries present a higher mortality rate from CVD (see Figure 2.1).

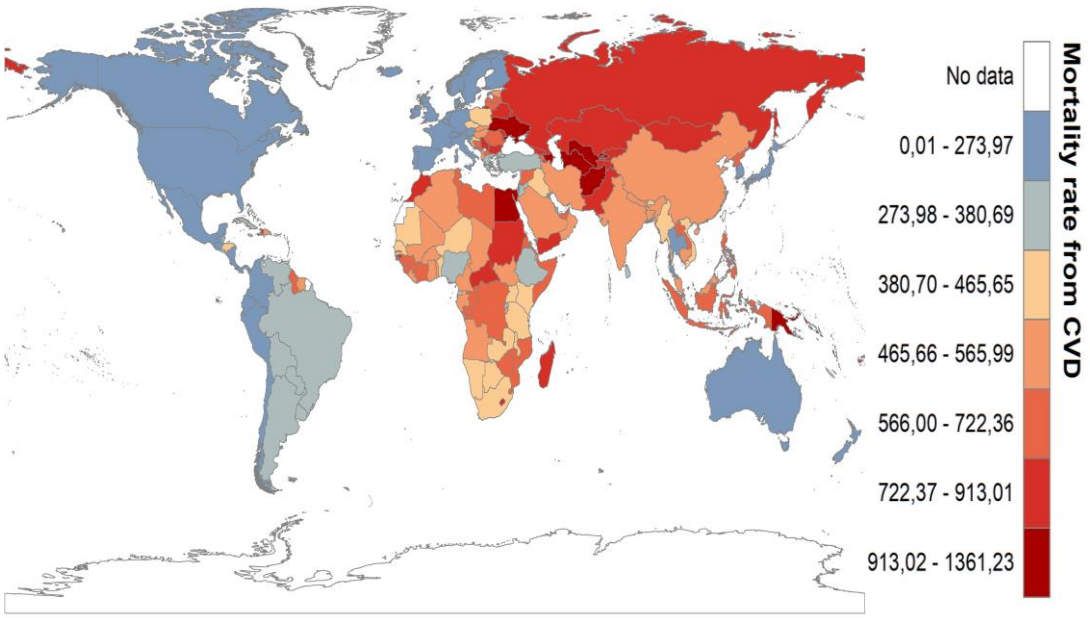

Figure. 2.1. Mortality rate from cardiovascular disease (per 100,000) by countries – 2013–2017 (adapted from [1]). Dark red color show regions with highest mortality rate and blue correspond to regions with lowest mortality rate.

In 2016 the INSP conducted a new national survey to estimate the medical causes of death in Algeria. The results of this study have shown that cardiovascular diseases are the leading cause of medical death (21.3%) (See Figure 2.2). In 2021 the INSP pointed out that CVD represented 34 % of overall causes of death [72].

This Chapter presents the main general information about, the cardiovascular system; cardiovascular diseases and focuses specifically on two diseases that affect the main artery in the cardiovascular system which is the aorta and which we will

study in our thesis .ie. Abdominal aortic aneurysm (AAA) and aortic coarctation (CoA).

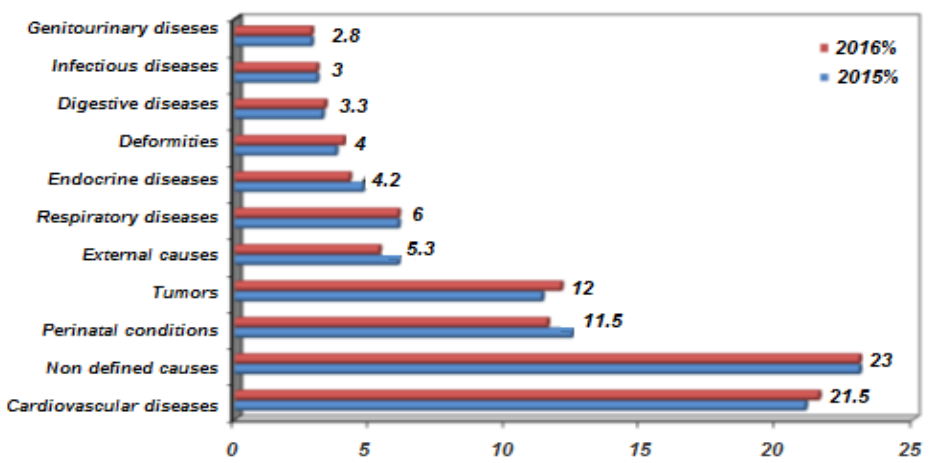

Figure. 2.2. Distribution of the main medical causes of death in Algeria (Adapted from INSP medical survey 2016 [73]).

2.2. CARDIOVASCULAR SYSTEM

The main role of the cardiovascular system is the irrigation, oxygenation, and transportation of nutrients to tissues and organs, as well as the waste products that are transported from the organs back to the heart and subsequently to the lungs. The circulatory system consists of two vascular loops: pulmonary circulation, which carries blood between the heart and the lungs, and systemic circulation, which carries blood between the heart and the organs. The pulmonary circulation simultaneously supplies the right and left lungs, and the systemic circulation simultaneously supplies the upper and lower parts of the body (see Figure. 2.3).

The cardiovascular system has two parallel networks of vessels: arteries and veins. The arteries constitute the network of vessels delivering oxygen, and the veins constitute the so-called "return" network of blood to the heart and the lungs.

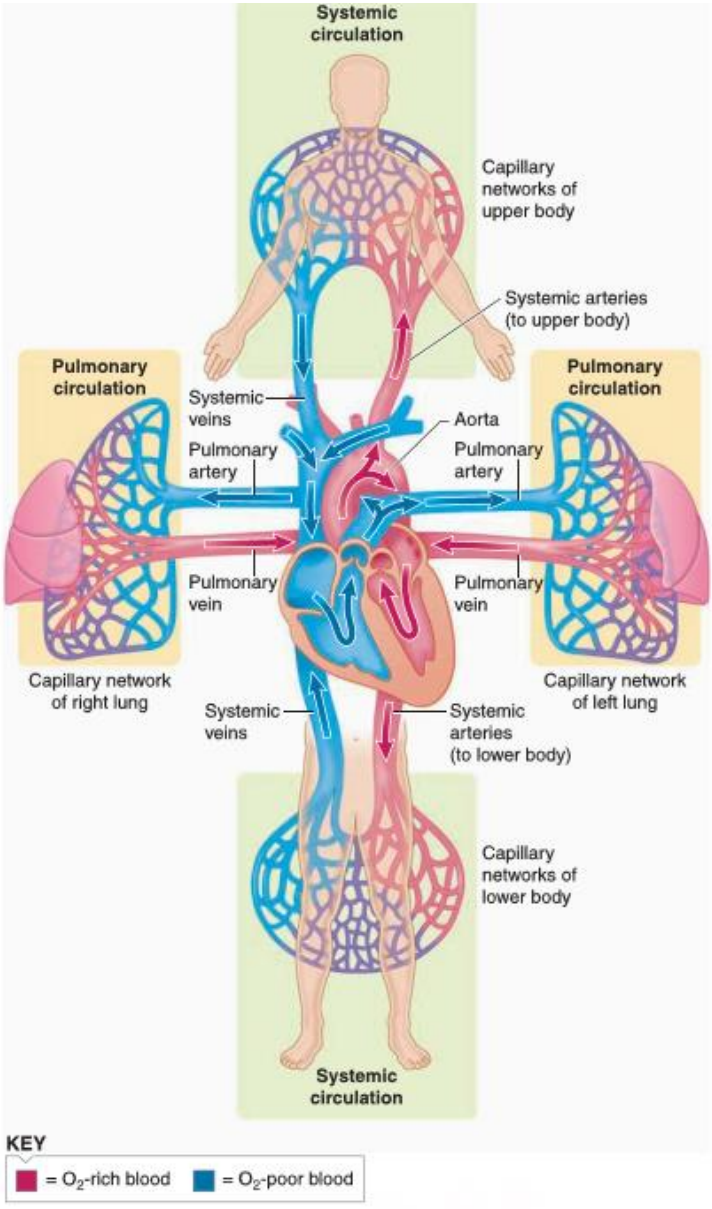

Figure. 2.3. Pulmonary and systemic circulation [74]. Red color relates to blood rich in oxygen O2 and blue color relates to blood poor in O2).

The study of the cardiovascular system concerns the study of three components, i) the heart which ensures blood circulation and plays the role of a pump assuring the irrigation of nearly 100,000 kilometers of vessels, ii) vessels, which serve as passageways or pipes to deserve all the body from the heart, and iii) blood which plays the role of medium of transportation.

The arteries play an essential role in maintaining blood pressure during the cardiac cycle thanks to their elasticity; this optimal blood pressure allows the irrigation of all points of the body, even the most distant capillaries. Endowed with their own musculature (smooth muscle cells), the arteries can vary the state of tension of their wall and thereby regulate blood pressure.

In this work, we focus on two diseases that affect the main artery in the cardiovascular system which is the aorta. Abdominal aortic aneurysm AAA and aortic coarctation CoA will be studied in our thesis. The following sections will be dedicated to the presentation of these two diseases (.ie. AAA and CoA).

2.3. AORTA ANATOMY AND DISEASES

2.3.1. Anatomy of the aorta

The aorta is the largest artery of the cardiovascular system. It starts directly from the heart (left ventricle) and supplies all the organs of the body through systemic circulation (except the lungs) and extends to the abdomen then it divides into the two iliac arteries (See Figure 2.4).

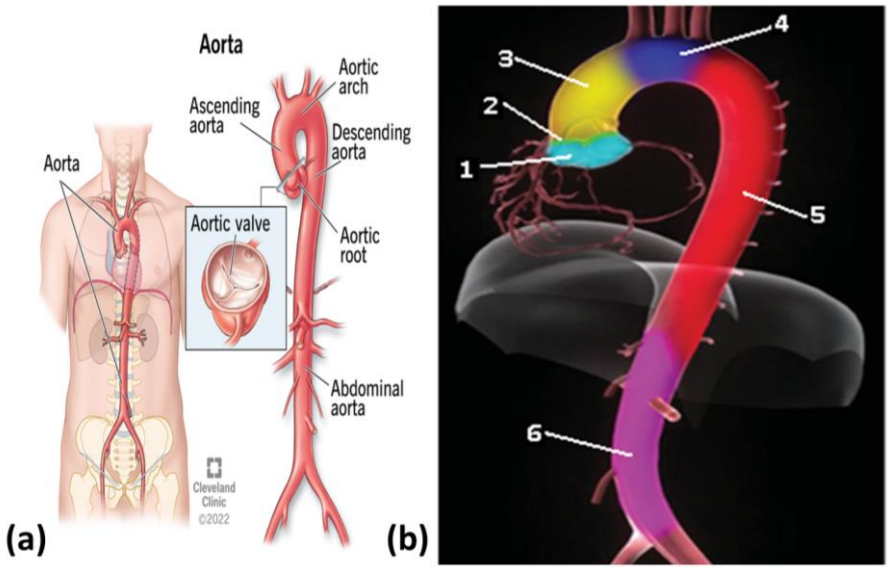

Figure. 2.4. Schematic representation of the aorta in the human body (a) [75] a Segmental division of the aorta (b) (adapted from [76]).

As shown in figure 2.4(b), the anatomy of the aorta can be divided as follows: (1) the aortic root; (2) the sinotubular junction; (3) the ascending aorta; (4) the aortic arch; (5) the descending (thoracic) aorta, and finally (6) the abdominal aorta AA [76].

2.3.2. Abdominal Aortic Aneurysm AAA

The abdominal aorta AA is the diaphragmatic aorta down to the aortic bifurcation (see Figure 2.4 (b) pink color and number 6), it includes the inferior phrenic arteries, branches of the celiac artery (hepatic artery, gastroepiploic artery, and splenic artery), renal arteries, superior mesenteric artery, inferior mesenteric artery, lumbar arteries and spinal artery, and the iliac arteries.

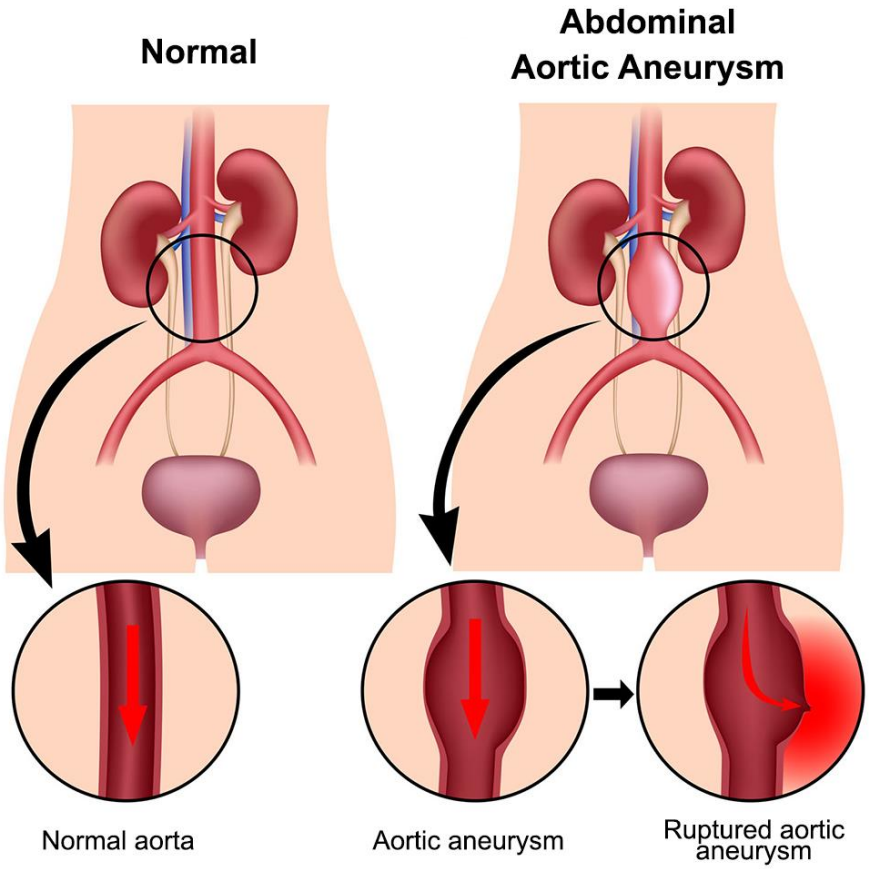

Figure. 2.5. Schematic representation of the normal abdominal aorta, abdominal aortic aneurysm AAA, and ruptured AAA. The image is adapted from [77].

The normal diameter of the abdominal aorta is equal to 2.0 cm (mean ± 2 SD) and the normal diameter of the infrarenal abdominal aorta is <2.0 cm (mean ± 2 SD) (see

the leftmost side of Figure 2.5 and the red arrows in Figure 2.6). There is a rule called the "thumb rule" that allows you to know the approximate diameter of the abdominal aorta, which says that the size of the AA is approximate to the size of the patient's thumb.

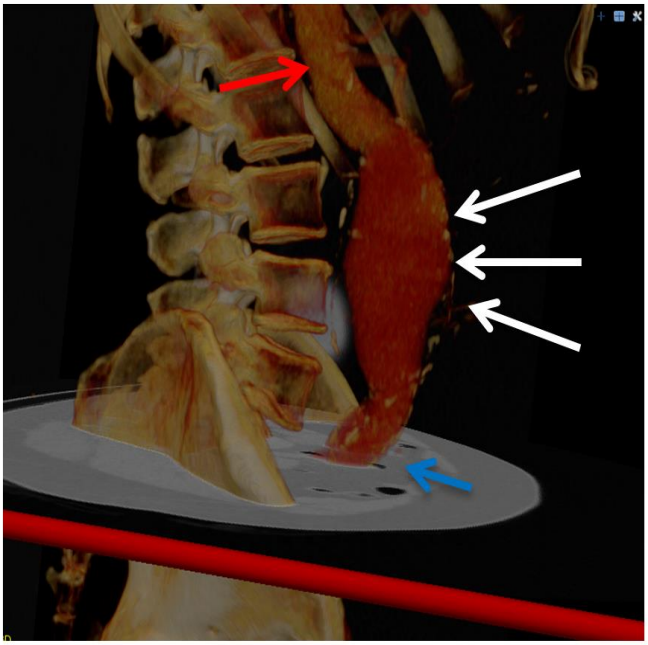

Figure. 2.6. Abdominal aortic aneurysm reconstruction image of an abdominal aortic aneurysm (white arrows), the healthy part of the aorta is indicated by red arrow and iliac arteries by blue arrow (CT sacn provided by radiologist during the thesis).

There is no universally accepted definition of AAA. However, most commonly it refers to deformation and a localized dilatation of the abdominal aortic wall (usually infrarenal) with an increase in diameter of 50% [78,79] or more of the diameter of a healthy aorta (typical value used to define an AAA is ≥ 3 cm - see the right side of Figure 2.5). AAA is one of the most common cardiovascular diseases, with a prevalence of 1.7-5 % for people over 65 years of age [80], reaching up to 10% for 80 years old male subjects [81]. AAA can undergo sudden rupture, frequently fatal, making AAA rupture one of the most common causes of death in the world. Most patients are unaware that they have an AAA and are diagnosed accidentally (incidental finding). Most AAAs are asymptomatic and remain asymptomatic until

rupture. Pain resulting from the expansion of the AAA indicates a threat of rupture. Pain attributable to AAA is usually new, constant, and located in the mid-abdomen, pelvis, or lumbar (lower back) region.

Rupture usually presents with abdominal or flank pain, hypotension, or abdominal distension (abdominal bloating). Other telltale or indicative signs may be a shock, cardiac arrest, aortic thrombosis, lower extremity thromboembolism, embolization of mural thrombus (clot), thrombosis in situ, and infection (endovascular infection) which leads to rupture.

According to Kavanagh et al 75% of clinically-relevant abdominal aortic aneurysms (AAAs) present with intraluminal thrombus (ILT) [82]. Da Silva et al. [83], report that ruptures occurred in the region of intraluminal thrombus (ILT) in 80% of AAA. However the role of ILT in AAA is still controversial between protective role from rupture or factor contributing to the degradation and consequently the rupture of the wall. Despite its role, ILT formation is related to the abnormal and non-physiologic hemodynamic conditions to which the endothelial cells ECs are subjected to. An example of ILT in AAA patient is shown in Figure 2.7.

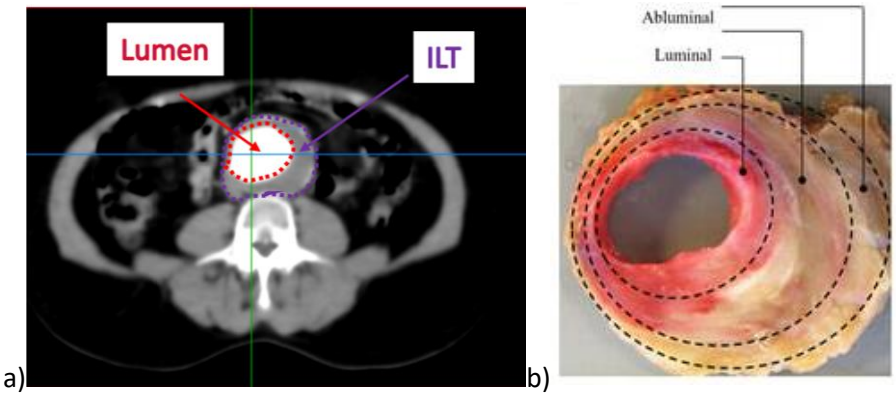

Figure. 2.7. Example of CT scan slices in axial views (derived from one of the group of patients studied in Chapter 6) ; lumen and ILT regions are shown and Cross-section of the bulk ILT tissue [84].

2.3.3. Aortic coarctation CoA

Coarctation of the aorta (CoA) is one of the most severe congenital heart diseases (CHD); it involves stenosis (in which a part of the aorta is narrower than usual of the

thoracic descending aorta (see Figure 2.8), in the vicinity of the ductus arteriosus, after the subclavian artery takeoff. The two main types of coarctation are pre- and post-ductal as presented in Figure 2.9 [85]. This malformation if not treated early, can lead to a decrease in life expectancy due to complications such as coronary artery disease, hypertension, stroke, rupture of the vessel, and aneurysm formation [86]. Typically, CoA is diagnosed in childhood and accounts for around 5%-8% of all congenital heart defects [87].

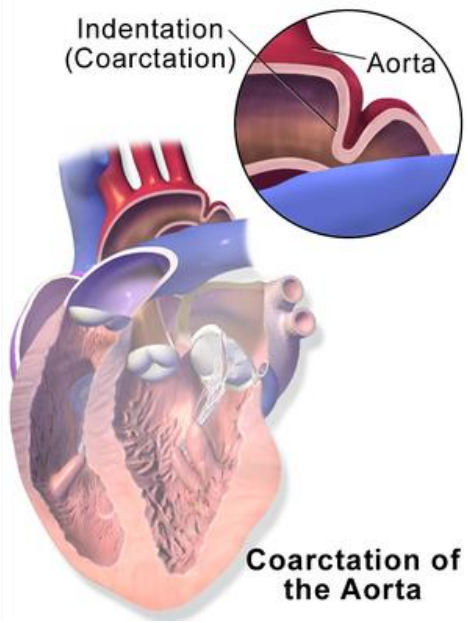

Figure. 2.8. Illustration depicting coarctation of the aorta with heart [88]

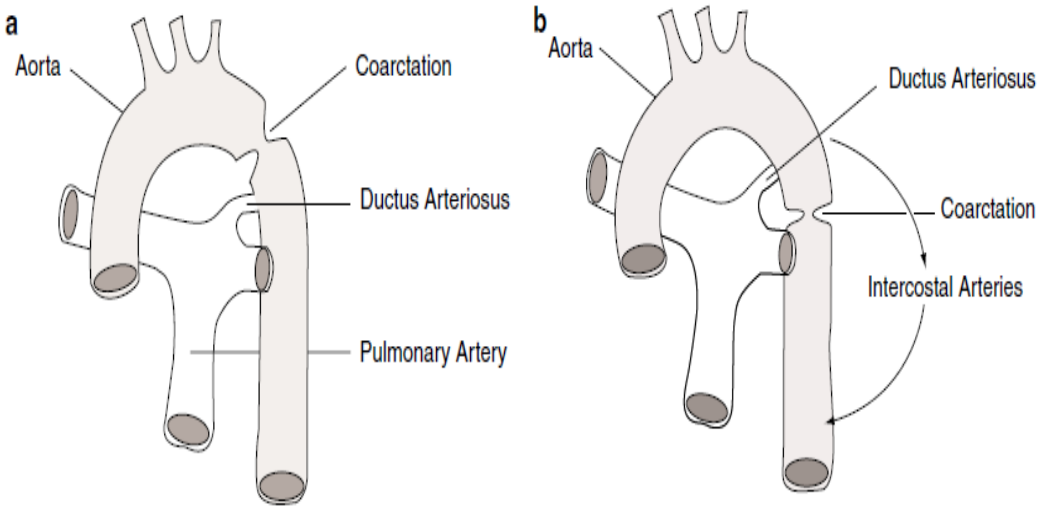

Figure. 2.9. Aortic coarctation: (a) preductal coarctation; (b) postductal coarctation, the most frequent type in adults [85].

2.3.3.1. Diagnosis

For CoA in the infantile type (pre-ductal type), most cases are symptomatic due to heart failure caused and depend on age, association with other and more complex cardiac malformations. For young adults, adolescents, and older children the coarctation is asymptomatic and is diagnosed accidentally by imaging the chest (radiography or echocardiography).

For the diagnosis of CoA, transthoracic echocardiography TTE is the most used imaging technique in clinical routine, especially for infantile and young child patients thanks to their small bodies allowing access to the coarctation region and providing information about the site, structure, and hemodynamic data. However, in older and/or obese patients the visualization by TTE becomes difficult. In that case, computed tomography imaging (CT scans) could be useful to extract and visualize the 3D anatomy of the CoA.

Thanks to new technological developments in data analysis, image acquisition, and reconstruction, Magnetic resonance imaging (MRI) makes an interesting non-invasive contribution to the study of the coarctation of the aorta. Contrary to the CT imaging technique, the MRI technique provides hemodynamic information and is not ionizing. Thanks to cine-MRI, dynamic images could be provided. Furthermore, 3D time-resolved phase contrast MRI, with three-directional velocity encoding (4D Flow MRI), allows both visualization and quantification of *in-vivo* blood flow with full volumetric coverage of the aorta [89]. Nevertheless, because of its cost and its technological constraints, MRI and MRI-based techniques are still not abundant in low-income countries and in limited resources hospitals.

Up to now, 4D Flow MRI is the unique way to measure and visualize full 3D time-dependent *in-vivo* blood flow [90], though with the drawback of low spatial and temporal resolution [62,91] and requiring a longer scanning time [92] (up to 20 minutes in cases of a large volume of interest, such as the aorta or whole heart). Furthermore, computational fluid dynamics (CFD) provides insights into the 3D blood flow and wall parameters with high spatial and temporal resolution compared

to 4D Flow MRI. Moreover, CFD allows the use of virtual surgery planning by modifying the vessel in the planned or desired postoperative geometry [93]. However, their consistency (.ie. CFD) with *in-vivo* data may be hampered by the used boundary conditions and the precision of complex patient-specific geometries. An example of segmented 3D geometry extracted from volumetric magnetic resonance angiography MRA images of a Patient presenting aortic coarctation is shown in Figure 2.10.

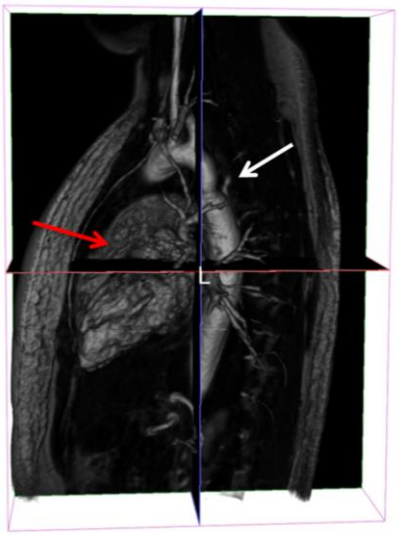

Figure. 2.10. Example of segmented 3D geometry superimposed on a volumetric magnetic resonance angiography MRA images of a Patient presenting aortic coarctation (the white arrow shows the coarctation and, the red arrow shows the heart).

Chapter 3

Mathematical Model

3.1. INTRODUCTION

Hemodynamics (or “blood flow dynamics”) is the study of blood flow properties. This chapter contains some of the basics of fluid mechanics applicable to blood flow in vessels, particularly in the case of two diseases .ie. Abdominal aortic aneurysm AAA and aortic coarctation CoA. The first part is devoted to the composition of blood, its rheology and its behaviour in arteries. Then the second part is dedicated to governing equations. Finally, in the last part of this Chapter, the wall parameters used in the post-processing of the data are described.

3.2. BLOOD: COMPOSITION, RHEOLOGY AND BEHAVIOR IN ARTERIES

3.2.1. Composition

Blood is a suspension of cells in plasma [94]. By volume, blood is composed of 45% cellular elements and 55% of plasma (see Figure 3.1). Under normal conditions, erythrocytes (red blood cells RBC) represent 99% of the volume of the cells, the rest (1%) being leukocytes (white blood cells) and platelets (also called thrombocytes, which are fragments of cells that are responsible of the coagulation) [95]; on the other hand, plasma, which is a yellowish viscous liquid, is composed of 90% water, 7% plasma proteins, 1% inorganic substances and 1% organic substances. It also contains gases, products, and wastes of cellular activity and ions.

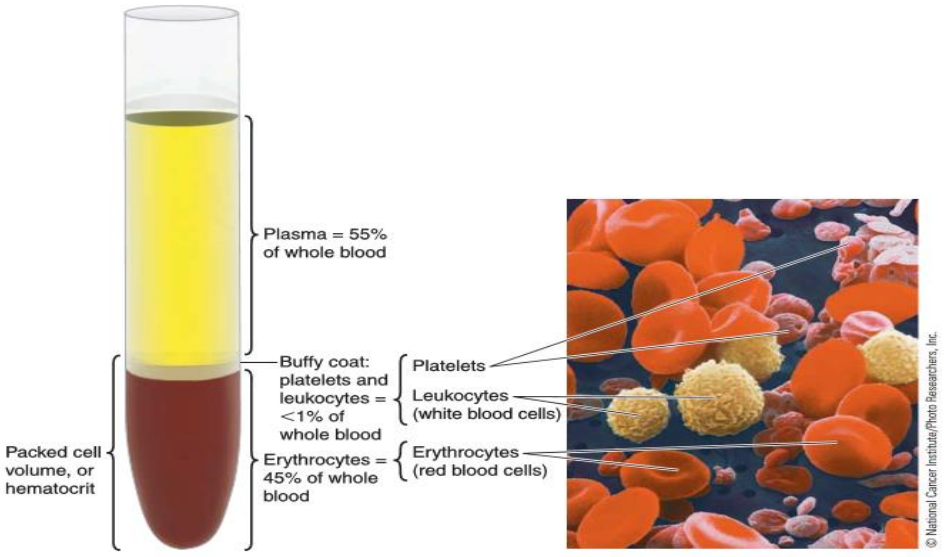

Figure 3.1: Blood composition [95].

3.2.2. Rheology of blood

Blood is a complex fluid made of a suspension of cells in plasma [94]. It was (.ie. blood) defined by David A. Steinman [96] as fluid-filled vesicles in water-like Carrier (plasma) (see Figure 3.2). This carrier (.ie. plasma) is mostly water with some dissolved proteins and is widely considered to behave as a Newtonian fluid (constant viscosity). The viscosity of blood, therefore, depends on the viscosity of the plasma, in combination with fluid-filled vesicles (erythrocytes or RBC) and consequently the hematocrit (% by volume of RBC, Ht). RBC looks typically like a biconcave disk with a diameter of 7.5-8 μm and 2-2.5 μm height [96,97], depending on flow conditions the RBC could take a different shape. The deformability of RBC gives blood its non-Newtonian shear-thinning property. Higher hematocrit Ht and less deformable cells imply higher viscosity. The relationship between hematocrit and viscosity is complex and many formulas exist, the simplest equation was introduced by Einstein (see equation 3.1 and figure 3.3). Various investigations and models were carried out showing the blood viscosity μ as a function of shear rate originating from the deformability of RBC (see figure 3.4 and table 3.1).

$$\mu = \mu_{plasma}.(1 + 2.5\ \mathrm{Ht}) \tag{3.1}$$

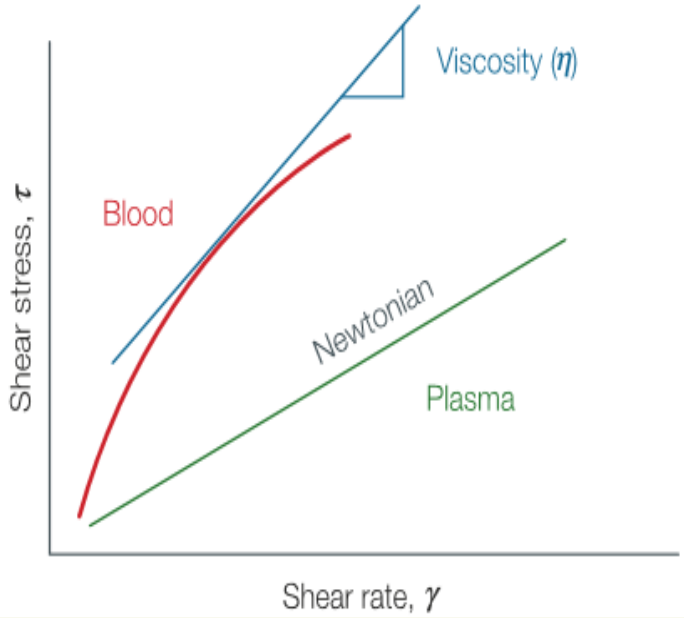

Figure. 3.2: Shear-dependent viscosity of blood and plasma [97].

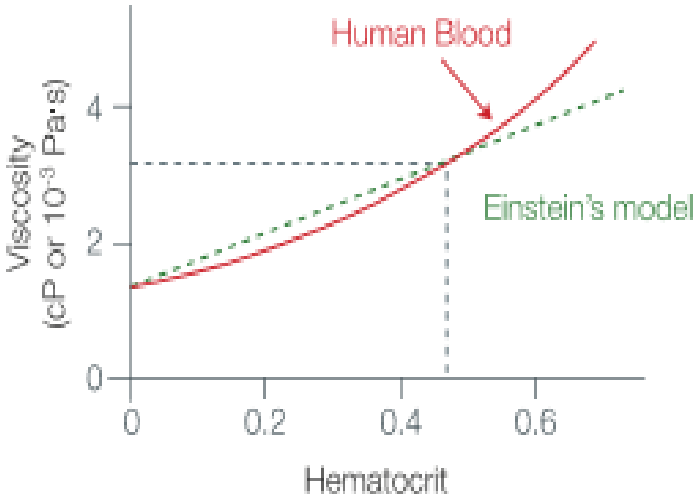

Figure. 3.3: Viscosity as a function of hematocrit [97].

Table. 3.1: Constitutive equations used for the non-Newtonian viscosity μ of blood as a function of shear rate $\dot{\gamma}$ [98]:

Non-Newtonian Model	**Constitutive Equations**	**Characteristics and Models constants (blood viscosity is given in poise 1poise=0.1 Pa s)**
Powell-Eyring Model	$\mu = \mu_\infty + (\mu_o - \mu_\infty) * \left[\frac{sinh^{-1}\lambda\dot{\gamma}}{\lambda\dot{\gamma}}\right]$	$\lambda = 5.383s$ $\mu_o = 0.56\ poise$ $\mu_\infty = 0.0345\ poise$
Modified Powell-Eyring Model	$\mu = \mu_\infty + (\mu_o - \mu_\infty) * \left[\frac{\ln(\lambda\dot{\gamma} + 1)}{[\lambda\dot{\gamma}^m]}\right]$	$\lambda = 2.415s$ $\mu_o = 0.56\ poise$ $\mu_\infty = 0.0345\ poise$ $m = 1.089$
Cross Model	$\mu = \mu_\infty + (\mu_o - \mu_\infty) * \frac{1}{1 + (\lambda\dot{\gamma})^m}$	$\lambda = 1.007s$ $\mu_o = 0.56\ poise$ $\mu_\infty = 0.0345\ poise$ $m = 1.028$
Simplified Cross Model	$\mu = \mu_\infty + (\mu_o - \mu_\infty) * \frac{1}{1 + \lambda\dot{\gamma}}$	$\lambda = 8.0s,$ $\mu_o = 1.30\ poise$ $\mu_\infty = 0.05\ poise$
Modified Cross Model	$\mu = \mu_\infty + (\mu_o - \mu_\infty) * \frac{1}{[1 + (\lambda\dot{\gamma})^m]^a}$	$\lambda = 3.736s,$ $\mu_o = 0.56\ poise$ $\mu_\infty = 0.0345\ poise$ $m = 2.406$ $a = 0.254$
Carreau Model	$\mu = \mu_\infty + (\mu_o - \mu_\infty) * (1 + (\lambda\dot{\gamma})^2)^{\frac{n-1}{2}}$	$\lambda = 3.736s$ $\mu_o = 0.56\ poise$ $\mu_\infty = 0.0345\ poise$ $m = 2.406$ $a = 0.254$

Carreau-Yasuda Model	$\mu = \mu_\infty + (\mu_o - \mu_\infty) * (1 + (\lambda\,\dot{\gamma})^a)^{\frac{n-1}{a}}$	$\lambda = 3.736s$ $n = 0.22$ $a = 1.25$
Casson Model	$\sqrt{\tau} = \sqrt{k_0} + \sqrt{k_1\,\dot{\gamma}}$	$k_0 = 0.05\,\frac{dyne}{cm^2}$ $k_1 = 0.04\ dyne/cm^2$
Power-Law Model	$\tau = m(\dot{\gamma})^n$	Liepsch and Moravec : $n = 0.61, m = 0.42$ Davies et al : $n = 0.61, m = 0.42$ if $\dot{\gamma} \leq 226.5\ s^{-1}$ $\mu = 0.04$, if $\dot{\gamma} > 226.5\ s^{-1}$

3.2.3. Blood Behavior in micro-circulation (small arteries) and macro-circulation (large arteries)

As described in the earlier section the viscosity of blood depends on the shear rate. More exactly formulated, for high shear rates, the viscosity decreases (Figure 3.4 and Figure 3.5-a) [5,6]. At high shear rates, the disks of RBC formed orient in the flow direction, and the viscosity decreases. At extremely low shear rates the formation of RBC aggregates may occur, which increases the viscosity to a very high value.

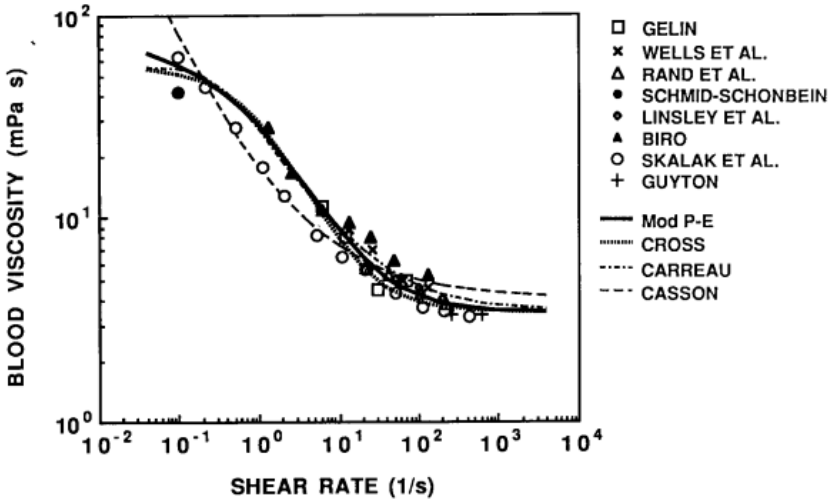

Figure. 3.4: Blood viscosity as a function of shear rate from experimental and different models. The percentage of Ht is in the range of 33-45%. Symbols relate to data measured experimentally and solid and dashed lines represent predictions using the models [98].

As shown in Figures 3.5a and 3.5b for shear rates below 100 s^{-1}, blood viscosity decrease exponentially, at shear rates above about 100 s^{-1} blood viscosity become

constant similarly to Newtonian fluid. Since in large arteries (for example aorta) shear rates are expected to be on the order of 100 s^{-1} the Newtonian approximation is widely justified [96].

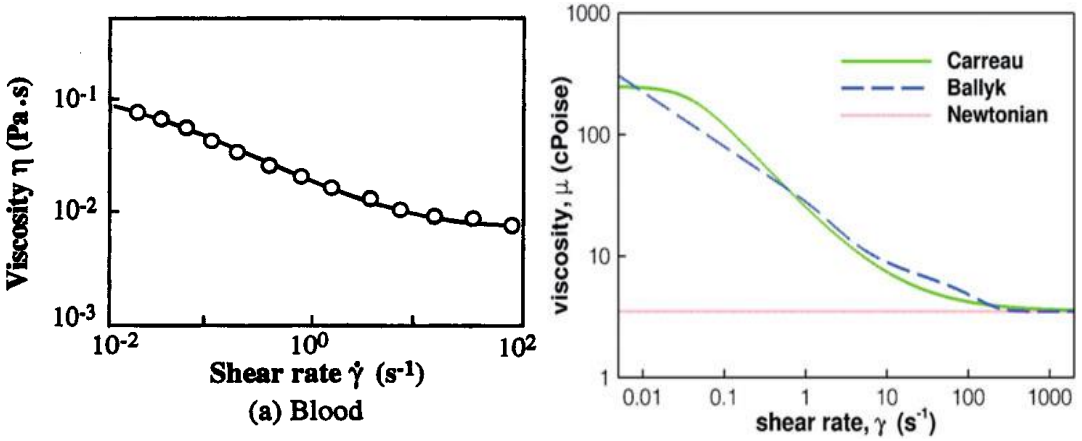

a) b)

Figure. 3.5: a) Blood viscosity as a function of shear rate [99]. b) shear rate Shear-thinning behaviour of blood, approximated by the Carreau and generalized power law (Ballyk) curve fits. [96].

Viscosity also depends on the size of the blood vessel (Figure 3.6). In small blood vessels and at low velocities, blood viscosity decreases with decreasing vessel size (Figures 3.7a & 3.7b). This is known as the Fahraeus-Lindqvist effect, and it begins to play a role in vessels smaller than 1 mm in diameter (see figure 3.8). Therefore, the non-Newtonian character of the blood only plays a role in the microcirculation where RBC deforms significantly (see figure 3.7-b) [100].

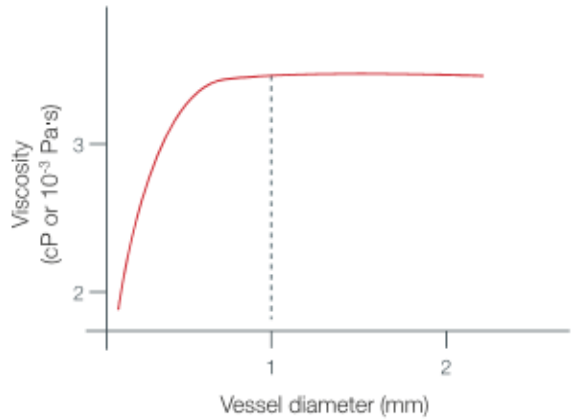

Figure. 3.6: Blood viscosity as a function of vessel size [97].

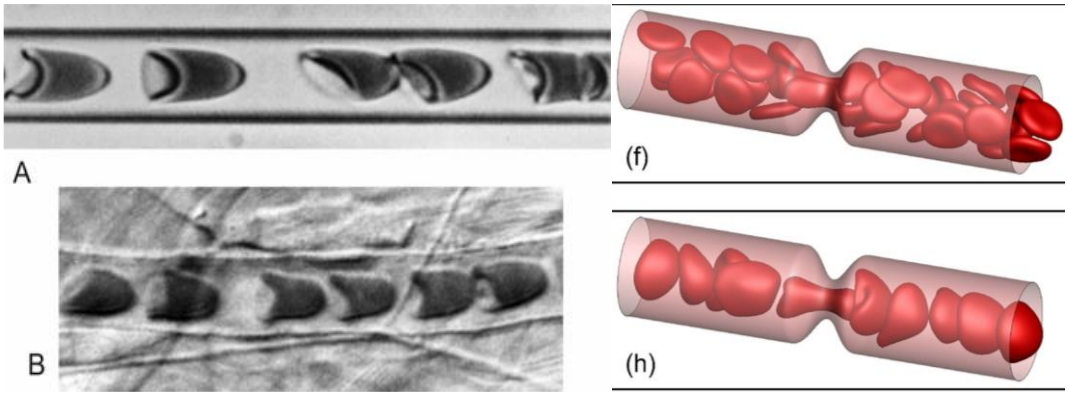

a) b)

Figure. 3.7: a) Human RBCs flowing in a glass tube with a diameter of 7 µm (bottom left-most side figure). Blood flow through a capillary in the rat mesentery with a diameter of approximately 7 µm (bottom left-most side figure). Flow is from left to right in each case. b) Snapshots showing instantaneous RBC distribution from a few representative simulations for 84% stenosed (right-most side figures) vessels at Ht ≈ 22–24% (Adapted from [100]).

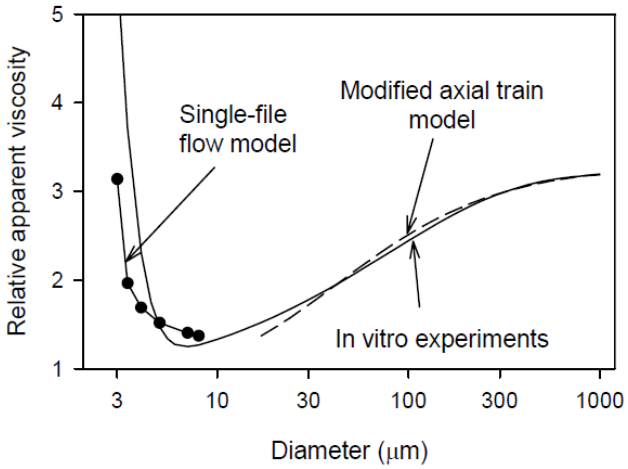

Figure. 3.8: Fahraeus-Liindqvist effet, experimental data and theoretical predictions [101].

3.2.4. Blood behavior in aortic coarctation (CoA) and abdominal aortic aneurysm (AAA)

To summarize the blood behaviour of microvascular stenosis is very different from that of macrovascular stenosis. In macrovascular stenosis blood behaves as a Newtonian fluid in large arteries however in microvessels it behaves as a non-Newtonian fluid [102]. In our study related to aortic stenosis (Coarctation) treated in Chapter 7, the Newtonian hypothesis is maintained and more details are provided in this Chapter and in our prior works [103, 62].

Similarly to CoA, in AAA the non-Newtonian behaviour of blood is limited [104], and it begins to play a role in vessels smaller than 1 mm in diameter [97,105]. Pedley & Fung [105] show that in vessels greater than approximately 0.5 mm in diameter it is reasonable to model blood as a Newtonian fluid. This assumption was also adopted in Chapter 5 related to AAA, however in Chapter 6 to capture blood's shear-thinning behaviour the Carreau-Yasuda (C-Y) model was used [69, 106]. More details are provided in the chapters cited above.

3.3. GOVERNING EQUATIONS

Fluid dynamic is a sub-discipline of fluid mechanics which studies the movement of fluid (gas or liquid); it is based on continuity assumption where the fluid is assumed to be continuous instead of discrete. The governing equations are based on the conservative's laws: .ie. Conservation of mass, Conservation of momentum, Conservation of energy, Conservation of species, and Effects of body forces (in our case the Conservation of mass and Conservation of momentum are used).

3.3.1. Mathematical description of fluid flow (governing equations)

3.3.1.1. Conservation of mass equation (continuity)

Considering an infinitesimal material volume of fluid $V_m(t)$. The mass m contained in this volume is:

$$m = \int_{V_m(t)} \rho \; dV \tag{3.2}$$

where ρ is the local density. If the material volume contains neither sources nor sinks, the mass which is in $V_m(t)$ is constant and we can write it as follow:

$$\frac{d}{dt} m = \frac{d}{dt} \int_{V_m(t)} \rho \; dV = 0 \tag{3.3}$$

We apply the transport theorem to this equation:

$$\frac{d}{dt} \int_{V_m(t)} \rho \; dV = \int_{V_m(t)} \frac{\partial \rho}{\partial t} dV \; + \int_{A_m(t)}^{0} \rho v . n \; dA \tag{3.4}$$

And the Green-Ostrogradsky theorem (supposing the volume $V_m(t)$ does not contain a discontinuity):

$$\int_{A_m(t)} \rho v.n\, dA = \int_{Vm(t)} \nabla.\rho v\, dV \tag{3.5}$$

We obtain :

$$\int_{Vm(t)} \left[\frac{\partial \rho}{\partial t} + \nabla.\rho v\right] dV = 0 \tag{3.6}$$

The volume of integration is arbitrary and consequently the integrand must be identically zero:

$$\frac{\partial \rho}{\partial t} + \nabla.\rho v = 0 \tag{3.7}$$

This local equation expresses the conservation of mass. It is applicable at any point of a continuous fluid containing no sources or sinks.

Equation (3.7) is often referred to as the continuity equation. It can be written in a slightly different form by expanding $\nabla.\rho v$

According to a classic vector identity: $\nabla.\rho v = \rho\nabla.v + v.\nabla\rho$

By substituting this relation in (3.7), we obtain:

$$\frac{\partial \rho}{\partial t} + \rho\nabla.v + v.\nabla\rho = 0 \tag{3.8}$$

and we can write (3.7) in the form (when ρ is considered as constant:

$$\frac{\partial \rho}{\partial t} + \rho\nabla.v = 0 \tag{3.9}$$

3.3.1.2. Conservation of momentum equation

Considering again a material control volume $V_m(t)$. The momentum contained in this volume is:

$$\int_{V_m(t)} \rho v\, dV \tag{3.10}$$

The fundamental principle of dynamics states that the change in momentum of this material system is equal to the sum of all external forces applied to it. Considering again a material control volume $V_m(t)$. The momentum contained in this volume is:

$$\frac{d}{dt}\int_{V_m(t)} \rho v\, dV = F \tag{3.11}$$

In most (classical) situations, two types of forces act on the fluid contained in V_m:

1- the volume forces that can be expressed in the form: $\int_{V_m(t)} \rho g \, dV$

2- the surface forces which act through the surface area $A_m(t)$: $\int_{A_m(t)} t(n) \, dA$

n: denotes the exterior normal.

t (n): is the constraint vector acting on dA.

The expression (3.11) can therefore be written in the form (after projection on the axis of fixed Cartesian systems):

$$\frac{d}{dt}\int_{V_m(t)} \rho \, v \, dV = \int_{V_m(t)} \rho \, g \, dV + \int_{Am(t)} ti(n) \, dA \qquad (3.12)$$

Here we use Einstien's notation: $t_i(n) = T_{ij} \, n_j$

From a physical point of view, it is interesting to decompose the constraint t into two parts:

• Stress associated to the pressure

• Stress associated to viscous forces

The pressure acts isotropically and its value depends only on the thermodynamic state of the fluid. The Viscous stresses are, on the contrary, essentially linked to the state of deformation of the fluid. We can write under these conditions:

$T_{ij} = -p \, \delta_{ij} + \tau_{ij}$

T_{ij} *: Stress Tensor*

$-p \, \delta_{ij}$: Tensor of stresses associated to the pressure

τ_{ij} : Tensor of viscous stresse

Based on these equations and after the expansion of the second term of equation (3.12) we find:

$$\int_{V_m(t)} \rho \, \frac{dv}{dt} \, dV = \int_{V_m(t)} \left[\rho \, g - \frac{\partial p}{\partial x} + \frac{\partial \tau_{ij}}{\partial x}\right] dV \qquad (3.13)$$

The control volume $V_m(t)$ is arbitrary and the integrands appearing in both members must be identical:

$$\rho \frac{dv}{dt} = -\frac{\partial p}{\partial x} + \rho \, g + \frac{\partial \tau_{ij}}{\partial x} \qquad (3.14)$$

The physical meaning of this equation becomes clear:

The quantity of Acceleration Constraints per volume unit =

Forces associated to the exerted pressure per volume unit +

Volume forces per volume unit + Viscous forces per volume unit

3.3.1.3. Continuity and momentum conservation equation in specific forms (Newtonian & Non-Newtonian fluid)

In our study in chapter 5 and chapter 7, the blood is considered as an incompressible and Newtonian fluid, with a homogeneous dynamic viscosity [62, 107]. The flow in the abdominal aorta is hence described by the general incompressible Navier-Stokes and continuity equations:

$$\rho \frac{dv}{dt} = -\nabla p + \mu \, \Delta v \tag{3.15}$$

$$\nabla . \, v = 0 \tag{3.16}$$

Where ρ is the density of the blood, p is the pressure of the blood and μ is dynamic viscosity of the blood.

However in chapter 6, the shear thinning behavior is taken into account by using the careau yasuda C-Y model. As it was shown in equation 3.14, τ_{ij} represent the tensor of viscous stresse, The stress tensor for an incompressible Newtonian fluid is defined as:

$$\tau_{ij=} 2 \, \mu \, d_{ij} \tag{3.17}$$

where μ is the Newtonian viscosity of the fluid and d_{ij} is the rate of deformation tensor. The d_{ij} is defined as:

$$d_{ij} = \frac{1}{2}(u_{i,j} - u_{j,i}) \tag{3.18}$$

In non-Newtonian fluids, the notation $\dot{\gamma}$ is used to represent the shear rate:

$$\dot{\gamma} = \sqrt{2 \, d_{ij} \, d_{ji}} \tag{3.19}$$

For incompressible Newtonian fluids, the relationship between stress tensor and the shear rate is linear. Any fluid that does not exhibit the same behavior as the Newtonian constitutive relationship of Eq. (3.17) is classified as non-Newtonian.

Viscosity can be described as measurement of the resistance of a fluid to deform or to flow under shear stress [108]. In the simplest type of non- Newtonian model and assuming that blood behaves as a generalized Newtonian fluid [109],used in this study (often called as generalized Newtonian or purely viscous), the stress is a function of the shear rate only and the relation in Eq. (3.17) can be generalized as

$$\tau_{ij=}2\,\mu(\dot{\gamma})d_{ij} \tag{3.20}$$

$\mu(\dot{\gamma})$ is the viscosity a function of the magnitude of strain rate. Blood viscosity decrease (shear thinning) when it is driven to flow at high shear rates. It was shown the shear thinning behavior could be captured using the Carreau- Yasuda model defined as:

$$\mu(\dot{\gamma}) = \mu_\infty + (\mu_o - \mu_\infty) * (1 + (\lambda\,\dot{\gamma})^a)^{\frac{n-1}{a}} \tag{3.21}$$

where η, $\dot{\gamma}$, μ_∞ and μ_o are the viscosity, shear rate, viscosity at infinite shear-rate and the zero-shear viscosity, respectively. λ, α, and n are material coefficients (λ = 1.902 s, a = 1.25, n = 0.22). For blood, μ_∞ = 0.00345 Pa s, μ_0 = 0.056 Pa s [110,98].

3.4. WALL PARAMETERS EQUATIONS

Many hemodynamic wall parameters including Time-Averaged Wall Shear Stress (TAWSS), Oscillatory Shear Index (OSI) [112], TransWSS [113], Relative Residence Time (RRT) [114], and Endothelial Cell Activation Potential (ECAP) are documented in chapters 5 and 6. An in-house MATLAB script is used for the post-processing and the calculation of those parameters.

In detail, WSS is the friction which creates a tangential force exerted by the blood flow on the vessel wall (see Figure 3.9). It is defined as:

$$WSS = \mu\left(\frac{\partial v}{\partial y}\right)_{y=0} \tag{3.22}$$

Where y is the distance to the wall, v the velocity of the fluid and μ the dynamic viscosity.

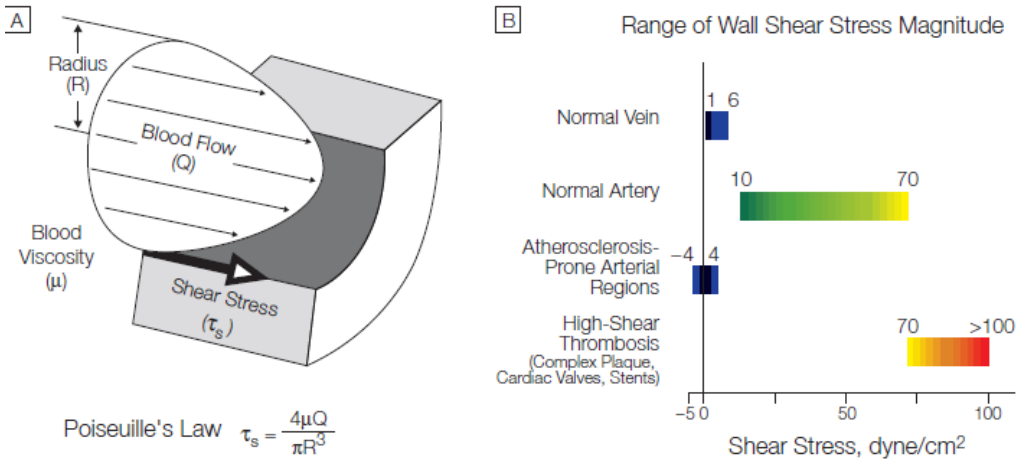

Figure 3.9: Wall shear stress (WSS) force excreted to the arterial wall. WSS is represented as the tangential force exerted by the blood flow on the vessel wall [64].

In addition to the endothelial layers' thrombogenic function, they are (.ie. endothelial layers) also the mechano-detecting elements which detect the local blood flow conditions and induce autocrine stimulation. In-vivo and in-vitro studies demonstrate the destructive effect of low and oscillatory WSS on the endothelial function [97] and their effect on intimal thickening. Under physiologic shear stress, the endothelial cells are aligned to the flow direction, which differs from the low shear stress case (see Figure 3.10)[97, 64]. Regions of low WSS are also associated with rupture and expansion sites of the AAAs [65]. The high level of WSS leads to athero-protective endothelial phenotype and decreases the expression of the vasoconstrictor [97].

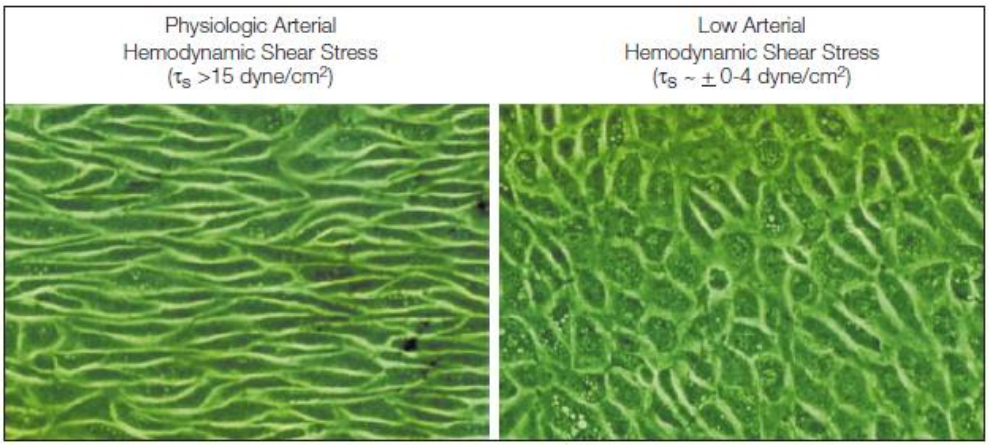

Figure 3.10: Relationship between WSS range and the alignement of endotghelial cells. An example of bovine Bovine aortic endothelial cells exposed for 24 hours to: 1- physiologic shear stress (align in the direction of blood flow left Figure) and 2- to low shear stress (right Figure) [64] (1 dyne/cm2 = 0.1 Pa).

The OSI is a mechanical factor related to flow oscillation throughout the cardiac cycle of period *T*. It represents the temporal variation in WSS direction which has been shown to affect the endothelial cells (EC) behavior. This dimensionless scalar index range between 0 and 0.5 and is defined by:

$$OSI = \frac{1}{2}\left(1 - \frac{AWSSV}{TAWSS}\right) \tag{3.23}$$

$\mathrm{AWSSV} = \frac{1}{T}\left|\int_0^{\mathrm{T}} \overrightarrow{\mathrm{wss}}\,\mathrm{dt}\right|$ is the magnitude of the time-Averaged WSS vector.

$\mathrm{TAWSS} = \frac{1}{T}\int_0^{\mathrm{T}} |\overrightarrow{wss}|\mathrm{dt}$ is the time-Averaged WSS magnitude.

WSS is known to regulate the endothelial phenotype where low TAWSS values (<0.4 Pa) are atherogenic however physiological and elevated values are known to play the role of quiescent atheroprotective phenotype (> 1.5 Pa) [64].

The Relative Residence Time (RRT) is a mechanical factor which includes the effects of both OSI and the time-averaged WSS magnitude. This hemodynamic metrics is able to capture low and oscillatory WSS regions. It is defined as:

$$RRT = \frac{1}{(1 - 2.OSI).TAWSS} \tag{3.24}$$

The endothelial cell activation potential (ECAP) is a new parameter [14], which characterizes the degree of thrombogenic susceptibility of endothelial cell. This parameter localizes regions of high OSI and low TAWSS by using the ratio of OSI and the TAWSS .

$$ECAP = \frac{OSI}{TAWSS} \tag{3.25}$$

To distinguish between multidirectional and uniaxial flows, transversal WSS (TransWSS) is introduced by Peiffer et al [113]. TransWSS completes TAWSS and OSI instead of replacing them. Using this metrics combined with the values of TAWSS and OSI it will be possible to understand whether the flow is i-Unidirectional disturbed flow, ii-Oscillating non-disturbed flow, iii-Unidirectional disturbed flow or iv-Oscillating disturbed flow. Figure 3.11 show the importance of studying this

parameter to capture the nature of the flow near the wall to which the endothelial cells are subjected. It is defined as fellow:

$$TransWSS = \frac{1}{T}\left|\int_0^T \overrightarrow{wss}.\left(\vec{n} \wedge \frac{\int_0^T \overrightarrow{wss}\ dt}{\left|\int_0^T \overrightarrow{wss}\ \mathrm{dt}\right|}\right)\right| dt \qquad (3.26)$$

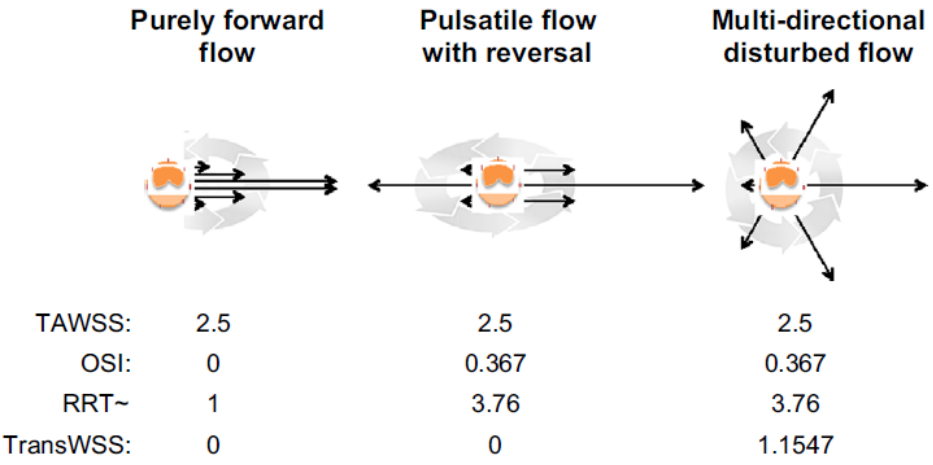

Figure 3.11: Graphical representations of flow near the wall to which Endothelial cells EC are subjected and relation with hemodynamic metrics [113].

Chapter 4

Methodology and Numerical Model

4.1. INTRODUCTION

Hemodynamics (or “blood flow dynamics”) is the study of blood flow properties. This chapter contains some of the basics of fluid mechanics applicable to blood flow in vessels, particularly in the case of two diseases .ie. Abdominal aortic aneurysm AAA and aortic coarctation CoA. The first part is devoted to show the methodology and the workflow adopted in our study in Chapter 5, 6 and 7. In the second part, a description of the used numerical model is summarized based on the code used in our studies.

4.2. METHODOLOGY AND WORKFLOW OF CFD STUDIES

To conduct CFD simulations a standard workflow needs to be followed, Ansys Fluent user guide defined nine steps in four parts as shown in the following flowchart (see Figure 4.1).

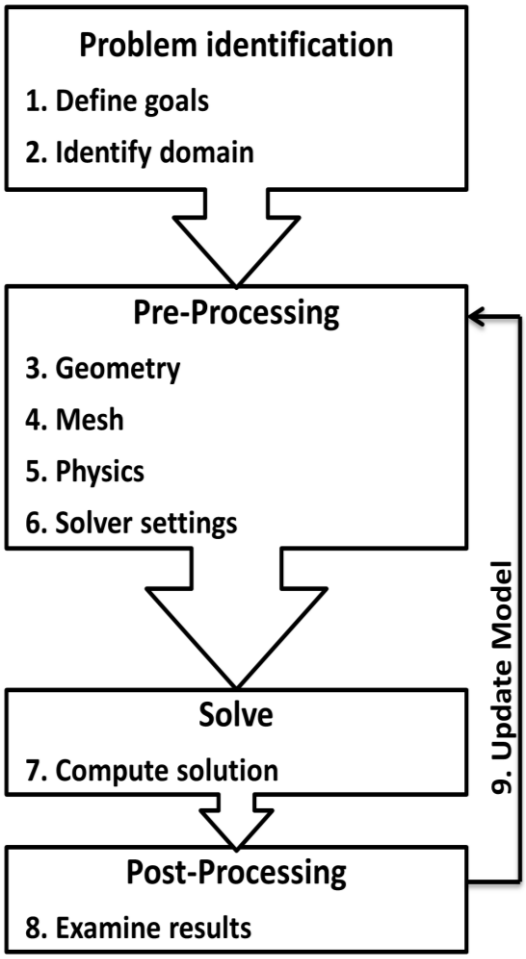

Figure. 4.1: Main CFD simulations flowchart [adapted from Ansys Fluent user guide].

In the first step we need to identify which results we are looking for (parameters of interest .ie. pressure, velocity, wall shear stress …etc). The region of interest ROI should be identified in the second step. From these steps, we should identify the appropriate physical model (equations to be resolved), which assumption could be acceptable for the study, which boundary conditions are needed and are available.

In the second part (preprocessing), the geometry is defined and created after the definition of the adequate fluid domain (in some cases simplification and smoothing of geometry are needed to remove uncertainty features and avoid possible complicated meshing). The adopted geometry needs to be divided into a number of elements (meshing) called control volumes (control volumes are the basis of the finite volume method FVM which will be detailed and explained in the following sections). In the fifth and sixth steps, we need to set up respectively the physics and the solver settings, where we define material properties, physical model, boundary conditions, and initial conditions.

In the third part (step seven), the discretized conservation equations are solved using iterative methods until reaching a pre-defined precision. This precision is verified based on the estimation of residuals (changes in solution variables between two consecutive iterations).

The last part (step eight) called Post Processing consists of the visualization and examination of the results using post-processing code or coding external scripts. This part allows the verification of the physical behaviour and the validation of the numerical results. Starting from this step we could decide whether we should adapt the model or not (step 9).

The following sections will be dedicated to the solving part, where the mathematical description of fluid dynamics and the methodology used to solve the equations computationally are going to be explained. The other parts (.ie. Problem identification, Pre-processing, and Post-processing) of the workflow shown in Figure 4.1 are detailed for each specific problem in the corresponding results in chapters 5, 6 and 7 and respectively below in Figures 4.2, 4.3 and 4.3 where the flowcharts are shown (for more details see the materials and method section in the corresponding chapters).

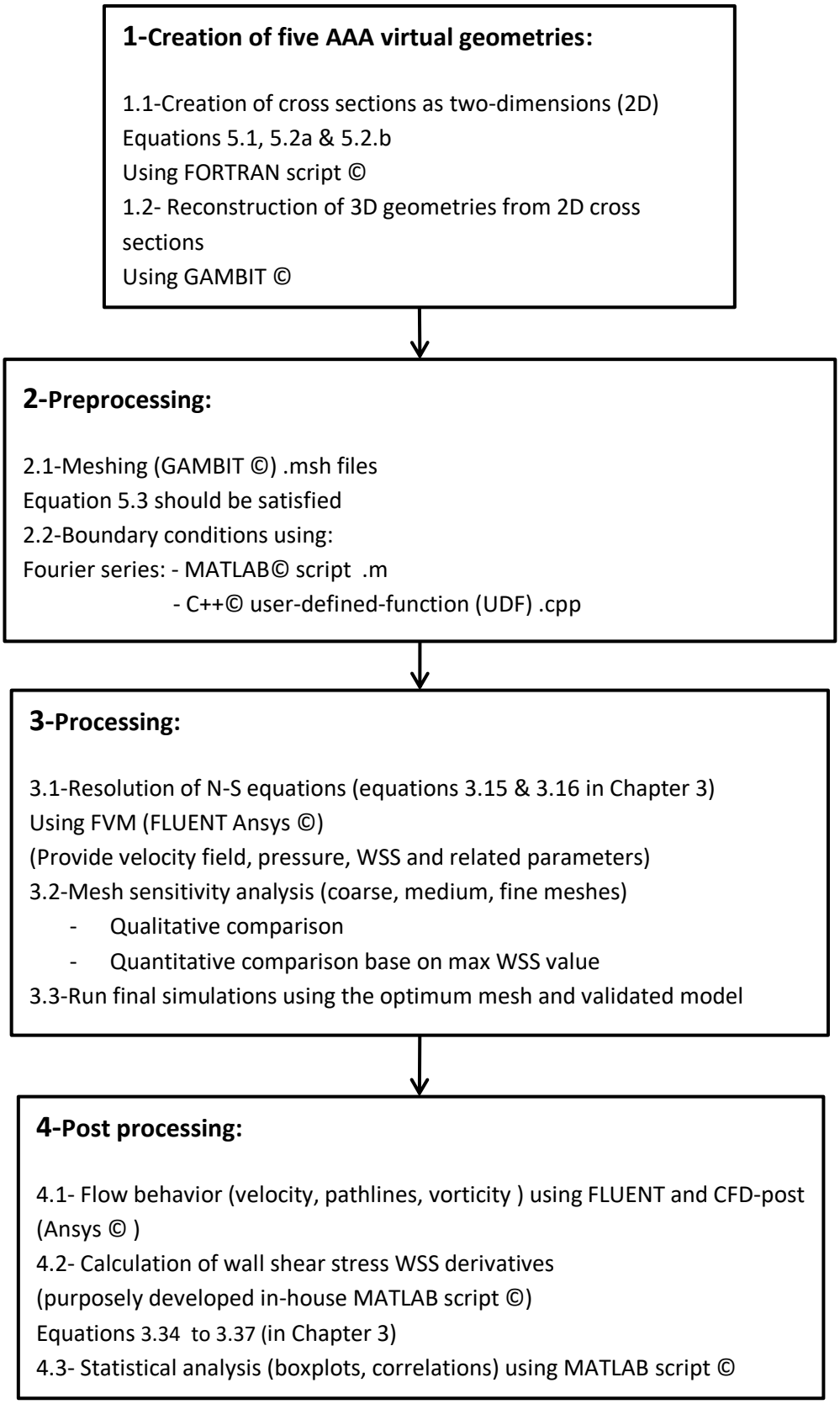

Figure. 4.2: Flowchart of the methodology used in Chapter 5.

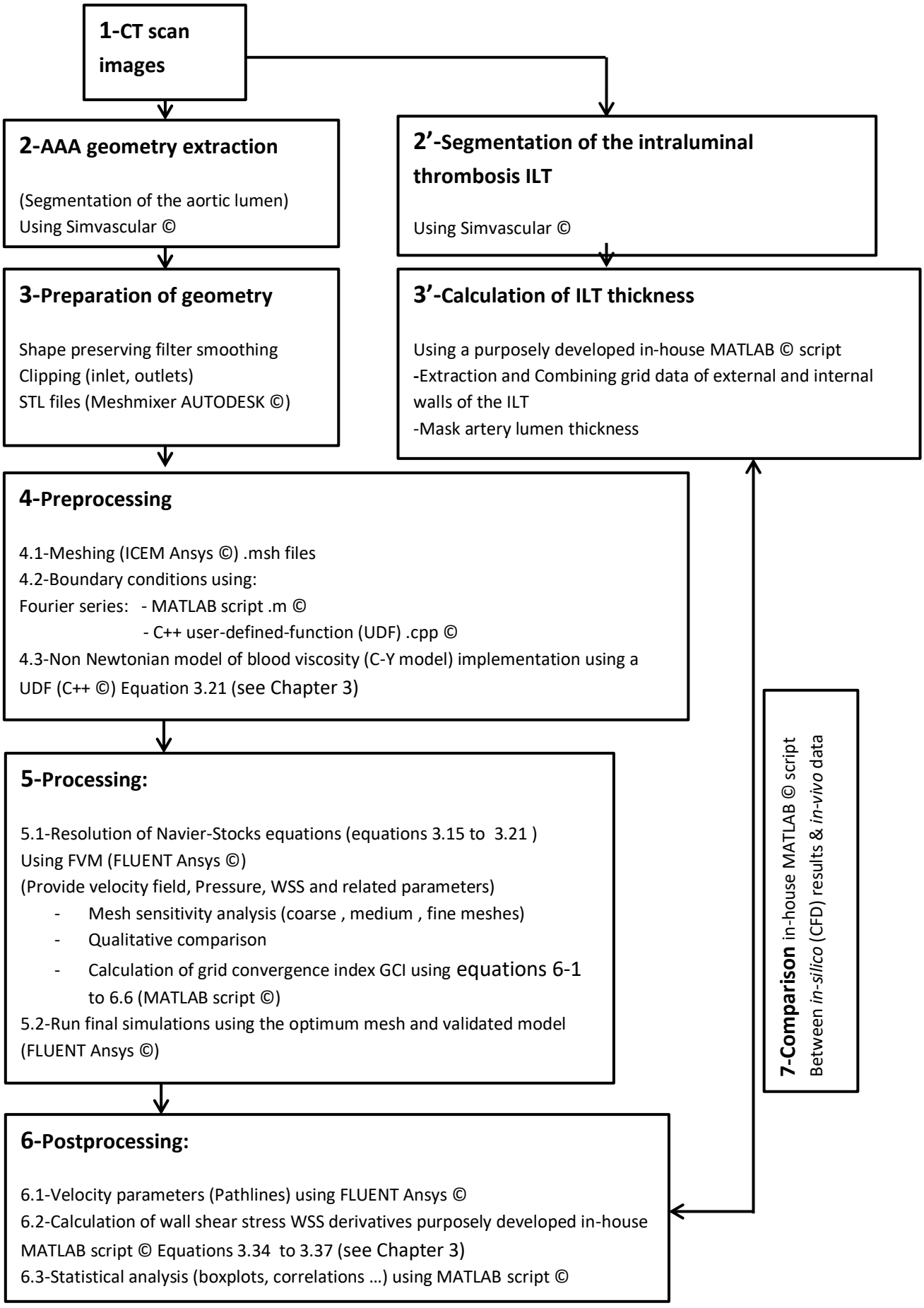

Figure. 4.3 : Flowchart of the methodology used in Chapter 6.

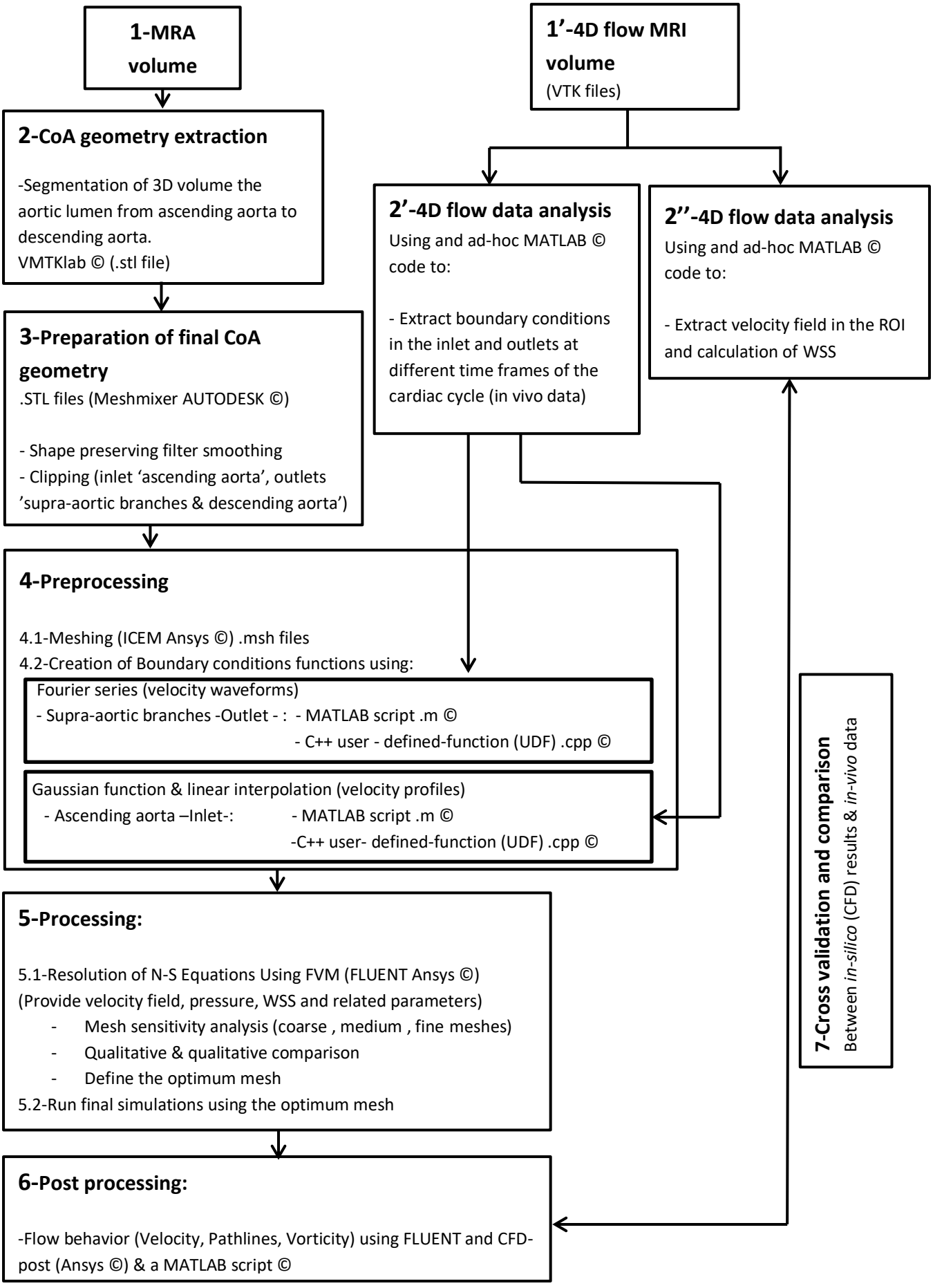

Figure. 4.4 : Flowchart of the methodology used in Chapter 7.

4.3. NUMERICAL MODEL (FINITE VOLUME METHOD (FVM))

In this section, the methodology used by ANSYS Fluent to resolve the governing equations and the configuration of our numerical model is described briefly based on the user guide of this code [111]. More details about the numerical configuration are provided in Appendix A.

ANSYS Fluent use the finite volume method (FVM) to solve the governing N-S equations (conservation of mass and momentum), and (if applicable) for energy and other scalars such as chemical species and turbulence. A basic volume control technique is used which consists of:

• Division of the domain into discrete control volumes (cells) using mesh generation.

• Integration of equations that govern individual control volumes to construct algebraic equations for discrete dependent variables such as velocity, pressure, temperature, and conserved scalars.

• Linearization of the discretized equations and iteratively solving the algebraic equations over each cell in the numerical mesh.

The schemes used are locally and globally conservative. They can be applied whatever the shape of the cells.

4.3.1. Overview of solvers

FLUENT allows us to choose one of two numerical methods:

- Pressure-based solver
- Density-based solver

Historically speaking, the pressure-based approach was developed for low-velocity incompressible flows, while the density-based approach was mainly used for high-velocity compressible flows. However, recently both methods have been extended and reformulated to solve and exploit a wide range of flow conditions.

In both methods, the velocity field is obtained from the equations of momentum. In the density-based solver, the continuity equation is used to obtain the density field while the pressure field is determined from the state equation. On the other hand, in the pressure-based approach, the pressure field is extracted by solving a

pressure correction equation and obtained by manipulating the continuity and momentum equations.

Both numerical methods use a similar discretization process (FVM), but the approach used to linearize and solve the discretized equations is different. In the next section, we will describe in general the two methods and later we will explain in detail the solver that we used in our work .ie. Pressure-based solver.

4.3.1.1. Pressure-based solver

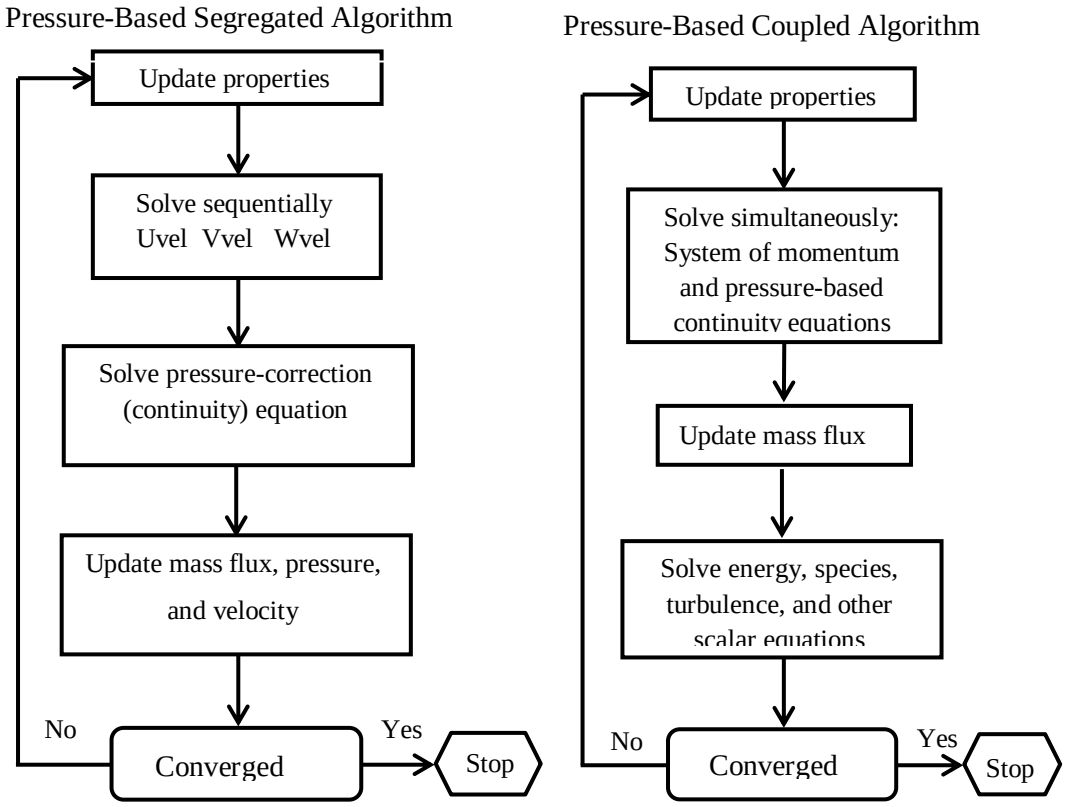

Figure. 4.5: Overview of the Pressure-Based Solution Methods (reedited from [111]).

The pressure-based solver employs an algorithm that belongs to a general class of methods called the projection method. In the projection method, in which the conservation of mass (continuity) constraint of the velocity field is obtained by solving a pressure equation (or pressure correction), the pressure equation is derived from the equations of continuity and momentum such that the pressure-corrected velocity field satisfies continuity. Since the governing equations are not linear and coupled, the resolution process consists of iterations in which the set of governing equations is solved until the solution converges.

4.3.1.2. Density-based solver

The density-based solver solves the continuity and momentum equations and (if applicable) energy transport and species simultaneously (coupled). The governing equations for the additional scalars will be solved subsequently and sequentially (i.e., separated from each other and from the coupled set) according to the procedure described in the next section (discretization). Since the equations are nonlinear and coupled, several iterations of the solution loop must be executed before a converged solution is obtained.

In the density-based solution solver, we can solve the coupled system of equations (continuity, momentum, energy and species equations if available) using either the coupled-explicit formulation or the coupled-implicit formulation.

The way in which equations are linearized can take an implicit or explicit form with respect to the dependent variable (or set of variables) of interest. Implicit or explicit means the following:

• Implicit: for a given variable, the unknown value in each cell is calculated from a relation that includes the existing and unknown values of neighboring cells.

Therefore, each unknown appears in more than one equation of the system, and these equations must be solved simultaneously to give the unknown quantities.

• Explicit: for a given variable, the unknown value is calculated in each cell from a relationship that only includes existing values. Therefore, each unknown appears in only one equation in the system, and the equations of the unknown value in each cell can be calculated once to give the unknown quantities.

4.3.2. The General Transport Equation for Scalars: Discretization and Solution

FLUENT uses a control volume-based technique to convert a general scalar transport equation to an algebraic equation that can be solved numerically. This control volume technique consists of integrating the transport equation over each control volume, resulting in a discrete equation that expresses the conservation law on a volume control basis.

The discretization of the governing equations can be illustrated most easily by considering the unsteady conservation equation for the transport of a scalar

quantity Φ. This is demonstrated by the following equation written in integral form for an arbitrary control volume V as follows:

$$\int_V \frac{\partial \rho\, \Phi}{\partial t}\, dV + \oint \rho\, \Phi \overrightarrow{v}\, d\vec{A} = \oint \Gamma_\Phi\, \nabla\Phi\, d\vec{A} + \int_V S_\Phi\, dV \qquad (4.1)$$

ρ	density
$\vec{v}$	Velocity vector (=u i + v j + w k in 3D)
$\vec{A}$	surface area vector
Γ_Φ	Diffusion coefficient for Φ
$\nabla\Phi$	Gradient of Φ (=$\frac{\partial\Phi}{\partial x} i + \frac{\partial\Phi}{\partial y} j + \frac{\partial\Phi}{\partial z}$ k in 3D)
S_Φ	source of Φ per unit volume

This equation is applied for each control volume in the calculation domain. Figure 4.6 is an example of a two-dimensional triangular control volume. Equation 4.1 applied to a cell gives:

$$\frac{\partial \rho \Phi}{\partial t} V + \sum_f^{Nfaces} \rho_f\, \overrightarrow{v_f}\, \Phi_f\, .\overrightarrow{A_f} = \sum_f^{Nfaces} \Gamma_\Phi\, \nabla\, \Phi_f . \overrightarrow{A_f} + S_\Phi\, V \qquad (4.2)$$

N_{faces}	Nombre of faces which enclose the cell
Φ_f	Value of Φ convected through the surface f
$\rho_f\, \overrightarrow{v_f}\, \overrightarrow{A_f}$	Masse flux through the face f
$\overrightarrow{A_f}$	Area of the face f , $\lvert A\rvert$ $(= A_x\, i + A_y\, j + A_z\, k\ in\ 3D)$
$\nabla\, \Phi_f$	Gradient of Φ through f
V	Volume of the cell

With $\frac{\partial \rho \Phi}{\partial t} V$ is defined in the temporal discretization section. The equations solved by FLUENT take the same general form as the one given above and are easily applied in multi-dimensional cases, unstructured meshes and composed of arbitrary polyhedra.

The discretized transport equation of the scalar (equation 4.2) contains the unknown scalar variable Φ at the center of the cell, as well as the unknown values in surrounding neighboring cells. A linearized form of equation 4.2 is written (see Appendix A in the section “Solving the Linear System”). Analogous equations can be written for each grid cell. This results in a set of algebraic equations. For scalar

equations, FLUENT solves this linear system using an implicit point (Gauss-Seidel) linear equation solver in conjunction with an algebraic multi-grid (AMG) method.

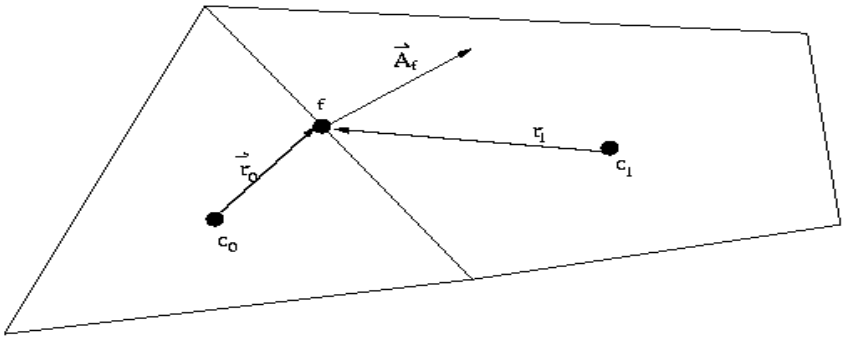

Figure. 4.6: Control volume used to illustrate the discretization of a scalar transport equation.

4.3.3. Discretization

4.3.3.1. Spatial discretization

FLUENT stores the discrete values of the scalar Φ in the cell centers (c0 and c1 Figure 4.6). However, the values in the face f are required for the convection terms in equation 4.1 and must be interpolated from the cell center values. This is accomplished using an upwind scheme.

For steady flow, equation 4.1 becomes:

$$\sum_f \rho_f \overrightarrow{A_f} \cdot \overrightarrow{A_f} \Phi_f - \sum_f \Gamma_f (\nabla \Phi)_f \cdot \overrightarrow{A_f} = \overrightarrow{S_\Phi} \Delta\Omega \qquad (4.3)$$

$\sum_f \rho_f \overrightarrow{A_f} \cdot \overrightarrow{A_f} \Phi_f$: Convection Terme

$\sum_f \Gamma_f (\nabla \Phi)_f \cdot \overrightarrow{A_f}$: Diffusion Terme

Upwinding means that the values on the faces ϕ_f are derived from the values in the cell downstream or relative to the direction of normal velocity vn . FLUENT allows you to choose between several Upwind schemes: 1st order upwind scheme, second order upwind scheme, power scheme and Quick.

In our case, we opted for the 2nd order UPWIND scheme, which has already been used in other studies similar to ours (for more details see chapters 5, 6 and 7), and for the advantages that will be mentioned below compared to the other schemes:

When second-order accuracy is desired, the quantities at the cell faces are calculated using a multidimensional linear reconstruction approach. In this approach superior accuracy is achieved at the cell faces by a Taylor series extension of the solution centered on the cell around the center of the cell's surface. So when the second-order upwind scheme is selected, the value at the center of the face ϕ is calculated using the following expression:

$$\Phi_{f,sou} = \Phi + \nabla \Phi . \vec{r} \qquad (4.4)$$

Where Φ and $\nabla\Phi$ is the value at the center of the cell and its gradient in the upstream cell, and $\vec{r}$ is its displacement vector from the center of the considered cell. This formulation requires to calculate the gradient $\nabla\Phi$ in each cell (as we will see later in section: Calculation of gradients and derivatives). Finally, the gradient $\nabla\Phi$ is limited so that there is no introduction of new minima or maxima.

4.3.3.2. Temporal discretization

For transient simulations (or unsteady which is the case of our study), the governing equations must be discretized in space and time. The spatial discretization of the time-dependent equations is identical to the stationary case. Temporal discretization involves the integration of each term in the differential equations over a time step Δt. Integrating transitional terms is straightforward, as shown below.

A generic expression for the temporal evolution of a variable is given by:

$$\frac{\partial \Phi}{\partial t} = F(\Phi) \qquad (4.5)$$

Where:

$$F(\Phi) = \frac{1}{\Delta\Omega}\left[\sum_f - \rho_f \overrightarrow{v_f} . \overrightarrow{A_f}\, \Phi_f + \sum_f \Gamma_f \, (\nabla\Phi)_f . \overrightarrow{A_f} + \overline{S_\Phi}\, \Delta\Omega\right] \qquad (4.6)$$

To discretize, we have two schemes: the first-order and the second at second-order schemes. If the time derivative is discretized using backward differences, the first-order time discretization is given by:

$$\frac{\Phi^{n+1} - \Phi^n}{\Delta t} = F(\Phi) \qquad (4.7)$$

And the second-order temporal scheme gives:

$$\frac{3\,\Phi^{n+1} - 4\,\Phi^n + \Phi^{n-1}}{2\,\Delta t} = F(\Phi) \qquad (4.8)$$

Φ = the scalar quantity

n + 1 = value at t + Δt

n = value at the current time t

n -1 = value at the precedent time step t- Δt

Once the time derivative has been discretized, it remains to choose how to evaluate F(ϕ): in particular, at what time step should we consider ϕ to calculate F.

Time integration

The method consists in evaluating F(ϕ) at the future time step n+1 (see equations in section ”Implicit time integration” in appendix A). This implicit equation can be solved iteratively at each time step before proceeding to the next step n+1.

The advantage of this scheme is that it is totally implicit and that it is unconditionally stable whatever the time step.

4.3.3.3. Gradients and derivatives evaluation

Gradients are not only needed to construct scalar values on cell faces but also to calculate secondary diffusion terms and velocity derivatives. The gradient of a variable ϕ is used to discretize the convection and diffusion terms in the flow conservation equations.

Gradients in FLUENT are calculated using three methods:

- Green-gauss cell-based
- Green–gauss node-based
- Least squares cell–based

Details about the methods used in our study could be found in appendix A (see section “Gradients and derivatives evaluation” in Appendix A).

4.3.4. Pressure-based solver

In this section, we will see the procedures related to the discretization of the momentum and continuity equations and their solution by means of the pressure-based solver. These procedures are described by considering the continuity and momentum equations written in integral form:

$$\oint \rho \ \vec{v} \ . d\vec{A} \ = 0 \qquad (4.9)$$

$$\oint \rho \, \vec{v} \, \vec{v} \, . d\vec{A} = - \oint p \, I \, . d\vec{A} + \oint \bar{\bar{\tau}} \, d\vec{A} + \int_V \vec{F} \, dV \qquad (4.10)$$

Where I is the identity matrix, $\bar{\bar{\tau}}$ is the stress tensor and F is the force vector.

4.3.4.1. Discretization of momentum and continuity equations

The discretization schemes seen previously in the discretization section are used to discretize momentum and continuity equations. The whole discretization methodology of both momentum and continuity equations are detailed in appendix A respectively in sections “discretization of the momentum equation“ and “discretization of the continuity equation”.

Pressure interpolation schemes in momentum equation

FLUENT uses a co-located scheme. In this diagram, the pressure and the velocity are stored at the center of the cells.

However, the discretized form of the momentum equation requires knowing the value of the pressure on the face between cells; therefore, an interpolation scheme is necessary to calculate the values of the pressure at the faces of the cells.

By default the interpolation scheme interpolates the pressure on the face using the coefficients from the momentum equation. By comparing the different existing methods, we had the choice between the PRESTO scheme and the second-order scheme. The two scheme where used in our numerical model in the chapters 5, 6 and 7. For more details about the two schemes (.ie. PRESTO and second-order) see the appendix A.

Interpolation scheme for density

For incompressible flows, FLUENT uses an arithmetic mean to calculate the density, which is the case for our simulations.

4.3.4.2. Velocity-pressure coupling

The velocity-pressure coupling is obtained by using the equation (A.19) (see appendix A) to derive an additional condition for the pressure by reformulating the continuity equation. The pressure-based solver allows the problem to be solved either by a segregated or coupled manner. FLUENT allows the choose between five velocity-pressure coupling algorithms: SIMPLE, SIMPLEC, PISO, Coupled, and for

unsteady flows using the non-iterative temporal progression scheme (NITA) Fractional Step (FSM). All the schemes cited below, except the coupled scheme, are based on the predictor-corrector approach.

The SIMPLE and PISO schemes were chosen for the velocity-pressure coupling, given the advantages they presents and by referring to previous similar studies (see chapters 5,6 and 7 for more details). Details about the two used schemes (.ie. SIMPLE and PISO) are provided in appendix A.

4.3.4.3. Time advancement algorithm

For time-dependent flows, the discretized form for the generic transport equations is of the form:

$$\int_V \frac{\partial \rho \Phi}{\partial t}\, dV + \oint \rho \Phi\, \overrightarrow{v}\, .\, d\vec{A} = \oint \Gamma_\Phi\, \nabla \Phi\, .\, d\vec{A} + \int_V S_\Phi\, dV \qquad (4.11)$$

$\frac{\partial \rho \Phi}{\partial t}$	Conservative form of transient derivative of transported variable Φ
ρ	Density
$\vec{v}$	Velocity vector (= $u\,\hat{\imath} + v\,\hat{\jmath} + w\,\hat{k}\ (in\ 3D)$
$\vec{A}$	Surface area vector
Γ_Φ	Diffusion coefficient for Φ
$\nabla \Phi$	gradient of Φ ($\Phi = {}^{\partial \Phi}/_{\partial x}\, i + {}^{\partial \Phi}/_{\partial y}\, j + {}^{\partial \Phi}/_{\partial z}$ k in 3D)
S_Φ	source of Φ per unit volume

The temporal discretization of the transient derivative in equation 4.11 is described in the section “temporal discretization” (equations 4.5 to 4.8). The solver based on the pressure uses an implicit discretization of the equations of transport (equation 4.11). By default, the standard approach allows the evaluation of the convective, diffusive and source terms from the field at time n+1:

$$\int_V \frac{\partial\, \rho\, \Phi}{\partial t} dV + \oint \rho^{n+1}\, \Phi^{n+1}\, \overrightarrow{v^{n+1}}\, \overrightarrow{dA} = \oint \Gamma_\Phi^{n+1}\ \nabla \Phi^{n+1}\, d\, \vec{A} + \oint S_\Phi^{n+1}\, dV \qquad (4.12)$$

In the pressure-based solver, the overall temporal discretization error is determined by the choice of temporal discretization (e.g., first-order, or second-order) and the way in which are advanced in time (time advancement scheme). The

process of solving the separate algorithm solves each equation alone and introduces errors known as "divisions"

There are two approaches to time advancement, depending on how you control the error of the Iterative Time-Advancement scheme and non-Iterative Time-Advancement scheme divisions. The first scheme is the one we have chosen in our study, it is defined in the paragraph below.

In the pressure-based solver, the overall time discretization error is determined both by the choice of time discretization (e.g., first order, second order) and how solutions are advanced to the next time step (time-advancement scheme). The temporal discretization introduces the corresponding truncation error; for the first and second order. The segregated solving process by which equations are solved one by one introduces splitting error. There are two approaches to the time-advancement scheme depending on how you want to control the splitting errors.

Iterative Time-Advancement scheme

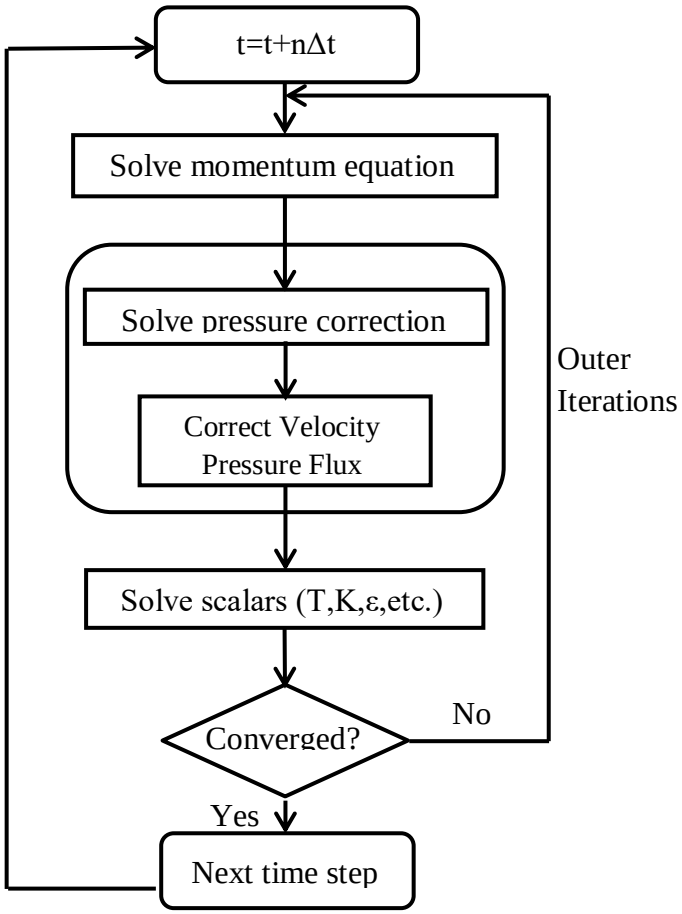

Figure. 4.7: Overview of the Iterative Time Advancement Solution Method For the Segregate Solver (reedited from [111]).

In the iterative scheme, all equations are solved iteratively for a given time step until reaching the convergence criterion. So advancing the solution for a one-time step normally requires a number of external iterations as shown in the figures (flowchart of pressure-based solver see figure 4.5 and the figure 4.7). With this iterative scheme, the non-linearity of the equations and the coupling between the equations are fully taken into account, thus eliminating the “splitting” error. The iterative scheme is the default in FLUENT.

Chapter 5

Flow Behaviour and Wall Shear Stress Derivatives in Abdominal Aortic Aneurysm Models: a Detailed CFD Analysis into Asymmetry Effect.

5.1. INTRODUCTION

Abdominal aortic aneurysm (AAA) is characterized by a deformation and a localized dilatation of the abdominal aorta (usually infrarenal) to at least one and a half times the diameter of the healthy aorta. AAA is one of the most common cardiovascular diseases, with a prevalence of 6-8 % for people over 65 years old, reaching up to 10% for 80 years old male subjects [81]. The average prevalence of AAA was 5.7% in the literature until February 2013 [115]. A complication of AAA is a sudden rupture, and this accounts for up to 4 to 5% of all sudden deaths according to Schermerhorn *et al.,* [116], and is ranked as the 14th most common cause of death in the world [117].

AAA is also characterized by a high mortality rate during and after surgery [118] which prompted some authors to suggest that subgroups of patients might be excluded from surgery [119]. In the US, the incidences of AAAs reach up to 55,000/year and the incidence of AAA rupture is 10,000 [120]. Sakalihasan and colleagues [121] reported that the number of deaths caused by ruptured aneurysms is about 8,000 and 15,000 patients in the UK and in the USA respectively.

Assessing the risk of rupture is extremely important in reducing AAA mortality. Currently, the most commonly used criterion to select eligible patients for surgery relies on the measurement of the AAA maximum diameter [3,122]. Surgery is recommended when the maximum diameter reaches 5.5 cm [123,124]; however many surgeons have observed that some AAAs became greater (11 or 12 cm) and remained unruptured, whilst others were smaller (<5.5cm) could break abruptly [124]. This evidence suggests there is a need to better stratify the risk for AAA rupture by determining additional criteria to help surgeons make clinical decisions regarding surgical intervention and management of patients with AAA.

Several researchers have studied the effect of aneurysm geometry and the mechanical behaviour of the wall on hemodynamic forces [11,125,126].The fact that AAA is often associated with deposition of blood clots and cell debris in the intraluminal thrombus (ILT), as well as the breakdown of connective tissue in the wall, which plays an important role in rupture and remodelling of the wall, makes the fluid dynamics in AAA, including the evolution of velocity and wall shear stress, a very promising index to improve prediction of AAA rupture.

Several numerical studies show that, compared to reconstructed geometries from medical imaging, virtual aneurysm models are more useful for parametrical studies [5,4]. The use of idealized geometry was adopted in many studies concerning AAA [4,5,9,11,127,128] and other cardiovascular diseases [129,130]. The models do not preserve the physiologically correct geometry, but they still retain important physical processes that occur in an AAA [131].

Some numerical studies have been done on the hemodynamic characteristics of symmetric and asymmetric idealized models [132], and experimental modelling studies have been carried out by Salsac *et al.,* [4]. The study by Finol *et al.,* [133] was devoted to the understanding of the relation between the aneurysm asymmetry and the WSS distribution. In Soudah *et al.,* [132] many geometric parameters including the asymmetry were tested.

In this work, the relationship between hemodynamic and WSS during the cardiac cycle for different symmetric and asymmetric geometries of aneurysm was studied. To the best of our knowledge, this is the first study to provide a detailed analysis in idealized symmetric and asymmetric aneurysms, including flow behaviour, WSS, vorticity, oscillatory shear index (OSI), and time averaged wall shear stress (TAWSS), which are very important factors for the understanding of thrombus formation and rupture risk evaluation.

5.2. METHODOLOGY

The flowchart used was shown in Chapter 4 (see Chapter 4 Figure 4.2). All the steps will be details in the following sections.

5.2.1. Geometries

The adopted geometries have a diameter of $\mathrm{d} = 2\mathrm{cm}$ in inlet and outlet, and a maximum diameter of $\mathrm{D} = \mathrm{DAAAmax} = 3\mathrm{d}$ in the median section of the AAA sac (see Figure 5.1). The asymmetry ratio β is:

$$\beta = \frac{r}{R} \tag{4.1}$$

where r is the radius measured at the medial section of an AAA sac from the longitudinal part toward the posterior part and R is the radius measured at the medial section of an AAA sac from the longitudinal part toward the anterior part. β=1 corresponds to a symmetric AAA.

The aneurysm lumen geometry is given by:

$$\varphi(z) = \begin{cases} d\left(\cos\left(\frac{\pi}{3d}(z-6d)+2\right)\right) & \begin{cases} 3d \le z < 9d \\ 0 \le z < 3d \ and \ 9d \le z < 12d \end{cases} \\ d \end{cases} \quad (5.2)a$$

$$\delta(z) = \frac{3}{4}\left(\frac{1-\beta}{1+\beta}\right)(\varphi(z) - d) \quad (5.2)b$$

Where $\varphi(z)$ define the diameter of the aneurysm sections along the aorta (axis z) and $\delta(z)$ define its deviation from the center (Figure 5.1).

$\beta = \{0.2, 0.4, 0.6, 0.8, 1\}$ Has been considered, corresponding to five different geometries of AAA as proposed by Scotti *et al.,* [6].

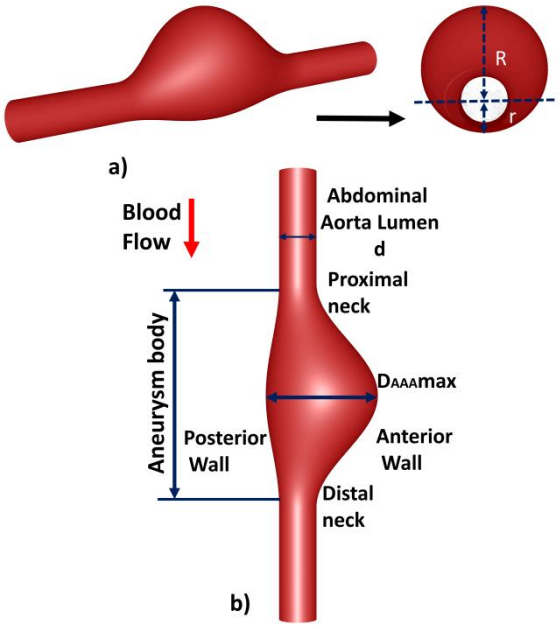

Figure. 5.1. Geometry of the AAA models (asymmetric model with asymmetry ratio β =0.4 is Model is illustrated) (a) Cross section (b) Vertical section.

5.2.2. CFD simulation

Mesh sensitivity studies were performed with the aim of defining the optimum computational domain for each AAA models. The software Gambit 2.4.6 (Ansys Inc.) was used for the mesh generation. For the symmetric model (SM), the mesh was

changed from 886950 elements (1068637 nodes) to 1503607 elements (1777500 nodes), and from 888973 elements (1070657nodes) to 1475241 elements (1744138 nodes) for the AM. The resolution of the boundary layer, as shown in Figure 5.2-b, was adapted near the wall and the cell adjacent to the wall satisfied Eq. (5.3); this ensures accurate estimations of velocity gradients, and wall shear stresses near the wall. The optimum mesh size was determined once the peak wall shear stress does not increase by more than 2%. Based on this analysis, the final hexahedral meshes' grids were constructed (# β=0.2 (AM): 1,241,376 elements; # β=0.4: 1,204,320; # β=0.6: 1,176,528; # β=0.8: 1,162,632; # β=1 (SM): 1,148,736).

$$y_p\sqrt{\frac{v_\infty}{\upsilon\, x}} \leq 1 \tag{5.3}$$

where y_p is the distance between the wall and center of the adjacent mesh cell, v_∞ is the free-stream velocity, υ is the kinematic viscosity of the fluid and x is the distance along the wall from the starting point of the boundary layer.

The workstation used to perform the simulations in this work is with two Xeon E5-2660 processors and 16 GB of RAM. The run time was 69 hours and 33 minutes for each cardiac cycle in the case of the SM, and approximately 81 hours and 9 minutes for the AM. Five cardiac cycles were simulated to minimize the influence of initial conditions, and the last cycle was considered in our results.

A no-slip boundary condition was imposed at the wall supposing that it is rigid. In fact, the wall of the AAAs become stiffer following the loss of elastin [14] and their compliance is nearly negligible compared to a healthy aorta [15]. This hypothesis was adopted in many studies concerning aorta and AAA [128,129;62-138].

At the geometry inlet, a pulsatile velocity is applied (Figure 5.2-a) which is justified by the fact that this condition is applied to the unexpanded section of the anterior portion of the abdominal aorta [133] and a free pressure boundary condition was imposed at the geometry outlet. These hemodynamic conditions were referred to in previous studies [94]. The temporal variations of these physiological velocity inlet conditions were reproduced by Fourier series of order 16th for velocity and implemented through a User_Defined_Function (UDF) script (see appendix B1).

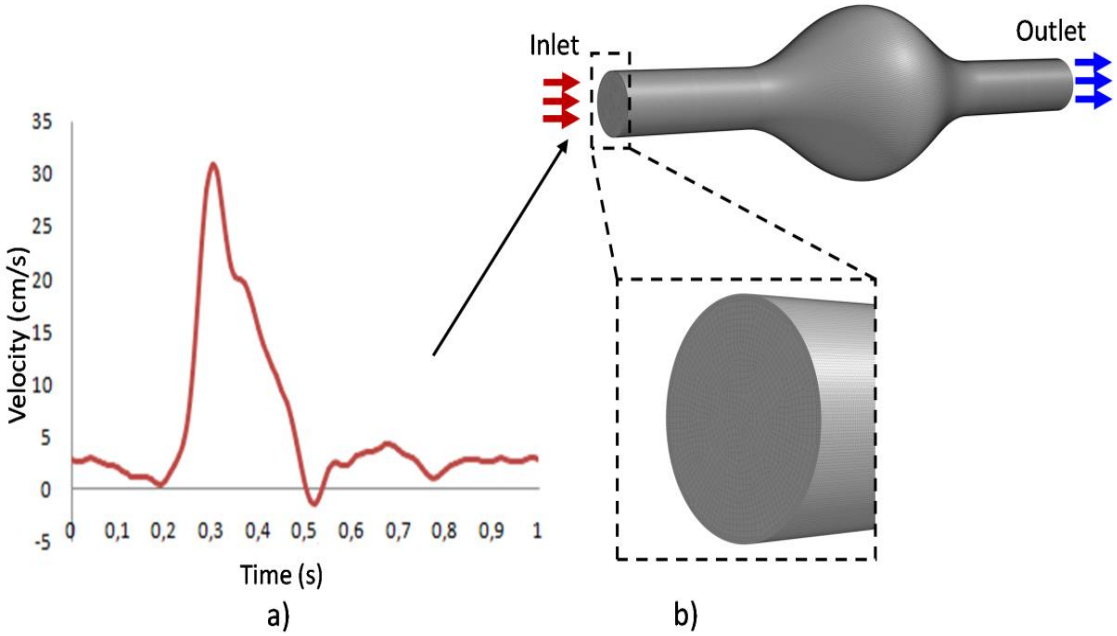

Figure. 5.2. Boundary conditions (a) Velocity waveform and (b) Boundary layer mesh (SM β =1 is illustrated).

In order to avoid numerical instabilities, the inlet and outlet boundaries were extended by three times the diameter of the healthy part of the aorta (Figure 5.1). The natural frequency of the pulsatile flow is set to $\omega = 2\pi \text{ rad/s}$, with a period $\text{T} = 1\text{s}$.

5.2.3. Governing Equations

Even if blood is a suspension of cells in plasma [94], in large-sized vessels, the non-Newtonian behaviour of blood is limited [104], and it begins to play a role in vessels smaller than 1 mm in diameter [97]. Pedley *et al.,* [105] shows that in vessels greater than approximately 0.5 mm in diameter it is reasonable to model blood as a Newtonian fluid.

This assumption was adopted in most of the previous works, where blood is considered as an incompressible and Newtonian fluid, with a homogeneous dynamic viscosity of 0.0035 $Pa.s$, and density of 1050 kg/m^3 [62, 107]. The flow in the abdominal aorta is hence described by the incompressible Navier-Stokes and continuity equations (see chapter 3 equations 3.15 and 3.16).

In this study the Finite Volume Method (FVM) was adopted to solve the governing equations and to predict the time-dependent flow through three-dimensional abdominal aortic aneurysm geometry by using Fluent (Ansys, Inc.) with the implicit solver. A second-order upwind scheme was used for spatial discretization and the PISO (implicit operator splitting pressure) algorithm for pressure-velocity coupling. The time-step size was taken equal to 10^{-3}s, which is equivalent to 1000 time-steps for each cardiac cycle using the iterative time advancement scheme. The convergence criteria for the continuity and the velocity are in the order of 10^{-6} and 10^{-5}, respectively.

5.2.4. CFD Validation

To validate our numerical model, we performed a comparison of the axial velocity profile at the center of the aneurysm with the experimental and numerical data of Budwig *et al.,* [139] for steady flow through the axisymmetric AAA model (as shown in Figure 5.3b and Figure 5. 3c). The simulations are carried out at Re = 400, aneurysm-to-artery diameter ratio D/d=2.1, and an aspect ratio of the aneurysm L/d=4 (L is the length of the aneurysm). The results generated in the present numerical simulation show good agreement with the experimental and numerical results [139]. The flow feature characterized by the formation recirculating vortex was in agreement with in vitro studies [139] (as shown in Figure 5.3-b). The shape of the aneurysm was not detailed in [139]. The slight difference in our velocity profile (in which the dome of the profile is slightly larger) compared [139] could be due to the possible difference in the shape of our aneurysm, experimental and numerical results.

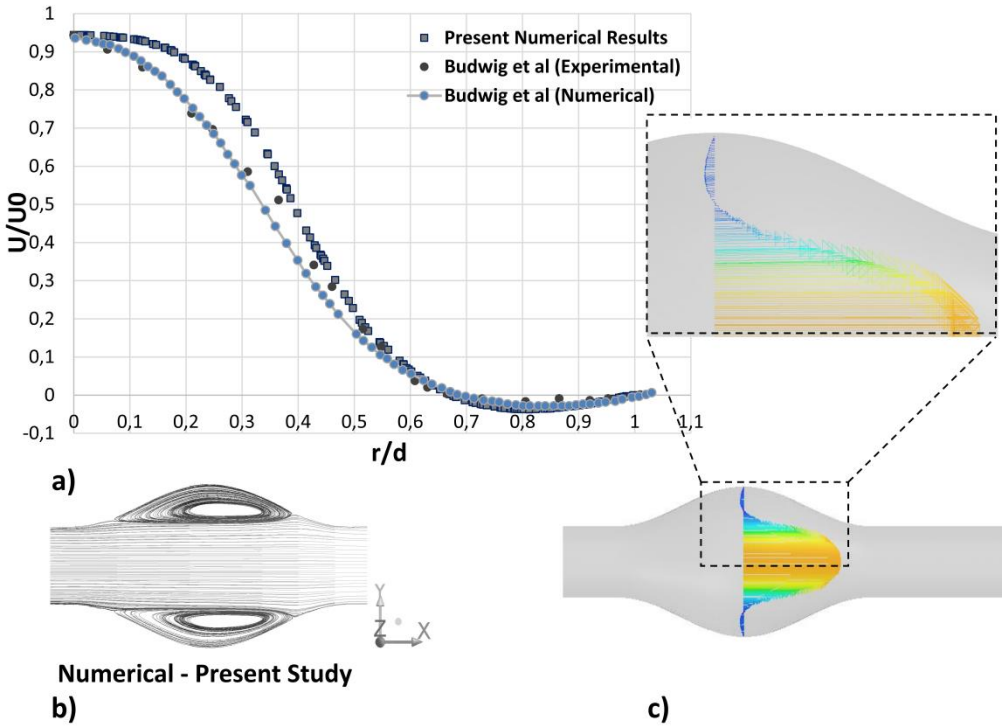

Figure 5.3. Model with Re=500, R⁄r0 = 2.1 and L⁄r0 = 8. (a) Comparison of steady profile across the centre of the AAA with experimental and numerical results, (b) Streamlines using present numerical model and (c) Profile across the centre of the AAA.

5.3. RESULTS

5.3.1. Flow Behavior in an AAA

Figure 5.4-a shows the general features characteristics of the flow with reference to the symmetric aneurysm (β= 1). At the inlet of the aneurysm (distal neck), a jet is formed and enters into the aneurysmal sac; this result is in perfect agreement with the experimental results of Deplano *et al.,* [140]. The velocity gradient between the jet flow and the surrounding parts produces shear layers; generating vortices detected in the horizontal and vertical vorticity contours and in velocity vectors (see Figures 5.4 and 5.5).

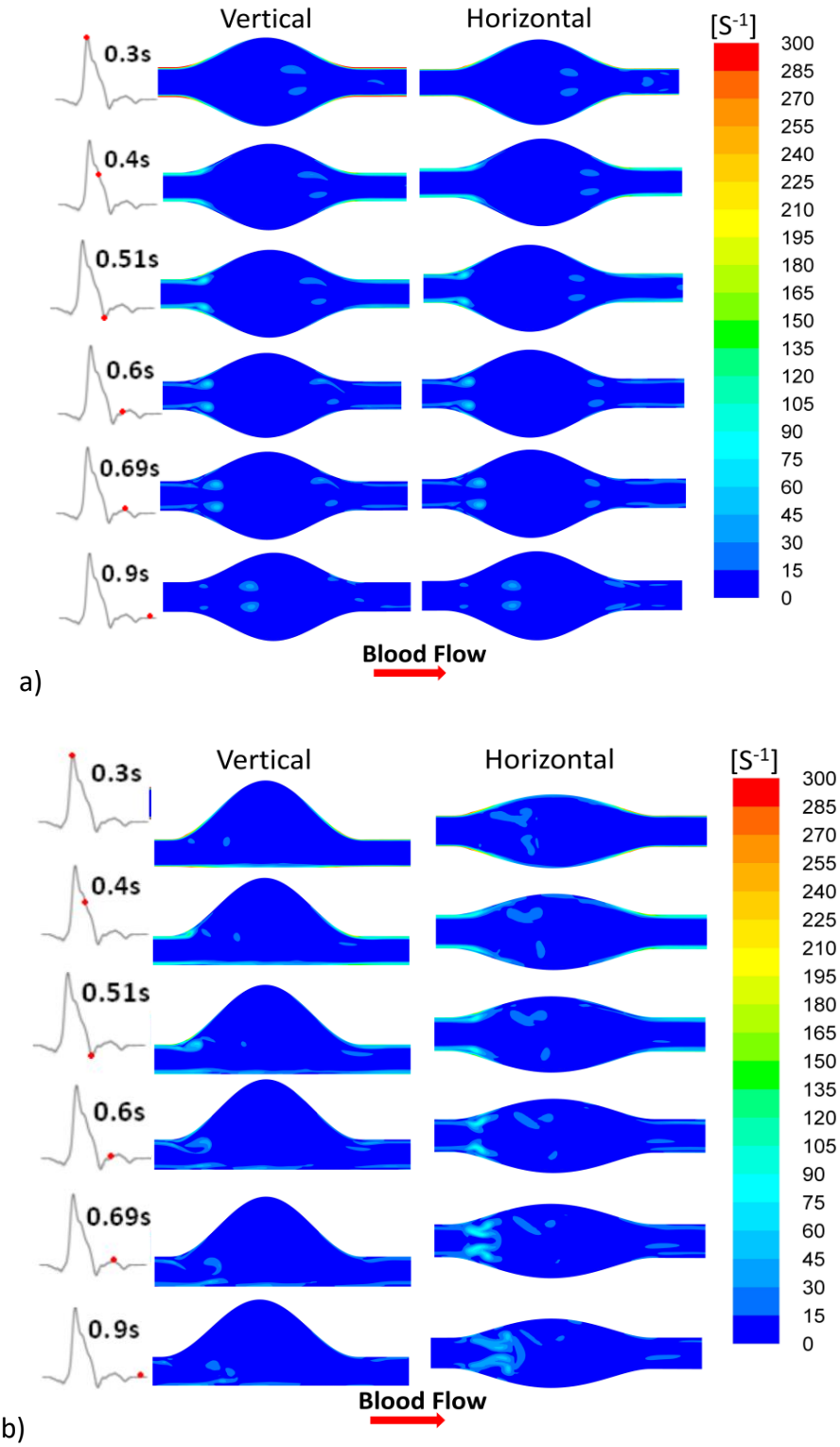

Figure. 5.4. Vorticity temporal evolution [s-1] for (a) Symmetric Model (SM) and (b) Asymmetric Model (AM), in vertical and horizontal planes respectively.

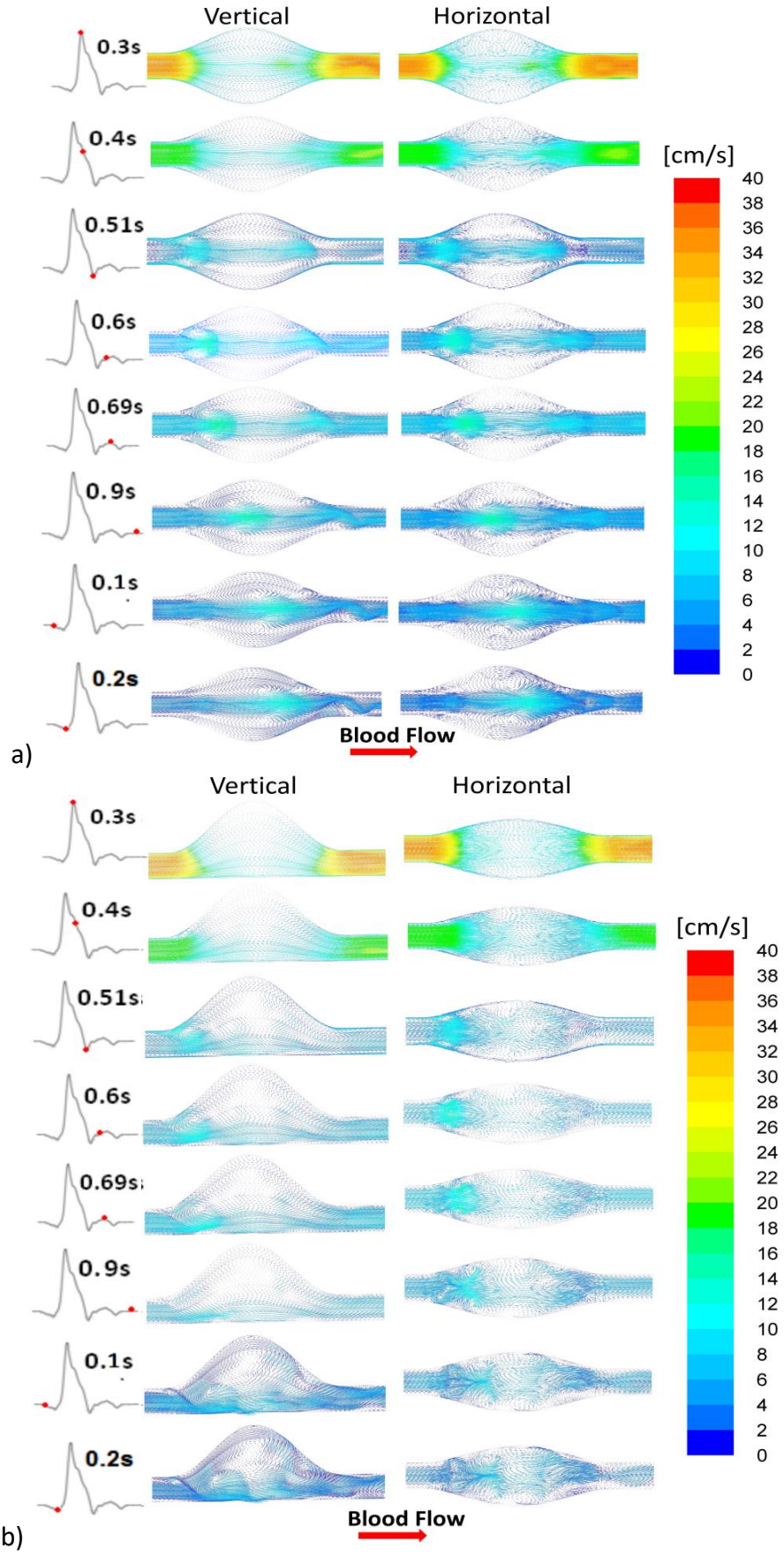

Figure. 5.5. Velocity vectors temporal evolution [cm/s] for (a) Symmetric Model (SM) and (b) Asymmetric Model (AM), in vertical and horizontal planes respectively.

The general characteristics of the flow in our results, the vortex formation, the impingement of the jet and regions of high and low WSS, are in good agreement with those in prior experimental studies [131, 140].

5.3.2. Flow Dynamics and vortical structure discussion

The effect of the asymmetry on the flow patterns and vortical structures is shown in Figure 5.6 where the time evolution of 3D vortical structures by the iso-surfaces of $\lambda 2$-Criterion Jeong and Hussain [141] is reported.

According to the results presented in the previous section, the aneurysm asymmetry is directly proportional to the earlier separation of the flow, and the vortex occurring in asymmetric aneurysms persist for a longer period compared to those occurring in symmetric aneurysms; in particular, these vortices persist throughout the cardiac cycle for the completely AM. This persistence is due to the separation of the fluid caused by the abrupt change of the section creating areas with large velocity gradients, the velocity gradient produces a stronger vortex. For the AM, the vortices which are produced during the deceleration phase are still present at the diastolic peak and roll-up from the proximal neck (enlargement) impinging on the distal neck (narrowing) (see Figure 5.6).

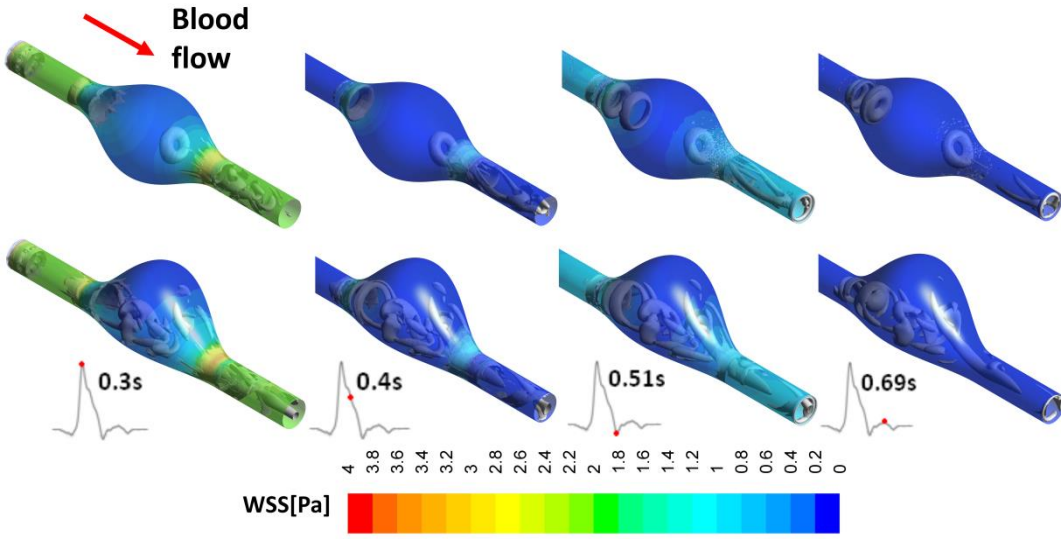

Figure. 5.6. Temporal iso-surfaces of $\lambda 2$-Criterion with threshold value of -10 [s^{-2}] with wall colored by WSS [Pa] at t=0.3, 0.4, 0.51 and 0.69 respectively from left to right. [SM: upper line and AM: Lower line].

In the SM, the vortex ring (VR) starts from the proximal neck during the acceleration phase and is transported along the bulb of the aneurysm to the distal neck. The shape of the VR is conserved and does not change until the end of the cycle. A different behaviour is observed in the Figure 5.5-b, which represents the temporal evolution of the vortex structure in the case of an AM. In the asymmetric aneurysm, the vortex core spreads across the bulb and impacts the distal/anterior wall forming fluctuation zones.

As shown in Figure 5.7, in the case of AM with symmetry factor equal to 0.6, the VR starts to form at t=0.3s (systolic peak) in the proximal neck, and its shape becomes complete at t=0.45s. Considering this time frame as the starting instant of the VR, Figure 5.7 demonstrates its persistence until the same time frame of the next cardiac cycle; however, its shape is lost at t=0.3s and the ring opens close to the posterior wall. This evidence confirms that the shape and the persistence of the VR are in an inverse relationship with the asymmetry of the aneurysm.

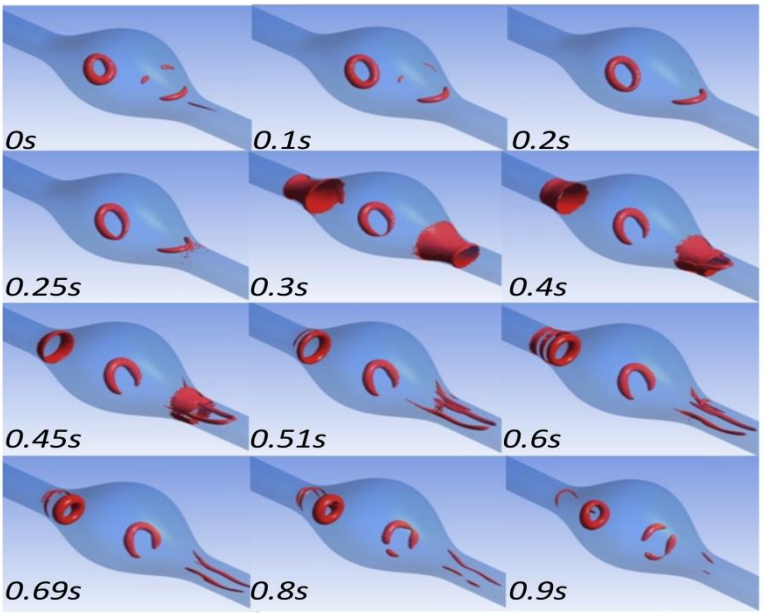

Figure. 5.7. Temporal iso-surfaces of swirling strength using a threshold value of 10 [s^{-1}] for the model β =0.6.

5.3.3. Wall Shear Stress Analysis

In addition to the endothelial layers' thrombogenic function, they are also the mechano-detecting elements which detect the local blood flow conditions and induce autocrine stimulation. In vivo and in vitro studies demonstrate the

destructive effect of low and oscillatory WSS on the endothelial function [97] and their effect on intimal thickening [142]. Under physiologic shear stress, the endothelial cells are aligned to the flow direction, which differs from the low shear stress case [97, 64]. Regions of low WSS are also associated with rupture and expansion sites of the AAAs [65, 143]. The high level of WSS leads to athero-protective endothelial phenotype and decreases the expression of the vasoconstrictor [97].

Many hemodynamic wall parameters including WSS and OSI [112], and TAWSS were documented. An in-house MATLAB code (The Mathworks Inc.) was used for the post-processing and the calculation of those parameters [114].

In detail, WSS, TAWSS and OSI are defined in chapter3 (see equations 3.22 & 3.23).

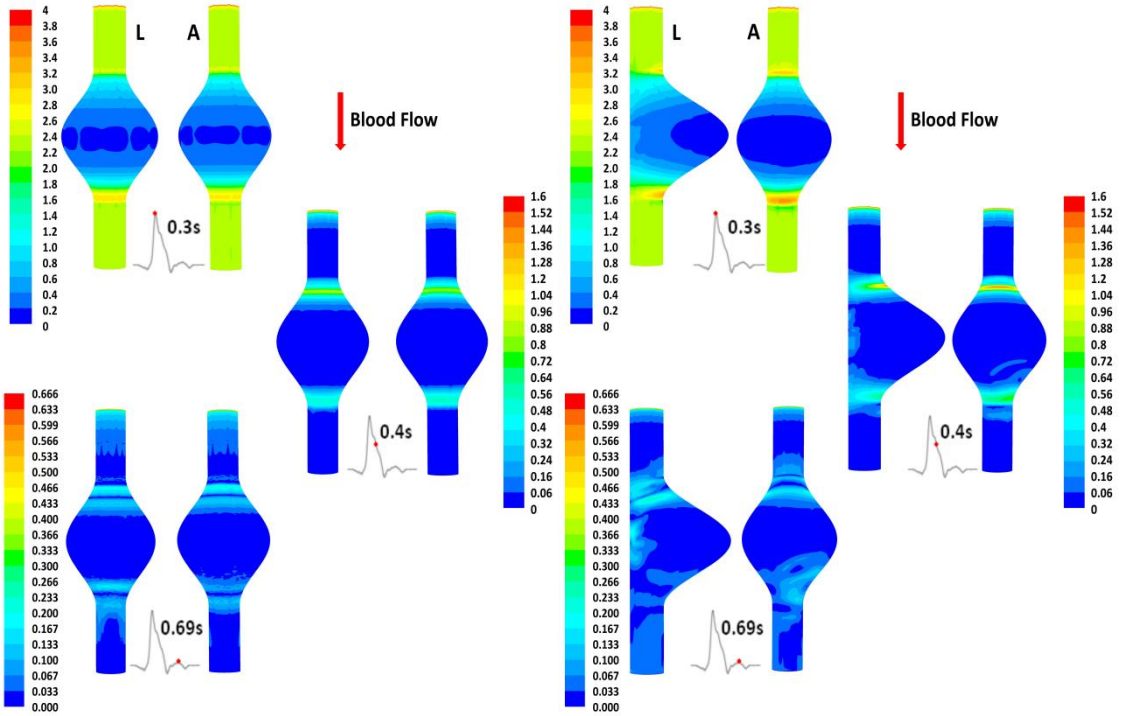

(a) (b)

Figure. 5.8. WSS contours [Pa] in vertical and horizontal plane respectively in (a) SM and (b) AM: at t=0.3s systolic peak, at t=0.4s and at diastolic peak t=0.69s.

Figures 5.8 and 5.9 show the contours of WSS in the SM and AM across three instances of the cardiac cycle. By analysing these figures, it can be observed that during systolic acceleration, WSSs are greater in the healthy part of the aorta (the unexpanded part) than in the wall of the aneurysm sac, which remains in this

condition until it reaches WSS-max at the systolic peak t=0.3s; this observation is valid both for symmetric and asymmetric aneurysm models. The distal and proximal necks are subjected to very high WSS, in contrast to the sac of the aneurysm where low WSS occur. During the deceleration phase, the WSS-max values are still in the two necks, and this configuration persists for the remaining period of the cardiac cycle (see Figures 5.8-a and 5.8-b at t=0.69s).

Figures 5.9-a to 9f show the time evolution of WSS in the five aneurysm models. By analysing this figure, it can be observed that the WSS curvature in the proximal neck is almost the same in the anterior wall represented by P1 (Figure 5.9-a), and in the posterior wall, represented by P1' (Figure 5.9-b). In the aneurysm sac, the anterior wall (Figure 5.9-c) is subjected to WSSs that are lower than those experienced by the posterior wall (Figure 5.9-d); also, in this case, the WSS-max becomes lower on the anterior wall when the level of asymmetry increases. By contrast, in the distal neck, the WSSs are highest in the anterior wall (Figure 5.9-e) than in the posterior one (Figure 5.9-f).

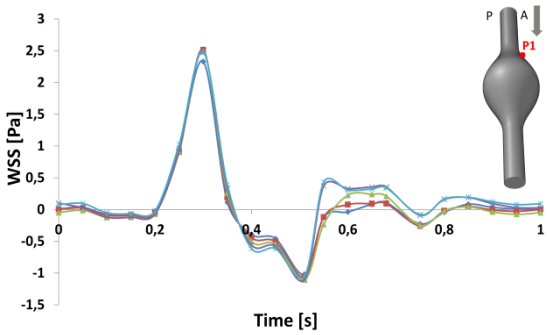

(a) In proximal neck / anterior wall (P1)

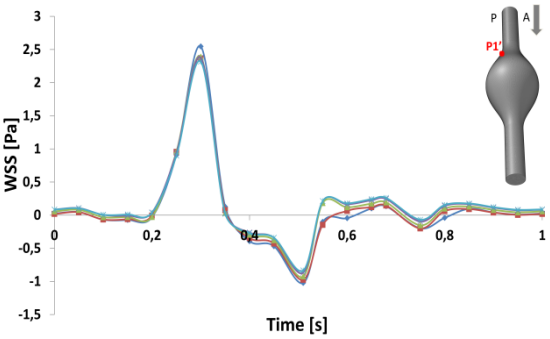

(b) in proximal neck / posterior wall (P1')

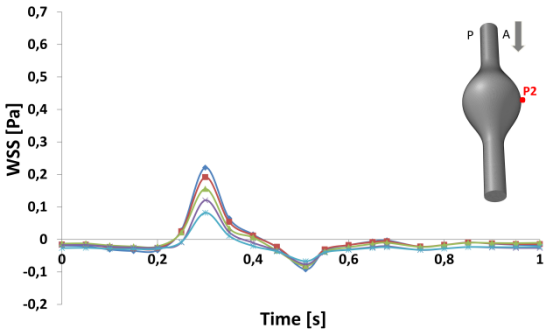

(c) In sac / anterior wall point (P2)

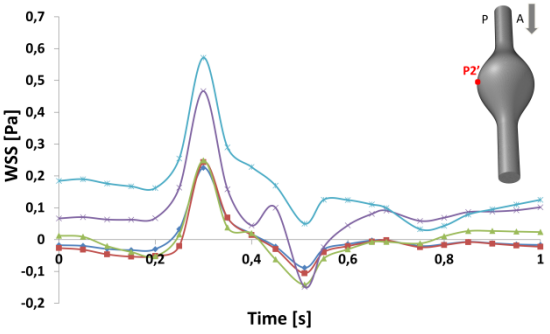

(d) in sac / posterior wall (P2')

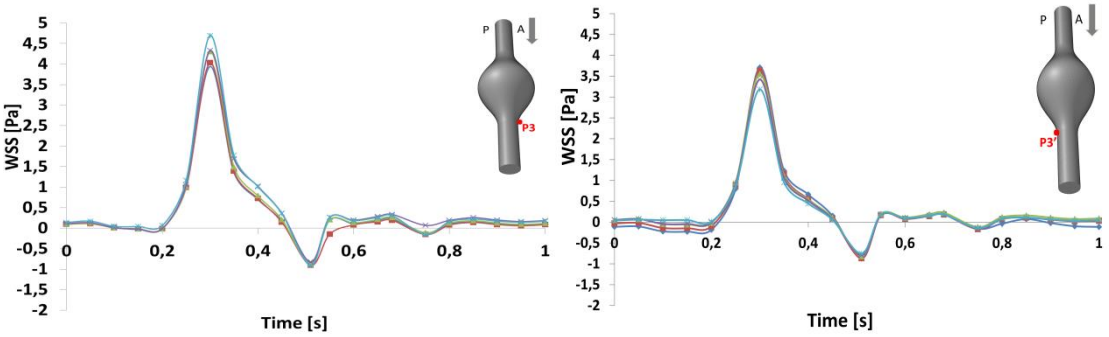

(e) In distal neck / anterior wall (P3) (f) in distal neck / posterior wall (P3')

Figure. 5.9. WSS temporal evolution [Pa] in the models (β=1 β=0.8 β=0.6 β=0.4 β=0.2.).

5.3.4. Analysis of TAWSS and OSI

Figures 5.10 and 5.11 respectively show the InvTAWSS and OSI for the SM and the AM (InvTAWSS the inverse of the TAWSS is displayed for visualization purpose to better detect regions of low TAWSS). The posterior, anterior, left and right views are shown.

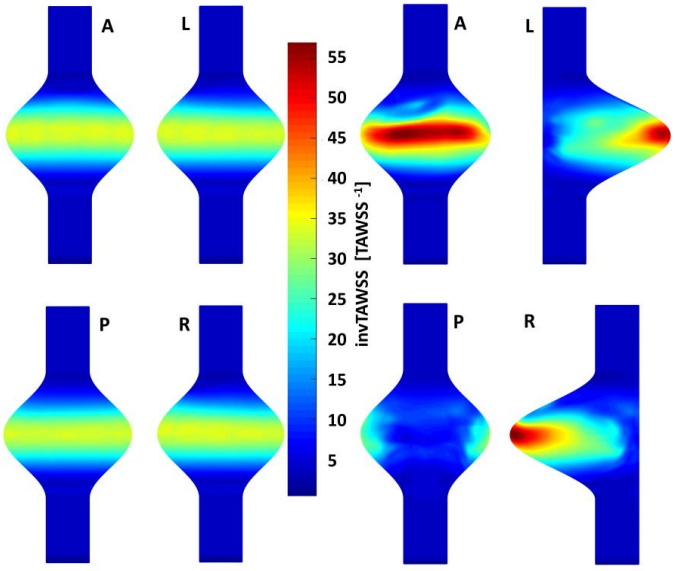

(a) (b)

Figure. 5.10. InvTAWSS contours [Pa-1] in SM (left column) AM (left column) (Views: P: posterior, A: anterior, L: left, R: right).

The OSI contours (see figure 5.11) in the AAA models predict similar behaviour featured by high values in the aneurysm sac. High OSI values are encountered at the wall part near to the recirculation zones. Although these values reach the maximum (OSI≈0.5) in some regions the case of AM in the anterior part of the wall, this region

is subjected to the vortices which were seen earlier (see section Flow Dynamics and vortical structure discussion). An OSI close to 0.5 indicates a region with completely oscillating WSS. In the SM the entire sac is subjected to oscillating WSS (High OSI values), this could be related to the vortex ring detected in this model. The TAWSS in this model is higher than the AM (InvTAWSS reaches highest values in the asymmetric model AM compared to the symmetric model SM as shown in figure 5.10).

Regions where large OSI and small TAWSS (High InvTAWSS) are concomitant, indicating an elevated thrombogenic susceptibility. Da Silva et al., [144] report that ruptures occurred in the region of intraluminal thrombus (ILT) in 80% of AAA.

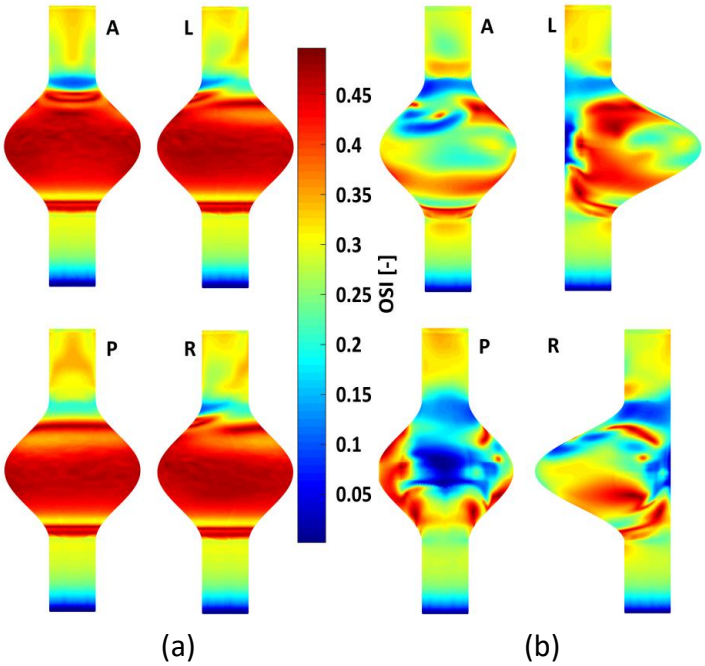

Figure. 5.11. OSI contours [-] in SM (left column) AM (left column) (Views: P: posterior, A: anterior, L: left, R: right).

The notion of minimum values of the WSS has significant effect on the rupture of abdominal aortic aneurysm Boyd *et al.,* [65]. The low values of WSSs are observed in the aneurysm sac where recirculation zones have appeared. The asymmetry of the aneurysm has a clear effect on the flow behaviour, the recirculation zones formation and consequently on WSS and its derivatives distribution. Previous studies were devoted to the understanding of the relationship between vortical structure and ILT accumulation [145] and WSS derivatives showing the importance of CFD as possible tool to help clinicians.

5.4. CONCLUSIONS

In this study, a detailed parametric analysis of flow dynamics using five virtual AAA models was performed numerically; the spatial distribution and the temporal evolution of wall shear stresses were also studied. In addition, hemodynamic parameters such as OSI and TAWSS were analyzed to define the effect of AAA asymmetry on a possible risk of rupture and on the promotion of thrombus formation.

The general characteristics of flow in AAA can be summarized by the formation of a jet that enters the aneurysm, which velocity gradient with respect to the surrounding stationary flow area generates shear layers that evolve creating vortices. Importantly, the development of these vortices is highly influenced by the symmetry of the aneurysm: in the case of an asymmetrical aneurysm, the vortex persists longer than in a symmetrical one. These changes, compared to the flow characteristics in a healthy artery, result in significant changes in the spatial and temporal distribution of wall shear stresses that act on the endothelial cells.

The presented results show that the aneurysm is also subjected to low and oscillating wall shear stresses, with an OSI close to 0.5 in the case of an SM in the entire aneurysm sac. Such conditions favor intraluminal thrombus (ILT) formation and endothelial dysfunction. The results of this detailed CFD study confirm that the asymmetry of the abdominal aortic aneurysm potentially increases its likelihood of rupture and the ILT formation. Although the studied symmetric and asymmetric AAA models have an equal maximum diameter, the asymmetry of AAA has a clear impact on the flow behaviour and WSS derivatives values which could favor their susceptibility to rupture and the formation of ILT.

Despite the limitations of our study, our results provide an interesting data for the understanding of the hemodynamic properties in AAAs, and how CFD study could be useful for clinicians in the prediction of the likelihood of AAA rupture. This study needs to be enlarged to a cohort of patients with ruptured and unruptured AAAs in order to validate its impact on the improvement of risk stratifications due to flow-derived biomechanical bio-markers.

Chapter 6

Intraluminal Thrombus Characteristics in Abdominal Aortic Aneurysm Patients: non-invasive diagnosis using CFD

6.1. INTRODUCTION

Abdominal aortic aneurysm (AAA) is characterized by a deformation and a localized dilatation of the abdominal aorta (usually infrarenal) with 1.5 times the diameter of the healthy aorta [78,79]. AAA is one of the most common cardiovascular diseases, with a prevalence of 1.7-5 % for people over 65 years of age [80], reaching up to 10% for 80 years old male subjects [81]. AAA can undergo sudden rupture, frequently fatal, making AAA rupture one of the most common causes of death in the United States [146]. It accounts for up to 4-5% of all sudden deaths [116] and it is the 14th most common cause of death in the world [117]. The total number of worldwide deaths reached 172,000 in 2019 including both thoracic and abdominal aneurysms [2].

Assessing the risk of rupture is extremely important in reducing AAA mortality. Currently, the most commonly used criterion to select eligible patients for surgery relies on the measurement of the AAA maximum diameter [3-112]. The recent guidelines continue to recommend a threshold diameter of 6.5 cm for AAA as unique criterion to decide whether the resort to surgery is required, for more prudence some clinicians suggested to consider 6.0 cm for women as threshold [80,147]. Thus there is a need to better stratify the risk of AAA rupture by determining additional criteria to help surgeons make a decision regarding the surgical procedure and management of patients with AAA. Several efforts have been devoted for estimating rupture risk. Recently Forneris et al. [71] suggested a new parameter combining time-averaged wall shear stress (TAWSS), intraluminal thrombus (ILT) and wall stress to determine regions of possible rupture.

Despite the controversial role of ILT in AAA rupture, its detection and the prediction of its growth are crucial for clinicians in the treatment and the management of AAA patients. The fact that AAA is often associated with deposition of blood clots and cell debris in the ILT, as well as the breakdown of connective tissue in the wall, it plays an important role in the rupture and the remodeling of the wall. This makes the fluid dynamics in AAA, including the evolution of velocity and wall shear stress (WSS) hemodynamic parameters a very promising index for ILT accumulation predictions and consequently the management of patients with AAAs. Several studies have focused on investigating the relationship between WSS-based parameters and ILT deposition and growth.

Computational fluid dynamics (CFD) are a powerful, non-invasive tool to reproduce flow features in the cardiovascular diseases including AAAs. Using CFD, the behavior of blood flow can be modeled without requiring invasively obtained experimental or field data. Flow features including WSS and its derivatives can be obtained within the CFD model.

To understand the mechanism of ILT accumulation in AAAs, numerical and computational simulations were carried out over the last decade [30,32,37,67-70,148]. Chen et al. [30] found a positive relation between the particle residence time and the platelet activation for ILT. Lozowy et al. [32] studied the effect of jet impingement on ILT deposition in AAA patients, in this work it was concluded that the jet impingement regions may prevent ILT deposition. Chandra et al. [37] observed the absence of ILT in high WSS areas. Zambrano et al. [67] investigated the association of vortical structures, WSS-based hemodynamic parameters and ILT in AAAs. Colciago et al. [68] in their study of patients presenting with thin ILT, showed that simulation-based indicators could support clinicians in the assessment of patients with AAA. Zambrano et al. [69] also conducted a follow-up study on a cohort of patients in order to investigate the relationship between TAWSS, ILT growth and aneurysm expansion. Qui et al. [70] assessed, via computational fluid dynamics simulation, the near-wall hemodynamic parameters in ruptured AAA patients.

None of the above literature has proposed a comprehensive analysis to understand the near wall flow nature in AAA and its relation with ILT deposition by considering hemodynamics indicators including transversal WSS (TransWSS), relative residence time (RRT) and the endothelial cell activation potential (ECAP) in addition to TAWSS and OSI. Further, none of the numerical studies so far have investigated the difference between thin and thick ILT areas for AAA patients and their relationship with the cited WSS-based parameters for the purpose of understanding the ILT deposition process and the prediction of ILT growth, . This part of the study has two-fold purpose: (i) investigate the co-localization and the relationship between the velocity flow spatiotemporal distribution and five WSS-based hemodynamic parameters obtained noninvasively by CFD simulations (ii) determine ILT deposition from CT scan images in order to differentiation between thick and thin areas of ILT deposition in terms of hemodynamic characteristics and to develop a criterion to help clinicians in the

prediction ILT deposition for assessment and management of AAA patients . Finally the relationship between flow the nature near the wall and ILT deposition areas is investigated by exploring TransWSS in addition to TAWSS and OSI.

6.2. MATERIALS AND METHODS

6.2.1. Workflow

The patient-specific model geometries of three male patients with a mean age of 68 years diagnosed with AAA were reconstructed from Computed Tomography (CT) scans acquired between the 3rd and 17th of February, 2021 under ethical approval statement (see Appendix C). These patients are labeled as Patient 1; Patient 2; and Patient 3 (Table 6.1). These steps are schematized in a detailed flowchart (see chapter 4 figure 4.3).

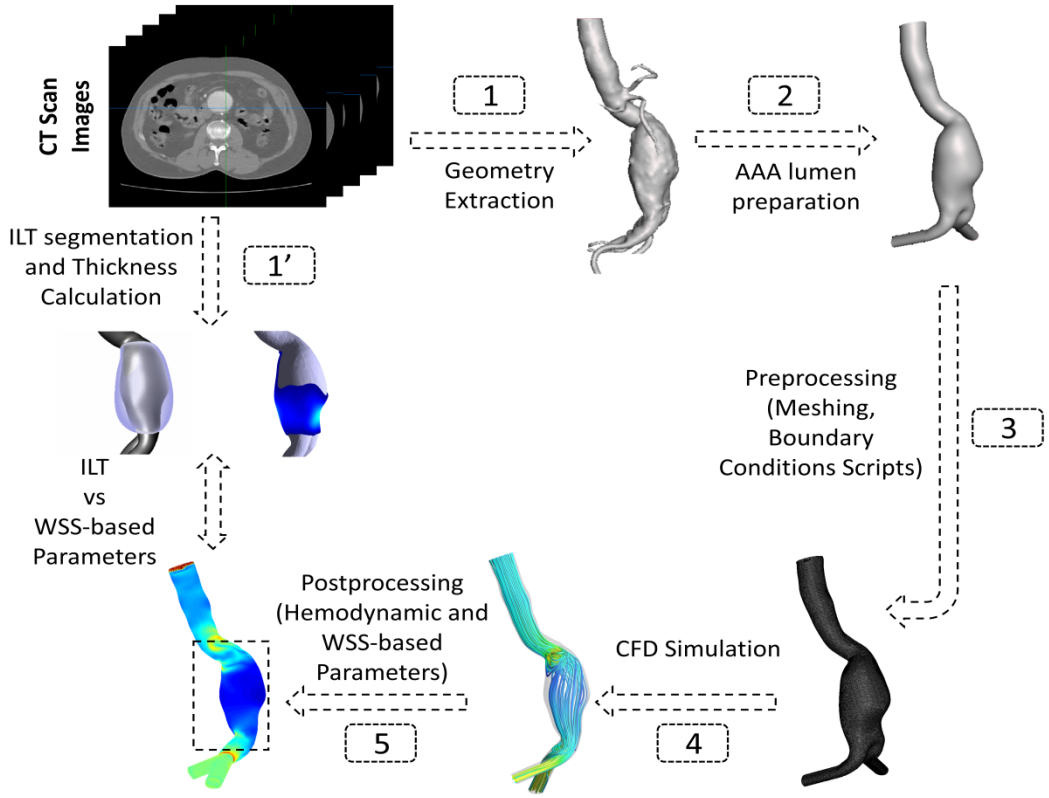

Figure. 6.1: Schematic representation of the adopted workflow showing the followed steps from CT images segmentation to post-processing of CFD based data.

Figure 6.1 shows a schematic diagram of the process adopted in this part of the study. The geometries were trimmed and prepared to be used in the CFD simulations and

finally data post processing was performed to extract the hemodynamic parameters and wall shear stress derivatives from CFD results.

6.2.2. Data acquisition & patient specific geometries reconstruction

CT scans of the patients were provided by a medical imaging center, with a slice thickness of 2 mm for Patients 1 and 2, and of 1 mm for Patient 3. To extract the arteries' lumen, SimVascular open-source software was used [148].

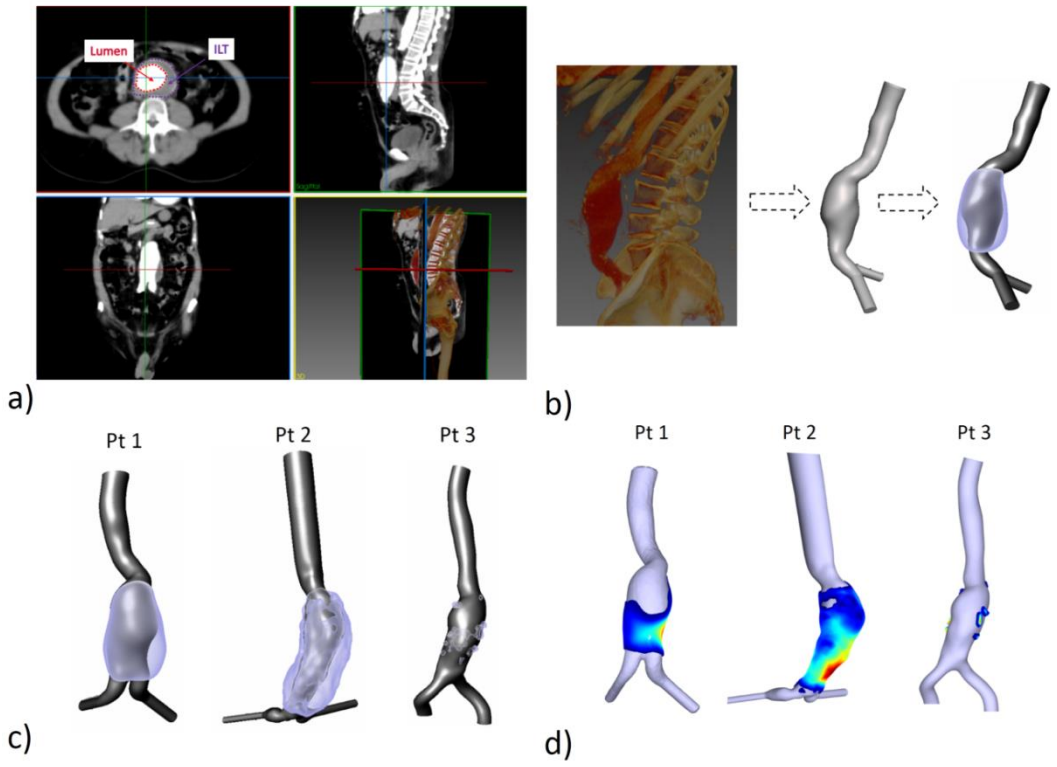

Figure. 6.2: a) Example of CT scan slices in axial, sagittal, coronal and 3D rendered views; lumen and ILT regions are shown in axial views and b) Rendered left sagittal image and segmented artery with ILT of AAA for Patient 1. c) Extracted computational domains of three AAA patient-specific lumens used to perform numerical simulations (grey) and ILT regions (purple) d) calculated ILT thickness patched to the lumen surface where blue corresponds to low values (thin) and red to high values (thick).

The arterial wall was smoothed to reduce roughness by using the shape-preserving smoothing filter and then clipped at the two iliac arteries to create the outlets' surfaces using Autodesk Meshmixer software (www.meshmixer.com). The descending aortas were clipped distally including entrance lengths which were calculated using an expression by Wood et al 1999 [149]. The two outlets were extruded by five times the

iliac arteries' diameters. Similarly to the aortic lumen, the segmentation of the ILT was performed using SimVascular (Figure 6.2(c)).

In order to estimate the ILT thickness, the coordinates of the outer ILT surface and the surface of aortic lumen of the three aneurysm models' were exported to a purposely developed in-house MATLAB script (Figure 6.2(d)) to calculate the distance between the two surfaces. *In vivo* studies of AAA have estimated the wall thickness to vary between 1 mm and 4.26 mm [150, 151]. In our work it is assumed to be constant with 2mm thickness. To obtain the final ILT thickness, a mask of 2 mm was applied to subtract the wall thickness from the initially estimated ILT thickness. For visualization purpose and to compare against WSS-based parameters, the final ILT thickness values were patched to the aortic lumen surface (Figure 6.2d). The final obtained geometries are displayed in Figures 6.2c and 2d and more details about the three AAAs are provided in Table 6.1.

Table 6.1: Threes AAA patients geometrical features and details.

Patient	Age (yrs)	Gender	Maximum lumen AAA diameter (mm)	Inlet AAA diameter (mm)	Right Iliac diameter (mm)	Left Iliac diameter (mm)	Length of AAA (mm)	Max ILT thickness (mm)	ILT thickness & distribution
Patient 1	70	male	56.7	25.2	15.9	17.2	118.1	19.9	-thick-thin -partially in AAA sac
Patient 2	76	male	45.2	23.6	16.5	14.9	146.5	18.5	-thick-thin -entire in AAA sac
Patient 3	60	male	32.4	19.6	13.4	12.9	86.3	1.6	-thin -small part of AAA sac

6.2.3. Patient specific CFD simulation

The patients' geometries, previously segmented in SimVascular from the CT images, were imported and discretized into a volumetric mesh of tetrahedral elements using ANSYS Icem CFD (ANSYS, Inc., Canonsburg, USA). Mesh sensitivity studies were performed with the aim of defining the optimum computational domain for each AAA model (see mesh sensitivity analysis section). The final meshes' details are described in Table 6.2. Near the wall, an exponential growth ratio was adopted with a minimum element size of 0.2 mm and a total thickness of approximately 2.6 mm. Three cardiac cycles were simulated to minimize the influence of initial conditions, and the last cycle

was considered in our results. The aortic wall was assumed to be rigid with no-slip condition [152-154]. A small change in wall deformation was found in elderly AAA patients [155]. The adopted numerical model was validated and compared with experimental results (See validation section).

Table 6.2: Mesh details used in the numerical calculation of the AAA patients.

Patient	Number of cells (Millions)	Number of nodes (Millions)
Patient 1	3.789	0.948
Patient 2	3.877	0.985
Patient 3	3.885	1.024

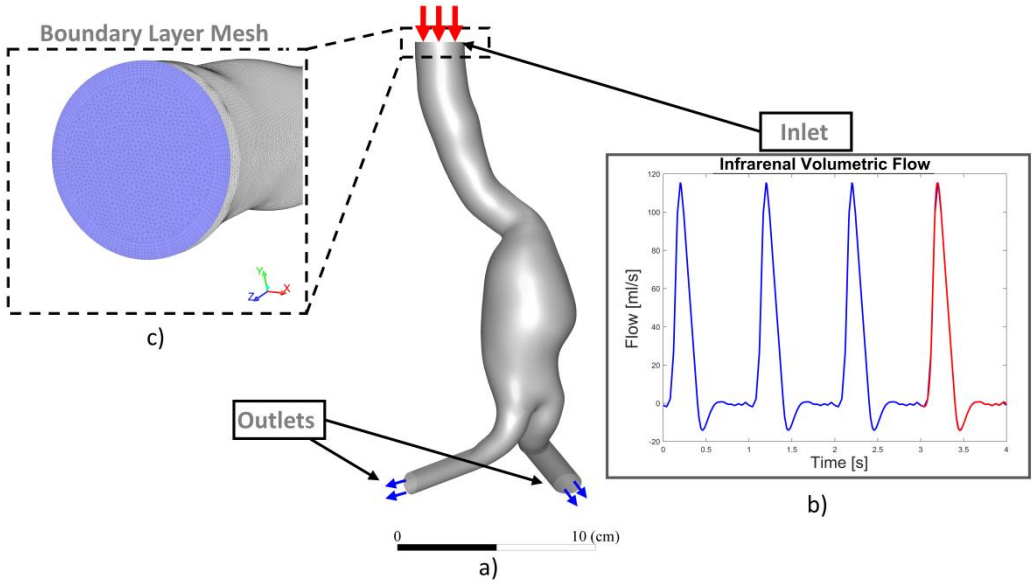

Figure. 6.3: Overall dimensions 3D model (Patient 1 is illustrated) of abdominal aortic aneurysm (AAA) (a) being subjected to inflow pulsatile velocity waveform (b) as inlet boundary condition used in the numerical model (the waveform displayed corresponds to flow rate instead of velocity). Boundary layer mesh at the inlet face is displayed (c).

Using a phase-contrast MRI (PC-MRI) data the flow waveforms at infrarenal artery were extracted by Les et al. and interpolated from a cohort of 36 AAA patients and then an averaged volumetric flow was deduced [156]. The PC-MRI based volumetric flow is converted to a corresponding velocity inlet waveform for each patient (an example is shown for Patient 1 in Figure 6.3). A zero reference pressure was imposed at the outlet boundaries [32,157-159]. The temporal variations of the physiological

velocity inlet condition were reproduced by Fourier series and implemented through a "user_defined_function" (UDF) script.

6.2.4. Mesh sensitivity analysis

To define the optimum computational domain for each AAA model, a mesh sensitivity study was performed by running unsteady flow simulations in ANSYS Fluent using three different meshes (coarse, medium, and fine) for each patient, as shown in Table 6.3. ANSYS Icem CFD (ANSYS, Inc., Canonsburg, US) was used for the mesh generation. The numerical model and boundary conditions detailed in the methodology section were used. The results at systolic peak were compared between the three meshes. A similar velocity pattern and Wall Shear Stress (WSS) distribution were captured by all three meshes for the three patients, as shown in Figure 6.4. The WSS contours for Patient 1 (one patient is shown here as illustration) presented comparable distribution and the highest computed WSS occurred at similar locations, but different maximum values of (WSS_max) were found with the different grids (see Table 6.3).

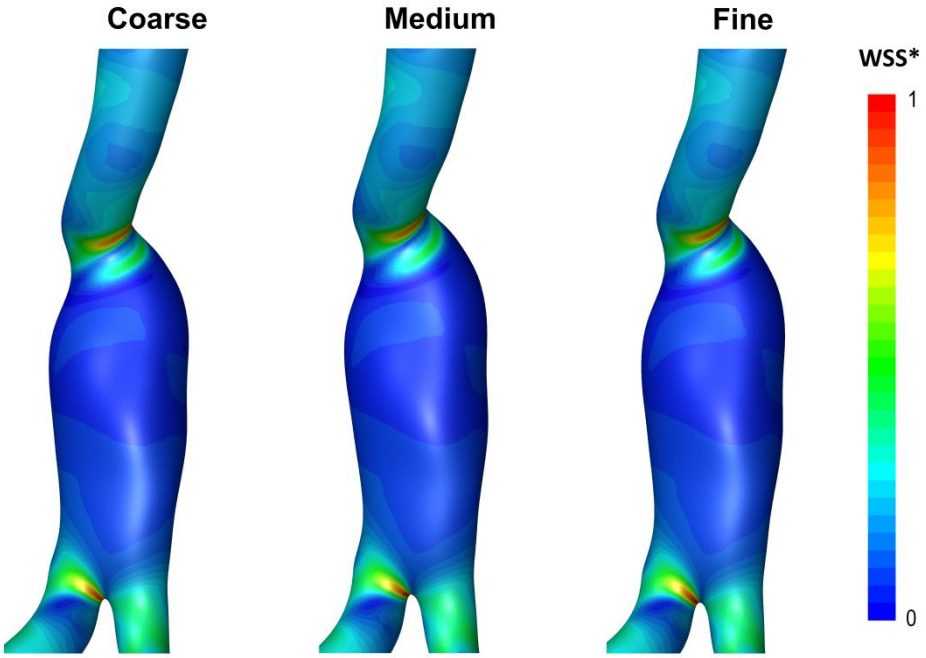

Figure. 6.4: Example of qualitative results showing Wall shear stress contours in the threes meshes for Patient 1(posterior view is displayed to show the peak values). WSS* is normalized with respect to WSS computed on the fine grid.

Table 6.3: Grid Convergence Index (GCI) and Grid parameters for the 3 AAA patients with corresponding WSS_max values.

	Grid	Number of cells (Millions)	WSS_max (Pa)	GCI (%)
Patient 1	g1 Fine	6.379	4.856	GCI1-2=0.102
	g2 Medium	3.799	4.872	GCI2-3=0.327
	g3 Coarse	2.306	4.822	
Patient 2	g1 Fine	6.351	25.559	GCI1-2=1.448
	g2 Medium	3.877	25.132	GCI2-3=0.651
	g3 Coarse	2.364	25.320	
Patient 3	g1 Fine	6.763	18.167	GCI1-2=0.035
	g2 Medium	3.885	17.630	GCI2-3=0.209
	g3 Coarse	2.236	17.891	

Additionally a comparison of velocity profile in the three grids with at least two lines inside the aneurysm for each patient was performed. A similar profile with error <1% was found for the three patients. Figure 6.5 shows an example of the velocity profile across one line in the center the aneurysm sac of Patient 1.

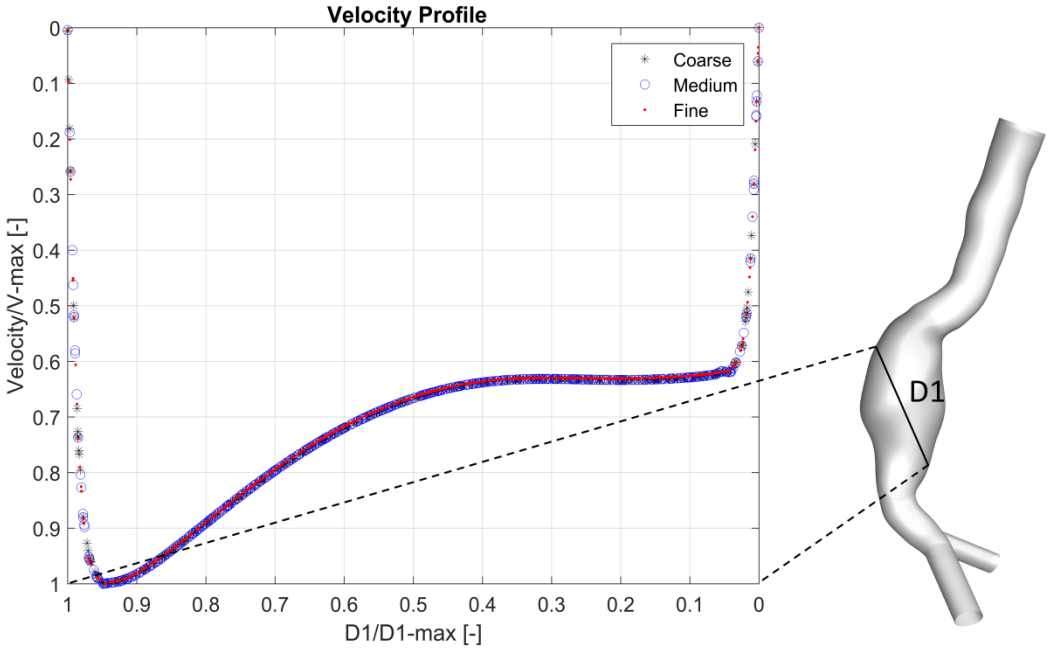

Figure 6.5: Velocity profile across a line in the center of the aneurysm in Patient1 at systolic peak. Curves are CFD results for threes grids (Coarse, Medium and Fine). Velocity values are normalized with respect to V-max in this line.

Furthermore the mesh sensitivity analysis was endorsed by the calculation of the Grid Convergence Index GCI (equations 6.1-6.2) and the maximum WSS (WSS_max) was used as a parameter of interest. The GCI measures the percentage of difference

between the computed parameter (WSS_max) for two consecutive grids and estimates how far it is from the asymptotic value. This index is considered as the most reliable technique for the quantification of numerical uncertainty [161]. The mesh sensitivity analysis revealed that the solution became relatively independent to further mesh grid refinement. The medium meshes were used for each patient corresponding to medium-to-fine GCI of approximately 0.327%, 0.651% and 0.209% for Patient 1, Patient 2 and Patient 3 respectively (see Table 6.3), which is in agreement with recent studies where the grid is adopted if GCI was inferior to 5% [162].

$$\mathrm{GCI}_{g1,g2} = \mathrm{F_s} \,.\, \left|\mathrm{E}_{g1,g2}\right| \tag{6.1}$$

$$\mathrm{GCI}_{g2,g3} = \mathrm{F_s} \,.\, \left|\mathrm{E}_{g2,g3}\right| \tag{6.2}$$

$$\mathrm{E}_{g1,g2} = \frac{\log\left(\frac{f_{g2}-f_{g1}}{f_{g1}}\right)}{r^{p}-1} \tag{6.3}$$

$$\mathrm{E}_{g2,g3} = \frac{\log\left(\frac{f_{g3}-f_{g2}}{f_{g2}}\right)}{r^{p}-1} \tag{6.4}$$

$$r \approx \left(\frac{N_{g1}}{N_{g2}}\right)^{1/3} \approx \left(\frac{N_{g2}}{N_{g3}}\right)^{1/3} \tag{6.5}$$

$$p = \frac{\log\left(\frac{f_{g3}-f_{g2}}{f_{g2}-f_{g1}}\right)}{\log r} \tag{6.6}$$

F_s is the factor of safety which is equal to 1.25 [160], fgi corresponds to the variable of interest (in our case WSS_max) and Ngi is the number of cells in the grid.

6.2.5. Validation

To validate the numerical model we performed a comparison of the axial velocity profile at the center of the aneurysm with the experimental and numerical data of Budwig et al. [139] for steady flow through axisymmetric AAA model. The simulations are carried out at Re = 2000 and Re=400, aneurysm-to-artery diameter ratio D/d=2.1, and an aspect ratio of the aneurysm L/d=4 (L is the length of the aneurysm). The flow feature is characterized by a jet formation surrounded by recirculating vortex and an agreement was found between the present results and the description given by Budwig et al. [139]. The velocity profiles across the aneurysm are in good agreement with the experimental and numerical results of Budwig et al. [139] (see figure 6.6a and 6.6b respectively), but the shape of the aneurysm was not detailed in this reference. The possible difference of the shape of the aneurysm may be the cause of the slight

difference in the velocity profile compared to the provided experimental and numerical results.

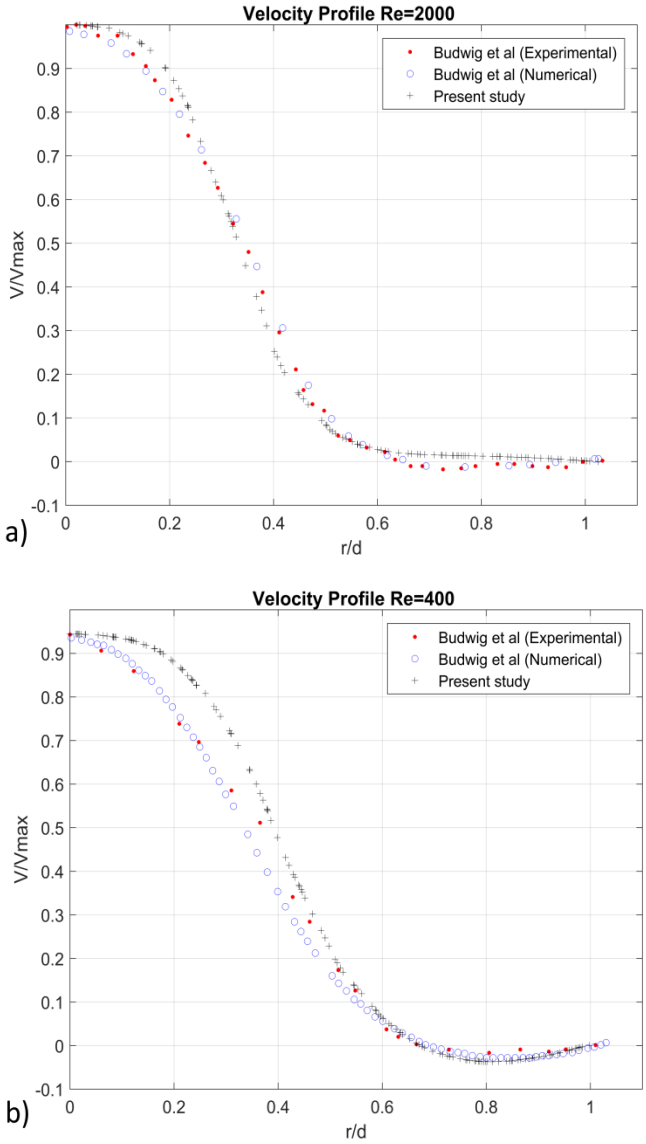

Figure. 6.6. Comparison of steady profile across the center of the AAA (D/d = 2.1, L/d = 8) with the experimental and numerical results derived and reproduced from Budwig et al [139] a) Re = 2000, b) Re = 400.

6.2.6. Governing Equations

This work modeled the blood as non-Newtonian fluid. The Carreau-Yasuda (C-Y) model was used to capture blood's shear-rate behavior [106]. The C-Y model was implemented using the UDF script for blood viscosity and was expressed by the equation 3.21 seen in chapter 3.

The flow in the abdominal aorta is hence described by the incompressible Navier-Stokes and continuity equations for non-newtonian fluid (see equations 3.15-3.21 in chapter 3 for more details) under the assumption of laminar incompressible flow (density $\rho = 1050\ \mathrm{kg}/m^3$).

In this study the finite volume method (FVM) was adopted to solve the governing equations and to predict the time-dependent flow through three-dimensional AAA geometries by using Ansys Fluent (ANSYS, Inc., Canonsburg, US) with the implicit solver. A second-order upwind scheme was used for spatial discretization and the SIMPLE algorithm (Semi-Implicit Method for Pressure Linked Equations) for pressure-velocity coupling. Each pulse cycle was divided into 1200 time-steps of 83.333×10^{-2} ms. The convergence criteria for the solutions were considered when the residuals for the continuity and the velocity achieved 1×10^{-5}.

6.3. RESULTS

6.3.1. Velocity Field and ILT deposition

At the peak systole (t/T=0.201), the flow is attached to the wall in the three cases. During the deceleration phase, a recirculation zone is captured in the posterior wall near the neck of the AAAs (proximal region of the posterior wall) for Patient 1 and Patient 3 starting from t/T=0.25, and at t/T =0.33 for Patient 2. The recirculating zone develops taking the aneurysm sac and persists throughout the diastole phase.

In addition to the mid-sagittal CT image, Figure 6.7 shows also the time-averaged velocity contours in the corresponding section for all the three Patients 1, 2 and 3 respectively in Figures 6.7-a, 6.7-b and 6.7-c. The ILT deposition zones are delimited by red dashed lines in CT images and as a 3D representation with the AAA computational domain. ILT covers the entire AAA sac in Patients 1 and 2 except the anterior proximal area for Patient 1, whereas in Patient 3, smaller separated areas of ILT are detected.

At the inlet of the aneurysms (the distal neck), a jet is formed and penetrates into the aneurysmal sac. The velocity gradient between the jet flow and the surrounding parts produces shear layers, generating recirculating zones. Time-averaged velocity magnitude contours in the mid-sagittal section shows apparent low velocity magnitude regions along the posterior wall in the first two patients, 1 and 2, (indicated

by the yellow arrows). The formed jet is close to the proximal anterior wall for the three patients (see figure 6.7).

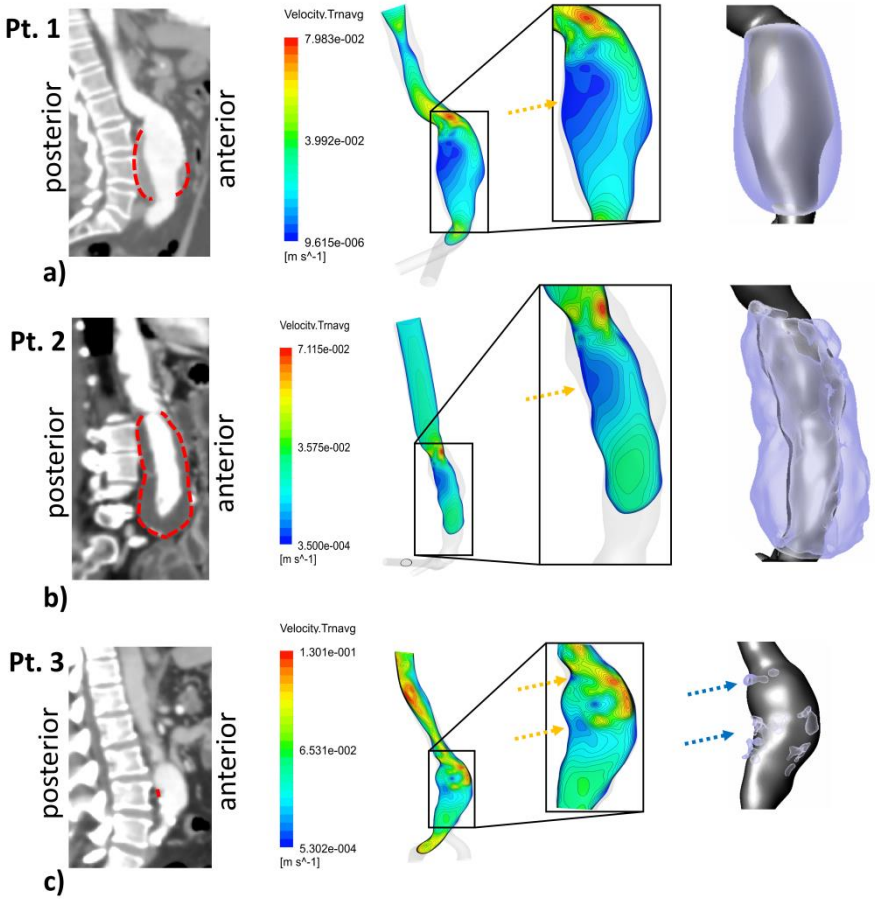

Figure. 6.7: Right sagittal CT images with dashed red lines showing outer ILT walls (left column). Time-averaged velocity contours at right view of mid-sagittal section and magnified in the AAA sac region (middle column); yellow arrows show recirculating flow zones. Extracted computational domain (grey) and ILT deposition (purple) of AAAs patients are shown in the rightmost column; blue arrows indicate ILT deposition areas for Patient 3.

6.3.2. WSS derivatives and ILT

Figure 6.8 shows the posterior view of TAWSS, invTAWSS (the inverse of the TAWSS) and normalized TransWSS contours of the Patient1 (TransWSS is normalized with respect to the maximum values of each patient NtransWSS = TransWSS / max (TransWSS)) respectively in figures 6.8a, b and c. Similarly Contours of OSI, RRT and ECAP are shown in Figure 6.8d, e, and f respectively. These parameters are calculated and plot using our purposely developed ad-hoc MATLAB script (The Mathworks Inc.).

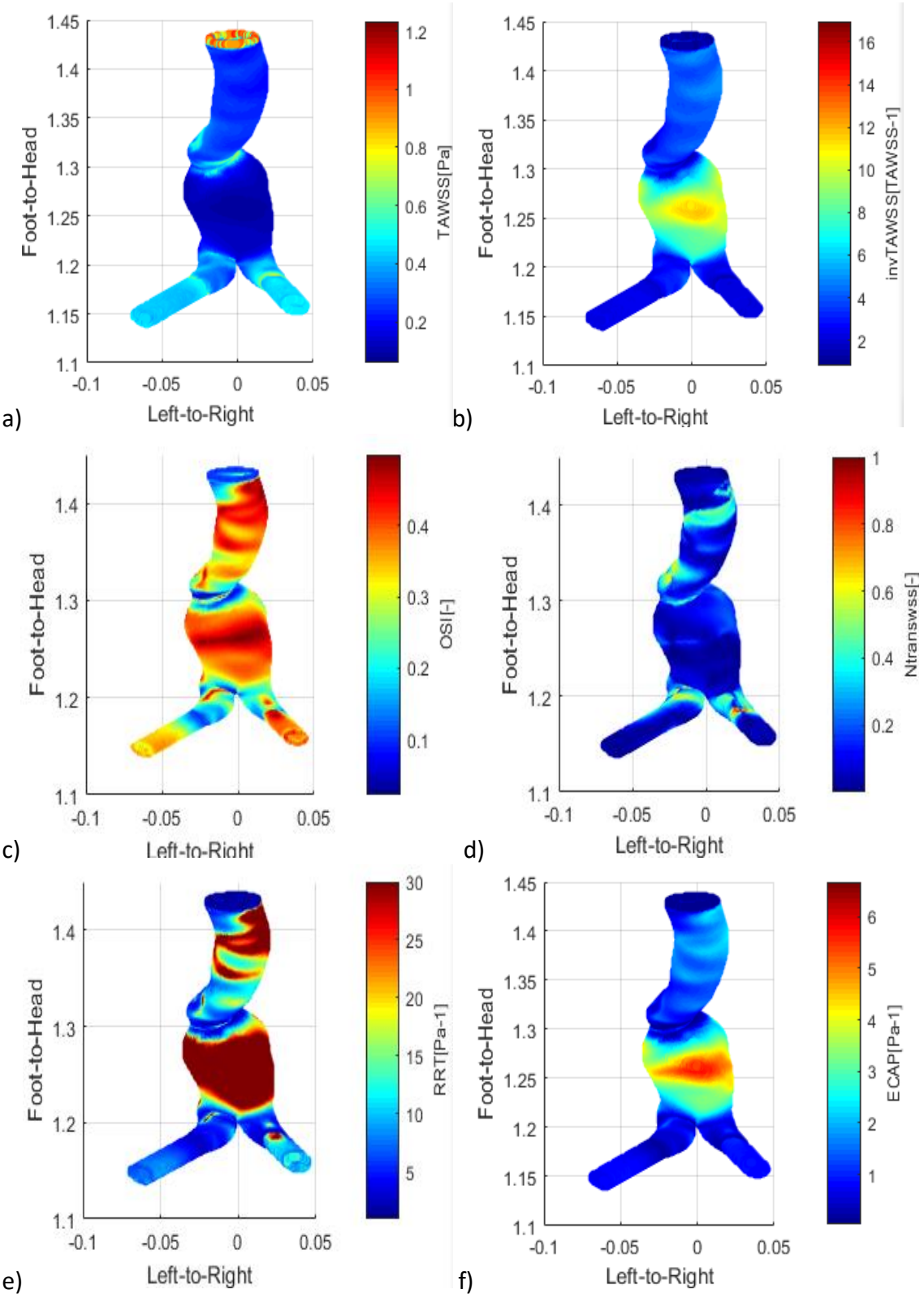

Figure. 6.8: Visualization of WSS derivatives calculated by the ad-hoc MATLAB script in the case of patient1, posterior view is shown (axes: Left-right and Foot-Head). a) TAWSS [Pa] , b) InvTAWSS [Pa^{-1}], c) NTransWSS [-], d) OSI [-], e) RRT [Pa^{-1}] and f) ECAP [Pa^{-1}].

Figure 6.9 and 6.10 shows the four views (Posterior, anterior, left, and right views) of WSS derivative for the three patients. Contours of TAWSS, invTAWSS and NTransWSS

for the three Patients, are shown in Figure 6.9. Contours of OSI, RRT and ECAP for the three Patients, are shown in Figure 6.10.

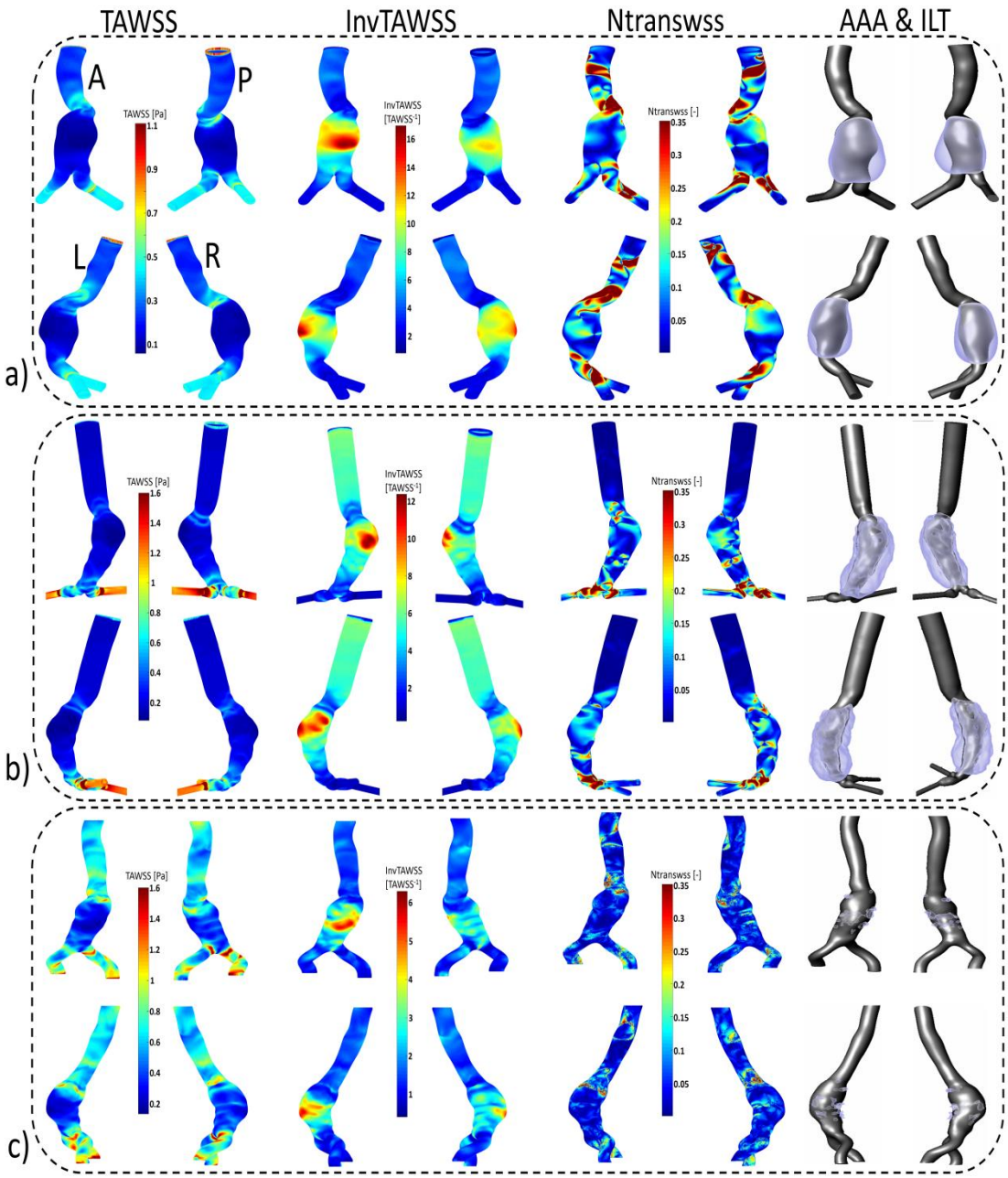

Figure. 6.9: Visualization of TAWSS, InvTAWSS and normalized TransWSS (NTransWSS) distributions (respectively from left to right columns) in AAA patients using CFD simulations. Extracted computational domain (grey) and ILT deposition (purple) of AAAs patients derived from CT scan images are shown in the rightmost column as 3D representation.

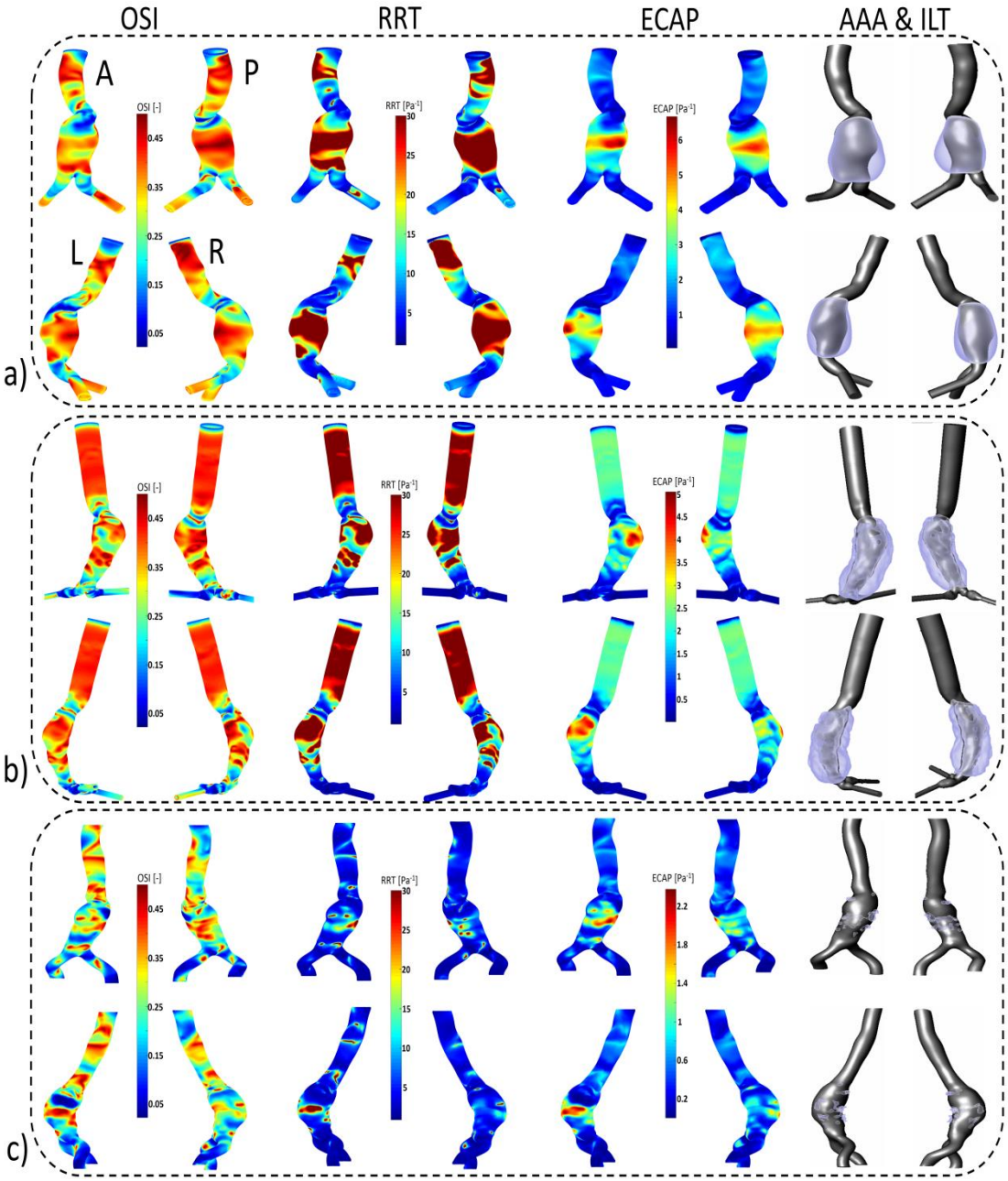

Figure. 6.10 : Visualization of OSI, RRT and ECAP (respectively from left to right columns) in AAA patients using CFD simulations a) Patient 1 b) Patient 2 c) Patient 3. Extracted computational domain (grey) and ILT deposition (purple) of AAAs patients derived from CT scan images are shown in the rightmost column as 3D representation.

TAWSS and InvTAWSS are investigated in order to show the high and low regions of WSS average over one cardiac cycle. For the three patients, the AAA sac is characterized by low TAWSS values (high InvTAWSS) compared to the healthy part of the aorta. As it can be observed the minimum values of TAWSS (max values of InvTAWSS) are found in the dome of the aneurysm reaching values of maximum InvTAWSS superior to 17, 12 and 6 Pa^{-1} for Patients 1, 2 and 3 respectively. From these

results it can be observed that low TAWSS (high InvTAWSS) are linked with ILT deposition regions in terms of qualitative comparison. Patient 3 presents a higher range of TAWSS values (lower range of InvTAWSS) in the AAA sac compared to Patients 1 and 2. This patient is characterized by small and dispersed ILT deposition areas in the aneurysm sac.

The OSI provides the oscillatory aspect of the flow: high values of OSI indicate that the flow is purely oscillating and low values indicate that the flow is purely forward. TransWSS is introduced by Peiffer et al. [113] to complete the OSI and TAWSS and to distinguish between uniaxial and multidirectional flows. TransWSS was examined in this study in order to understand the nature of the flow near the arterial wall in different areas of the AAA.

For Patient 2, high values of TransWSS are observed in the two iliac arteries and in some dispersed areas of the AAA sac. Whereas an inverse relationship was found between TransWSS and OSI in the entrance of AAA sac for Patient 1, where high values of TransWSS coincide with low OSI in this area, and the wall is devoid of ILT deposition. Conversely, the wall is devoid of ILT in some areas for Patient 2 with low values of both OSI and TransWSS.

In the aneurysm sac, the ILT deposition is correlated with high oscillating flow corresponding to high OSI values, high relative residence time (RRT) of blood particles near the wall and low TAWSS (high InvTAWSS) values for Patients 1 and 2. Patient 3 presents different behavior, exhibiting ILT deposition in dispersed areas through the aneurysmal sac, making it interesting in the understanding of which WSS indicators and hemodynamic parameters are linked to ILT deposition. In this Patient, ILT deposition co-localizes with high OSI, ECAP and RRT; and inversely co-localizes with low TAWSS. For all three patients, RRT and ECAP present an almost similar topological distribution as OSI in the AAA sac, which is the area of interest in this study.

6.3.3. Flow near the wall and ILT

Tables 6.4, 6.5 and 6.6 succinctly summarize the nature of the flow near to the wall for all compartments in the three patients, Patient 1, 2 and 3 respectively. From these three tables, it can be observed that regions of low TAWSS and high OSI are subjected to ILT deposition (as per the rightmost column in the threes aforementioned tabs) for

all the aneurysms independently to NtransWSS. In those regions, the EC are subjected to oscillating non disturbed flow (low TransWSS) or oscillating disturbed flow (high TransWSS) (see TAWSS, OSI and NtransWSS in Figure 6.11).

Table 6.4: ILT deposition regarding flow near the wall to which Endothelial Cells (ECs) are subjected to in region of interest (AAA sac) for Patient 1 (P1).

	AAA areas	**WSS parameters**			**Flow near the wall to which Endothelial cells EC are subjected to ***	**ILT deposition**
		TAWSS	OSI	TransWSS		
P1	Entrance of AAA	-High	-Low	-High	-Unidirectional disturbed flow 	-No ILT 
	AAA Sac	-Low	-Low	-High and (low in some regions)	-Unidirectional disturbed flow (non-disturbed flow) 	-No ILT 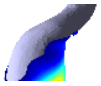
			-High	-Low	-Oscillating non disturbed flow 	-ILT 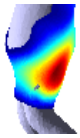
				-Proportionally High in some regions	- Oscillating disturbed flow 	
	Downstream AAA SAC	-High	-Low	-High	-Unidirectional disturbed flow 	-No ILT 

* Graphical representations of flow near the wall to which Endothelial cells EC are subjected to, (Adapted from [113]).

Table 6.5: ILT deposition regarding flow near the wall to which Endothelial Cells (ECs) are subjected to in region of interest (AAA sac) for Patient 2 (P2).

	AAA areas	**WSS parameters**			**Flow near the wall to which Endothelial cells EC are subjected to ***	**ILT deposition**
		TAWSS	OSI	TransWSS		
P2	Entrance of AAA	-High	-Low	-Low	-Unidirectional non disturbed flow 	-No ILT 
				-Proportionally High in some regions	-Unidirectional disturbed flow 	
	AAA Sac	-Low	-High	-Low	-Oscillating non disturbed flow 	-ILT 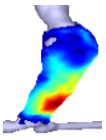
				-Proportionally High in some regions	- Oscillating disturbed flow 	

	Downstream AAA SAC	-High	-Low	-High	-Unidirectional disturbed flow 	-No ILT 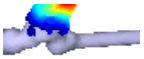

* Graphical representations of flow near the wall to which Endothelial cells EC are subjected to, (Adapted from [113]).

Table 6.6: ILT deposition regarding flow near the wall to which Endothelial Cells (ECs) are subjected to in region of interest (AAA sac) for Patient 3 (P3).

	AAA areas	**WSS parameters**			**Flow near the wall to which Endothelial cells EC are subjected to ***	**ILT deposition**
		TAWSS	OSI	TransWSS		
P3	Entrance of AAA	-High	-Anterior part low	-High	- Unidirectional disturbed flow 	-No ILT (anterior)  A
		-Low	-Posterior part high		- Oscillating disturbed flow 	-ILT (posterior) P 
	AAA Sac	-Low	-High Dmax zone (belt from dome to posterior)	-Low	- Oscillating non disturbed flow 	-ILT 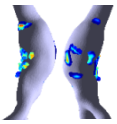
		-High	-Low in the remaining regions		- Unidirectional non disturbed flow 	-No ILT
	Downstream AAA Sac	-High	-Low	-Low	-Unidirectional disturbed flow 	-No ILT 

* Graphical representations of flow near the wall to which Endothelial cells EC are subjected to, (Adapted from [113]).

6.3.4. ILT-thickness areas as possible indicator

To further elucidate the ILT deposition-WSS derivatives' relationship, in Figure 6.11 we show two views for each aneurysm, enabling a visual comparison between WSS derivatives thresholds versus ILT thickness. In the literature, different threshold values of WSS derivatives are defined as a key threshold to distinguish between low and high values when predicting thrombus formation, therefore we decided to use the most common ones from different investigations. Hemodynamic conditions favorable for ILT deposition in aorta where defined: low TAWSS and particularly <0.4 Pa by [29,64,66,160]. OSI values >0.2 to 0.3 [66,113,145]; ECAP >1.4 Pa^{-1} [29] and values >10 Pa^{-1} for RRT [66], these values are adopted as threshold. ILT thickness was calculated

by MATLAB script (detailed previously in section 6.2). The thickness values are patched to the lumen surface for visualization purposes, allowing easy comparison against WSS derivatives in Figure 6.11.

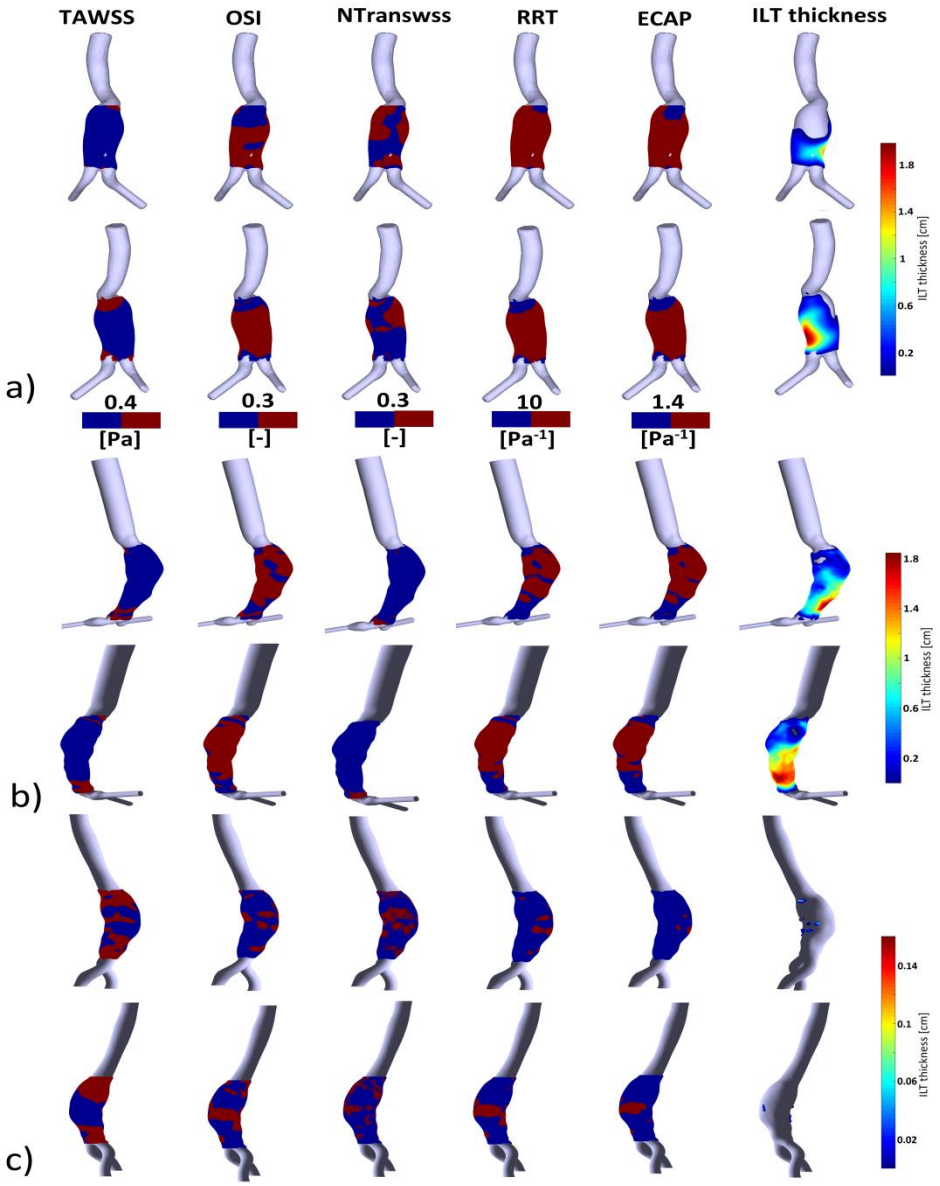

Figure. 6.11: Visualization of TAWSS,OSI, NTransWSS, RRT and ECAP (respectively from left to right columns) in three AAA patients using CFD simulations in the AAA zone with threshold values indicated in the corresponding color-maps (Blue for values below threshold and Red for values above) . In the rightmost column ILT thickness in [cm] is shown for: (a) Patient 1; (b) Patient 2; and (c) Patient. For visualization purpose, two views are displayed for each patient.

WSS derivatives at the inlet aorta and the iliac arteries are masked, showing only the aneurysmatic region which is the region of interest. As observed, ILT deposition is

related to TAWSS and OSI and consequently to RRT and ECAP. From Figure 6.11a and 8b, it can be observed that for Patients 1 and 2, which are characterized either by thrombus covering the entire AAA sac (for Patient 2, as per Figure 6.11b) or partially covered (for Patient 1, as per Figure 6.11a), the TAWSS is low and OSI is high in almost the entire aneurysm sac (see Figure 6.12). Whereas for Patient 3 (Figure 6.11c), which presents a small part of the aneurysm sac covered by ILT near to its lumen maximum diameter, this area corresponds to low TAWSS and high OSI values; in contrast, the remaining AAA regions are subjected to high TAWSS and low OSI values.

As it could be seen in the statistical boxplots (see Figure 6.12) mean TAWSS and OSI values for Patients 1 and 2 are respectively 0.14 Pa and 0.32 for Patient 1 and 0.241 Pa and 0.324 for Patient 2. Patient 3 presents a mean TAWSS equal to 0.48 and mean OSI equal to 0.23.

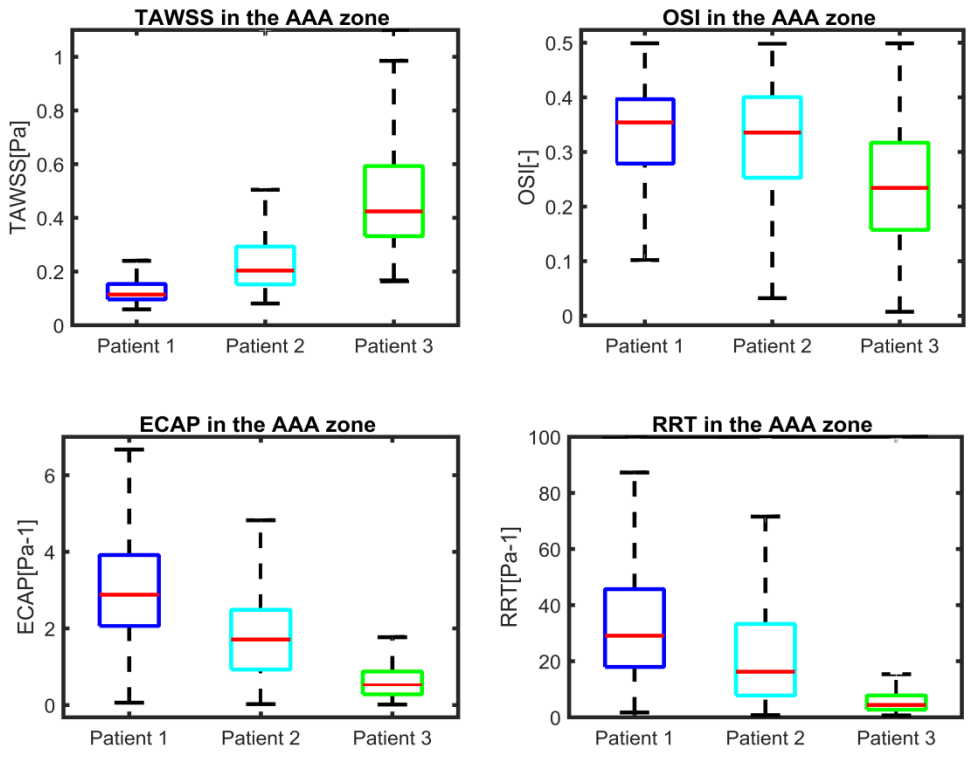

Figure. 6.12: Boxplots of WSS-based parameters (TAWSS, OSI, ECAP and RRT) in the entire AAA region for Patients 1, 2 and 3. Whiskers refer to the 10th and the 90th percentiles respectively; each box ranges between the first and the third quartiles with red line designating the median value of the WSS derivatives.

One difference between Patient 1 and Patient 2 should be noted. For patient 2, the thickest ILT area is located in the distal part of the aneurysm sac, corresponding to low

values of OSI, RRT and ECAP (the blue area in Figure 6.11b) and also high values of TAWSS (red area), while in Patient 1, the ILT is also thickest in the distal part but correlates with opposite to patient 2's hemodynamic conditions in corresponding zone. Those hemodynamic parameters correspond to the proximal anterior part of the aneurysm sac (entrance) which is devoid of ILT in Patient 1.

Motivated by the last observation of difference between Patient 1 and Patient 2 (Patient 3 was not included in this part of the study since it does not show a thinnest and thickest ILT areas), we investigated whether we can use the hemodynamic characteristics in the thinnest and thickest ILT in AAAs as possible indicators of ILT growth. Supposing that the thresholds and magnitude of WSS descriptors found in the literature and used in this study characterized by, on one hand, low values of TAWSS, and on the other hand high values of OSI, ECAP and RRT are the most favorable hemodynamic conditions to determine areas of AAA where ILT will continue to grow.

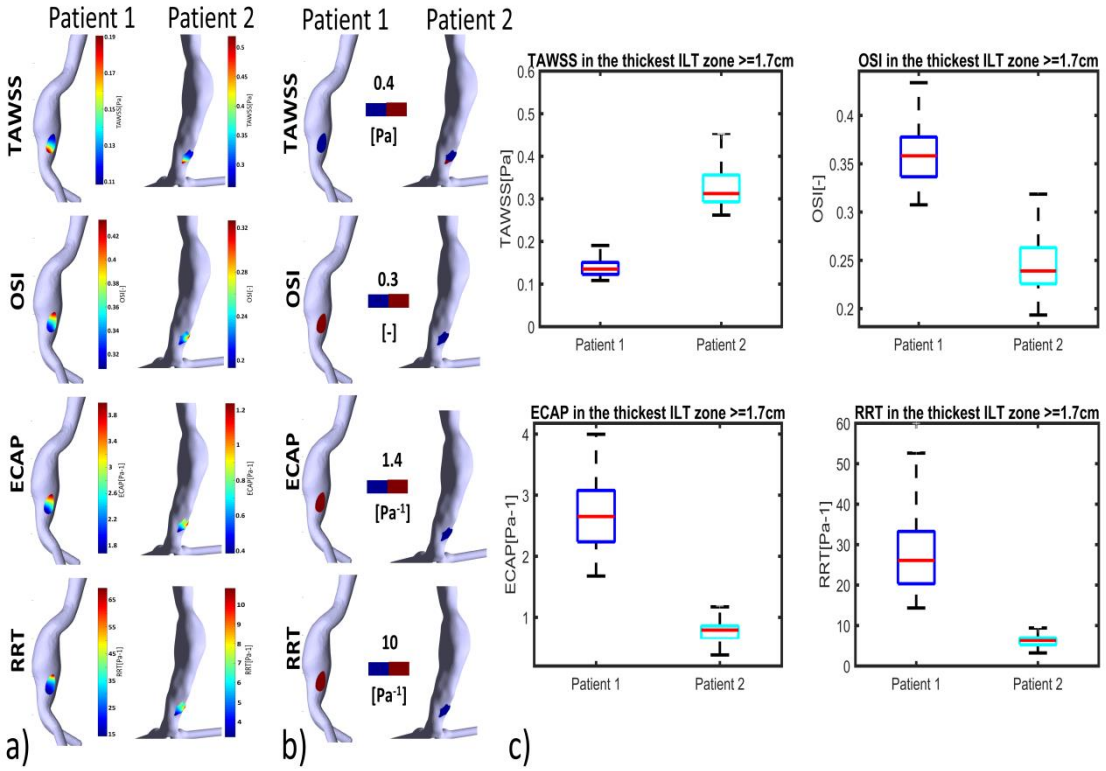

Figure. 6.13: Visualization of TAWSS, OSI, RRT and ECAP in AAA Patients 1 and 2 using CFD simulations in the thickest ILT zones with threshold $\geq 1.7\ \mathrm{cm}$: a) values indicated in the colormaps; b) values indicated in the colormaps with corresponding threshold used for each WSS-based parameter (Blue for values below threshold and Red for values above); and c) statistical boxplots.

Figures 6.13 and 6.14 illustrate the WSS descriptors in the thinnest and thickest ILT areas respectively for the two patients 1 and 2. In Fig 6.13a TAWSS, OSI, ECAP and RRT contours are shown. Similarly, Figure 6.13b shows these hemodynamic descriptors' distribution for the two patients with threshold to better visualize regions of low and high values.

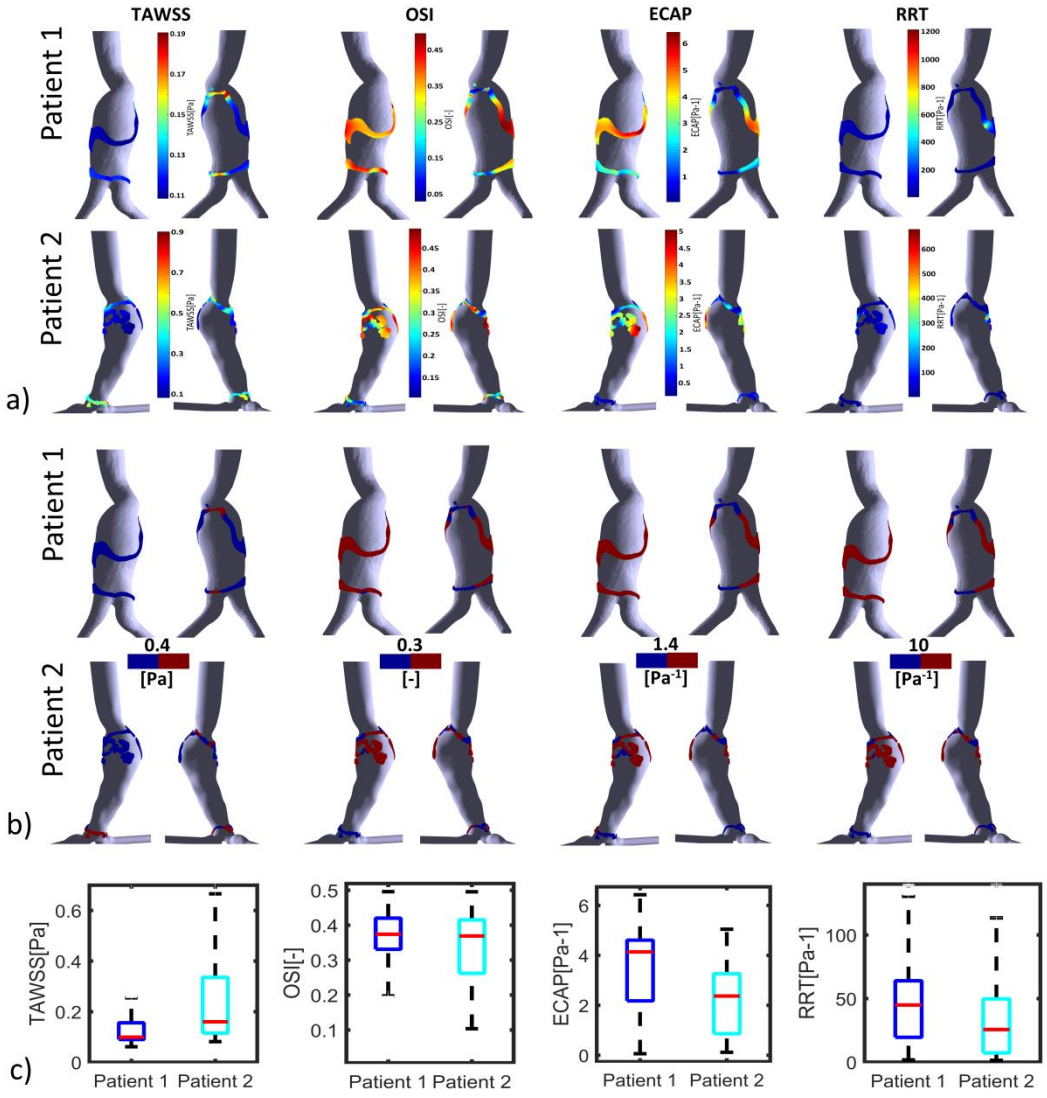

Figure 6.14: Visualization of TAWSS, OSI, RRT and ECAP in AAA Patients 1 and 2 using CFD simulations in the thinnest ILT zones with threshold ≤ 0.15 cm: a) values indicated in the colormaps; b) values indicated in the colormaps with corresponding threshold used for each WSS-based parameter (Blue for values below threshold and Red for values above); and c) statistical boxplots.

Representation via statistical boxplots was done in Figure 6.13c. For Patient 1, TAWSS is lower than the threshold value of 0.4 Pa [0.08 Pa to 0.18 Pa], OSI, ECAP and

RRT are higher than their corresponding threshold values (see Figure 6.13b and 6.12c). However, Patient 2 presents with the highest TAWSS compared to Patient 1 at the thickest ILT area, with values ranging between 0.26 Pa and 0.45 Pa. OSI, ECAP and RRT values where lower than the thresholds as it can be observed in (Figs 6.13a, 6.13b and 6.13c). These results show the WSS derivatives in the ILT regions exceeding or equal to 1.7 cm of thickness, comparable trends and observations are found when using 1.5 cm of thickness as the minimum value to define the thickest ILT zone.

Similar to Figure 6.13; Figure 6.14 explore the wall shear stress derivatives in ILT regions not exceeding 0.15 cm of thickness. For visualization purposes, two different views are displayed for each patient. The thinnest ILT regions of Patient 1 presents values corresponding to values favorable for ILT deposition in the proximal and distal parts of the AAA, except in the posterior wall as shown in the color-maps (Figure 6.14a), similarly presentations with thresholds are shown in Figure 6.14b and statistical boxplots (Figure 6.14c). Whereas in patient 2 we observe a difference between the WSS derivatives values in the proximal part and the distal part of the aneurysm. Contrary to the distal part, the proximal part of the thinnest ILT areas is favorable to ILT growth.

6.4. DISCUSSION

This study presents the relationship between ILT deposition and outcome data regarding hemodynamic parameters related to wall shear stress WSS exerted to the endothelial cells (EC) In this study, we selected a sample of three AAA patients with different ILT deposition area and different ILT thickness which makes this preliminary study significative to explore the possibility of using the differentiation between the hemodynamic characteristics in thinnest and thickest ILT areas as possible indicator in the management of AAA by predicting ILT growth. The co-localization and relationship between five WSS-based hemodynamic parameters and ILT deposition is addressed.

Results show the accumulation of ILT in flow recirculating area characterized by a low velocity magnitude. Regions devoid of ILT correlate to jet impingement areas formed inside the aneurysm sac. This result is in accordance with the previous evidence [32,71]; where the jet is formed at the neck and circulated through the AAA and impinging against the anterior wall as can be seen in Patients 1 and 3 in Figure 6.7.

For those two patients (Patients 1 and 3), the anterior wall is free of ILT, whereas the circulating zones created in the surrounding area, mainly in the posterior wall, are characterized by ILT accumulation.

Patient 3 presents a case of ILT initiation near to its lumen maximum diameter. This finding also agreed with the results found by Zambrano et al. [69] showing that the ILT accumulation process began at region of maximum diameter. However for patients 1 and 2, each presenting with both a thin and thick ILT areas, the maximum ILT thickness is found in the distal part of the aneurysm. For the two aforementioned patients, the maximum ILT zone was in the left side of the distal part of aneurysm, as shown by red zones in the rightmost column of Figures 6.11a and 6.11b. Figure 6.12 shows the relationship between ILT deposition and the WSS-based hemodynamic parameters: on one hand, there is a correlation between ILT deposition and low TAWSS; and on the other hand, a direct correlation exists between OSI, RRT and ECAP with ILT. As can be observed, Patient 3 is devoid of ILT and is characterized by higher TAWSS values in the AAA wall and lower OSI, RRT and ECAP values. Conversely, the aneurysm wall in Patients 1 and 2 is almost covered by ILT, corresponding to lower TAWSS and higher OSI, RRT and ECAP values. This accords with the results found by Tzirakis et al. [43] where patients with significant ILT deposition present low TAWSS values, below 0.5 Pa in the aneurysm sac (in our case less than 0.22 Pa and 0.51 Pa for Patient 1 and 2 respectively). Whereas in the patient devoid of ILT, the TAWSS attain higher values (reach 1 Pa in Patient 3).

This study is one of the fewest exploring the effect of TransWSS on ILT accumulation. According to our results, it was found that independently to the nature of the flow near the wall characterized by TransWSS (disturbed or non-disturbed flow), the ILT deposition area corresponds to low TAWSS and high OSI values as defined in tables 6.4, 6.5 and 6.6.

In figures 6.13 and 6.14, we displayed the WSS-based parameters in the thinnest and thickest ILT areas for patients 1 and 2. The results show WSS-based hemodynamic parameters favorable to ILT growth in the thickest and thinnest area for Patient 1. Whereas, Patient 2 presents hemodynamic characteristics unfavorable to ILT growth in the thickest region and thinnest ILT regions in the distal part of the aneurysm; and favorable conditions are found in the thinnest part situated in the proximal part of the

AAA. This suggest a strong potential of ILT growth in the thick ILT area for patient 1 while patient 2 shows a weak potential. Possible continuous growth of maximum ILT thickness for patient 1 can be predicted. This result shows the possibility of predicting ILT growth using the approach of determining the WSS-based indicators in the thinnest and thickest ILT areas of AAA patients. This approach opens a perspective to the study the effect of thin and thick ILT regions hemodynamics characteristics on ILT growth prediction.

6.5. CONCLUSIONS

In summary, this preliminary study focus on the investigation of the co-localization and relationship between ILT and WSS-based hemodynamic parameters (TAWSS, TransWSS, OSI, RRT and ECAP) in three realistic patients with AAA by using CFD simulations. Pulsatile flow was performed in ANSYS Fluent software and the non-Newtonian behavior of blood was modeled by using Carreau-Yasuda model. ILT segmentation and ILT thickness estimation are realized. CFD simulations enabled non-invasively the hemodynamic parameters acting on the endothelial cells. A mesh sensitivity analysis was highlighted, and the numerical methodology was validated against *in-vitro* research data from the literature. Our model allowed the evaluations of clinically relevant hemodynamics indexes.

High values of OSI, RRT and ECAP were found to co-localize with ILT deposition areas, whilst there was a correlation between regions with low TAWSS and ILT. ILT deposition areas were found in regions of low TAWSS and high OSI independently to the flow nature near the wall characterized by TansWSS.

Our Results indicate that the suggested approach which is based on the estimation of CFD-based WSS indexes in the thin and thick ILT areas extracted from the segmentation of real medical imaging data could provide tool to support clinicians' assessment and management of AAA patients. The results obtained in this preliminary study can lead to further studies that consider other clinical follow up data of large cohort of AAA patients in order to provide robustness to our methodology and our suggested approach.

Chapter 7

On the potential of 4D Flow in guiding CFD analyses: a case study of aortic coartaction patient *In-vivo* vs *in-silico*

7.1. INTRODUCTION

Coarctation of the aorta (CoA) is one of the most severe congenital heart diseases (CHD) which involves stenosis of the aortic segment. This malformation if not treated early, can lead to a decrease in life expectancy due to complications such as coronary artery disease, hypertension, stroke, rupture of the vessel and aneurysm formation. Typically, it is diagnosed in childhood and accounts for around 8%-11% of (CHD) [163].

In the last decade, derangements of the fluid dynamics within the region of interest have been investigated as possible diagnostic and prognostic markers of the pathology. In this context, novel *in-vivo* flow-encoding magnetic resonance (MR) imaging techniques and *in-silico* computational fluid dynamics (CFD) have been exploited to gain insights into the redistribution of flows and pressures [163,164].

Thanks to new technological developments in data analysis, image acquisition and reconstruction [92], magnetic resonance imaging (MRI) has undergone substantial developments and can provide, 3D angio scanning for morphological assessment and 4D Flow MRI, which combines volumetric spatial encoding with 3D blood velocity-encoding. Up to now, 4D Flow MRI is the unique way to measure and visualize full 3D time-dependent *in-vivo* blood flow [90], though with low spatial and temporal resolution [165]. Complementary, computational fluid dynamics (CFD) provide insights into the 3D blood flow and wall parameters with high spatial and temporal resolution compared to 4D Flow MRI. Moreover, CFD allows the use of virtual surgery planning by modifying the vessel in the planned or desired postoperative geometry [93]. However, their consistency with *in-vivo* data may be hampered by the used boundary conditions and the precision of complex patient-specific geometries.

A number of recent studies have been devoted to the use of *in-vivo* data in CFD calculations with the aim of helping surgeons make a decision regarding the surgical procedure and management of cardiovascular disease patients. However, there are few CFD studies about aortic coarctation based on 4d flow data, and there are no studies about a cohort of patients with coarctation using MR-derived data in guiding the realism of CFD models.

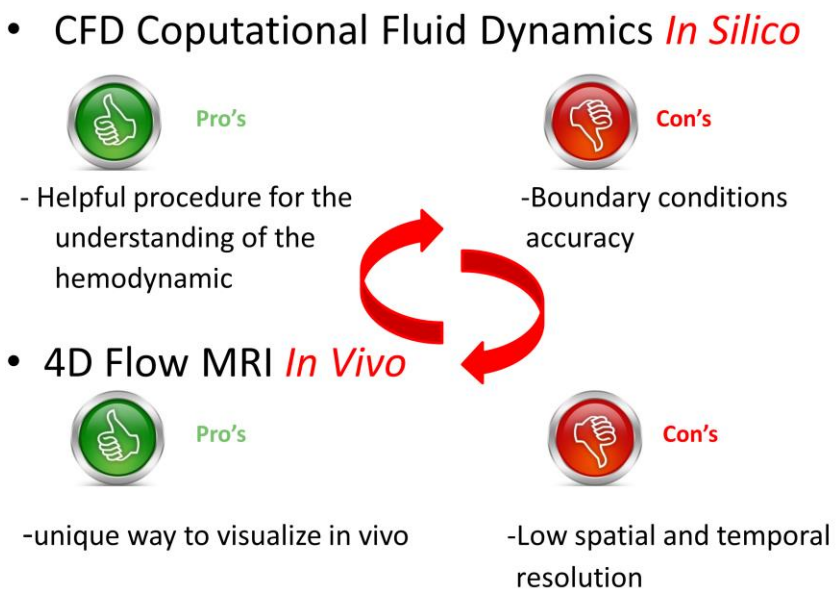

Figure 7.1: Coupling *in-silico* and *in-vivo* data present an important tool to benefit from the advantages of the two technics.

The present study takes into account the important aspects of validating the numerical simulation by using angio-MRI data to extract patient-specific geometry coupled with 4D Flow-based boundary conditions to obtain realistic CFD simulations. 3D velocity vector fields, pathlines and wall shear stress (WSS) distribution maps were obtained by 4D Flow and CFD and were compared. The study was conducted with data obtained from one patient with CoA at IRCCS Policlinico San Donato Milan.

7.2. MATERIALS AND METHODS

7.2.1. Workflow

The geometries of the numerical models were constructed from magnetic resonance MR angiography data. In-house Ad hoc software (developed in Politecnico di Milano by the Biomechanics group) was exploited to post-process 4D flow results and extracts the patient's specific boundary conditions to perform the numerical simulations.

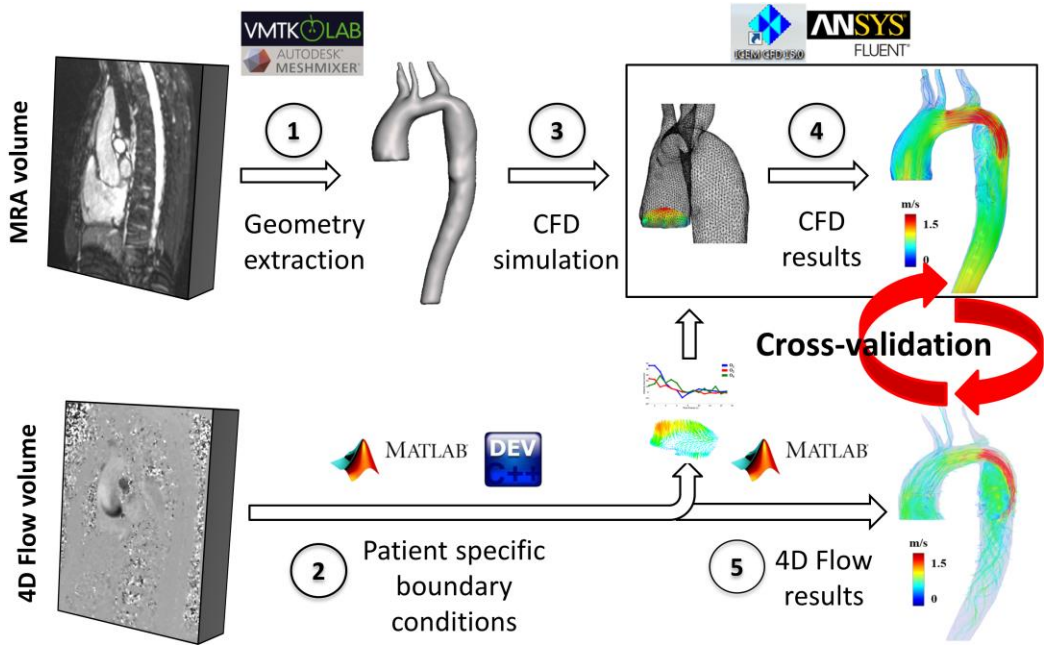

Figure 7.2: Schematic representation of the adopted workflow. Angiography MR data were used to extract patient-specific geometries. 4D Flow-based boundary conditions were used to obtain realistic CFD simulations (the Flowchart was also presented in detailed form in Chapter4 - see Figure 4.4).

In our study, the workflow displayed in Figure 7.2 is used for the combination of the CFD and 4D Flow MRI. The steps followed could be summarized as follow for MR sequences and CFD model respectively:

7.2.1.1. MR sequences

The MR acquisition could be summarized by the following step:

i. MRA: MR angiography with a voxel size of 1.09x1.09x1.10 mm3

ii. 4D Flow: 3D time-resolved phase-contrast cardiac magnetic resonance with velocity encoding (VENC) set to 200cm/s with a voxel resolution of 1.77×1.77x2.00 mm3 and ECG-gating during free-breathing.

iii. Analyzing the 4D Flow data by an ad-hoc MATLAB code(The MathWorks Inc., Natick, MA, United States), in order to extract the 3D velocity field and yield to the use of these data as boundary conditions in CFD simulations.

7.2.1.2. CFD model

Patient-specific geometries of the aorta were extracted from magnetic resonance angiography (MRA) imaging by using VMTKLab (Orobix Srl, Bergamo, Italy).

Simulations were performed through a two-step approach, first a steady state simulation and then three consecutive cardiac cycles.

The CFD boundary conditions were defined according to the 3D velocity field extracted from the 4D Flow volume following the methods proposed in [166]. The temporal variations of these physiological conditions were reproduced and implemented through a user_defined_function (UDF) script (see C++ script in Appendix B3). The simulation study protocol consisted in the following steps:

i. Patient-specific geometries extraction (from MRA).

ii. Geometries reconstruction and volumetric mesh were then computed in ANSYS ICEM CFD (ANSYS, Inc., Canonsburg, USA).

iii. Generate a steady-state solution that will be used as an initial condition for the time-dependent solution.

iv. Define an unsteady boundary condition using a user_defined_function (UDF) based on the acquired 4d flow data.

v. Calculate a transient solution.

vi. Saving and post-processing time-dependent data sets.

7.2.2. Patient and MR data acquisition

MR acquisitions were performed on a 1.5 T scanner (Magnetom Aera, Siemens Healthcare, Erlangen, Germany). Two MR sequences were acquired: gadolinium-enhanced MR angiography (MRA), and 3D time-resolved phase-contrast cardiac magnetic resonance, with prototype pulse sequences for three-directional velocity encoding (4D Flow). The MRA volume was acquired prescribing a voxel size resolution of 1.09×1.09x1.10 mm3 (echo time = 0.95 ms, repetition time = 2.67 ms, flip angle = 25°). The 4D Flow volume of the acquisition was oriented along a sagittal plane encompassing the ascending aorta, the aortic arch and the thoracic aorta. An almost isotropic voxel resolution of 1.77×1.77x2.00 mm3 was prescribed [90]. The remaining parameters were: echo time = 2.44 ms, repetition time = 38.72 ms, flip angle = 8°, and temporal resolution = 45.27 ms. Data were acquired with prospective ECG-gating during free-breathing, using a respiratory navigator. The velocity encoding range (VENC) was properly set to 200 cm/s after scouting on cross-sections positioned in the ascending aorta and downstream of the coarctation. Exploiting *ad*

hoc in-house MATLAB software MATLAB (The MathWorks Inc., Natick, MA, United States), 4D Flow data were analyzed yielding the time-dependent 3D velocity field within a user-defined region of interest (ROI) [166].

7.2.3. 4D Flow based CFD simulation

A semi-automated segmentation was used to extract the aortic inner-wall of the patient-specific from the MRA volume through a level sets algorithm available in VMTKLab (Orobix Srl, Bergamo, Italy). The aortic inner-wall surface was clipped distally, at the three supra-aortic branches and the descending aorta to create the outlet surfaces. The ascending aortas were clipped in the sino-tubular junction, to define the inlet surfaces (Figure 7.3). The segmented volume was exported as a .stl file. Additional manual smoothing was applied to the geometries by using Meshmixer (Autodesk, San Rafaeil, CA, USA) before generating the computational mesh using Icem CFD (ANSYS, Inc., Canonsburg, USA).

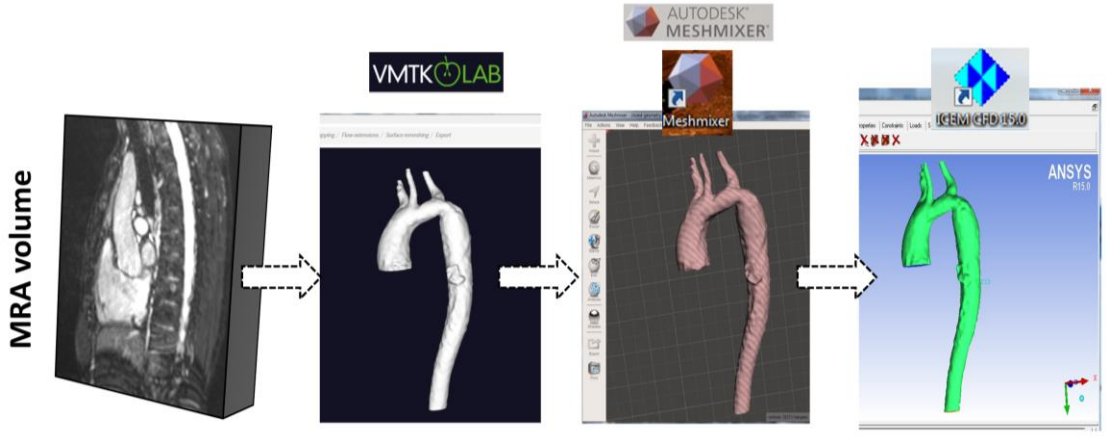

Figure 7.3: Steps followed in the segmentation of the inner-wall from MRA data.

7.2.4. Mesh sensitivity analysis

The mesh was refined in the near-wall region and mesh independence analysis was performed for the computational domain (see Table 7.1). Velocity vectors coloured by velocity magnitude are shown for different mesh sizes (see Figures 7.4a and 7.4b). As it can be seen mesh 3 and 4 show similar velocity distribution and the maximum velocity region is captured at similar areas. The optimum mesh size was determined once the peak wall shear stress and the maximum velocity values do not increase by more than 3%. Based on this analysis, the final mesh grid was selected.

Table 7.1: Meshes parameters with corresponding maximum velocity values

mesh	Number of Cells [millions]	Maximum velocity [m/s]	Diff/mesh4
Mesh1	0.25	2.04	- 11.7%
Mesh2	2	2.26	-2.1%
Mesh3	3.4	2.38	+3%
Mesh4	5.7	2.31	-

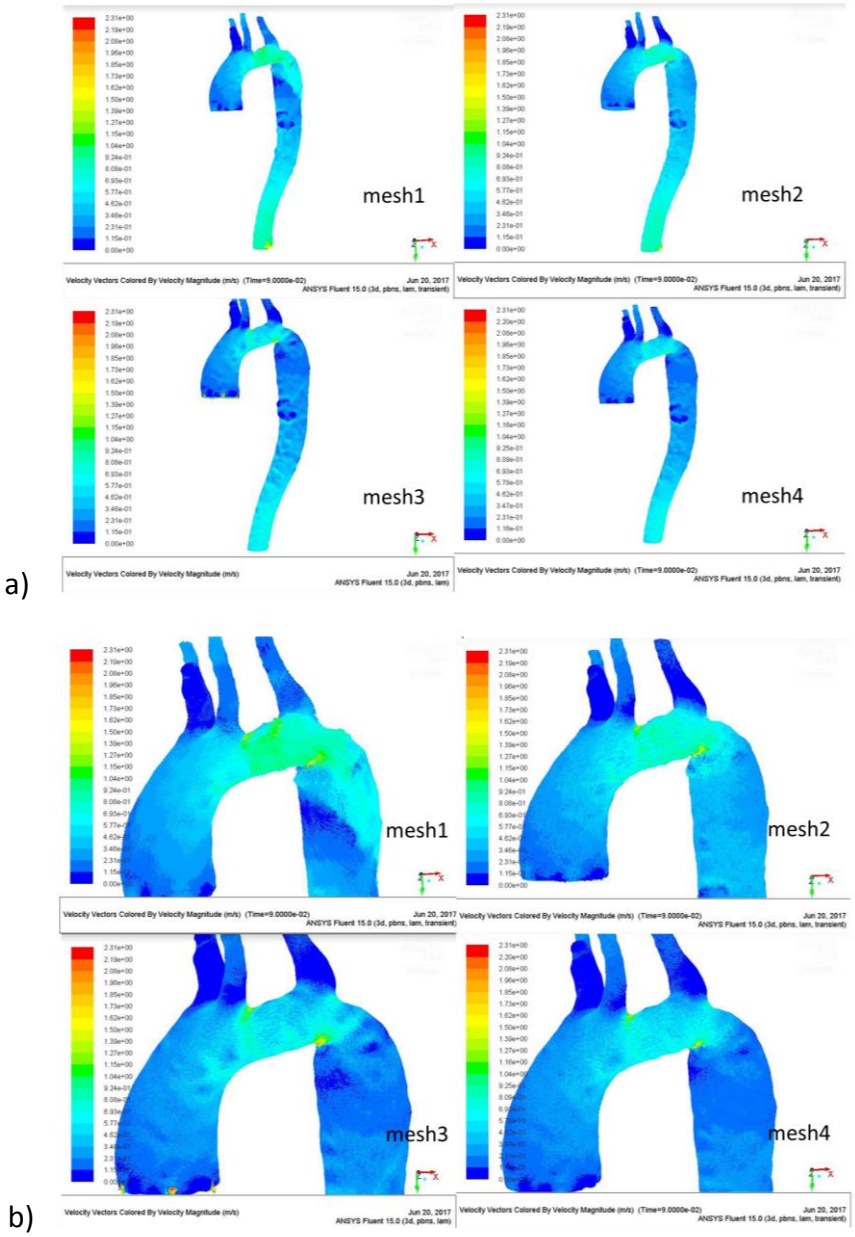

Figure 7.4: Velocity vectors colored by velocity magnitude [m/s] for four different mesh (mash 1 to 4 from coarse to fine mesh respectively). a) All the domain is shown b) the thoracic aorta is shown with aortic branches.

7.2.5. CFD model

Computations were performed by using the finite volume solver Fluent (Ansys, Fluent Inc, Lebanon, NH, USA). For the solution of the governing equations of mass conservation and Navie–Stokes (see equations 3.15 and 3.16 in chapter 3 governing equation section) a second-order upwind scheme was used. A second-order upwind scheme was used for spatial discretization and the PISO (implicit operator splitting pressure) algorithm for pressure-velocity coupling. For temporal discretization using the Iterative time advancement scheme every time frame of the cycle was divided into 50 time steps as mentioned in detail in Table 7.2. The convergence criteria for the continuity and the velocity are in the order of 10-5 and 10-4 respectively.

A rigid wall with no-slip condition was assumed at the aortic wall. Blood was considered as an incompressible and Newtonian fluid, with a homogeneous dynamic viscosity of 0.0035 Pa s, and a density of 1050 kg/m3.

Three cardiac cycles were simulated to minimize the influence of initial conditions, and the last cycle was considered in our results. The calculation time for CFD was about 5 to 15 days for each cardiac cycle using the Polimi (Politecnico di Milano) cluster.

An in-house MATLAB code (The Mathworks Inc., Natick, MA, United States) and ANSYS CFD-Post (Ansys, Inc.) were used for the post-processing of the CFD data.

Table 7.2: Temporal discretization used in the numerical calculation of CoA patients

	Number of Time Frame (-)	**Time Frame size (ms)**	**Time step size (ms x 10^{-2})**	**Number of time step per cycle (-)**	**Cycle size (s)**
CoA Patient	15	45.3	90.6	50	0.6795

7.2.6. Boundary Conditions

The CFD boundary conditions were defined according to the 3D velocity field extracted from the 4D Flow volume. Specifically, the inlet and outlet surfaces of the CFD model were registered in the 4D Flow volume by applying a rigid transformation computed according to the relative orientation of MRA and 4D Flow scans. The

discrete velocity field was sampled within the ROI on the cross sections identified by S_{in}, S_{out},1-2-3, following the methods proposed in [166]. The extracted points were used to define: i) the full 3D velocity profile at Sin (Inlet real profiles in the ascending aorta), ii) the net flow rate at S_{out}, 1-2-3 (3 aortic branches). At S_{out}, 4 (descending aorta) a zero-pressure boundary condition was applied (Figure 7.5).

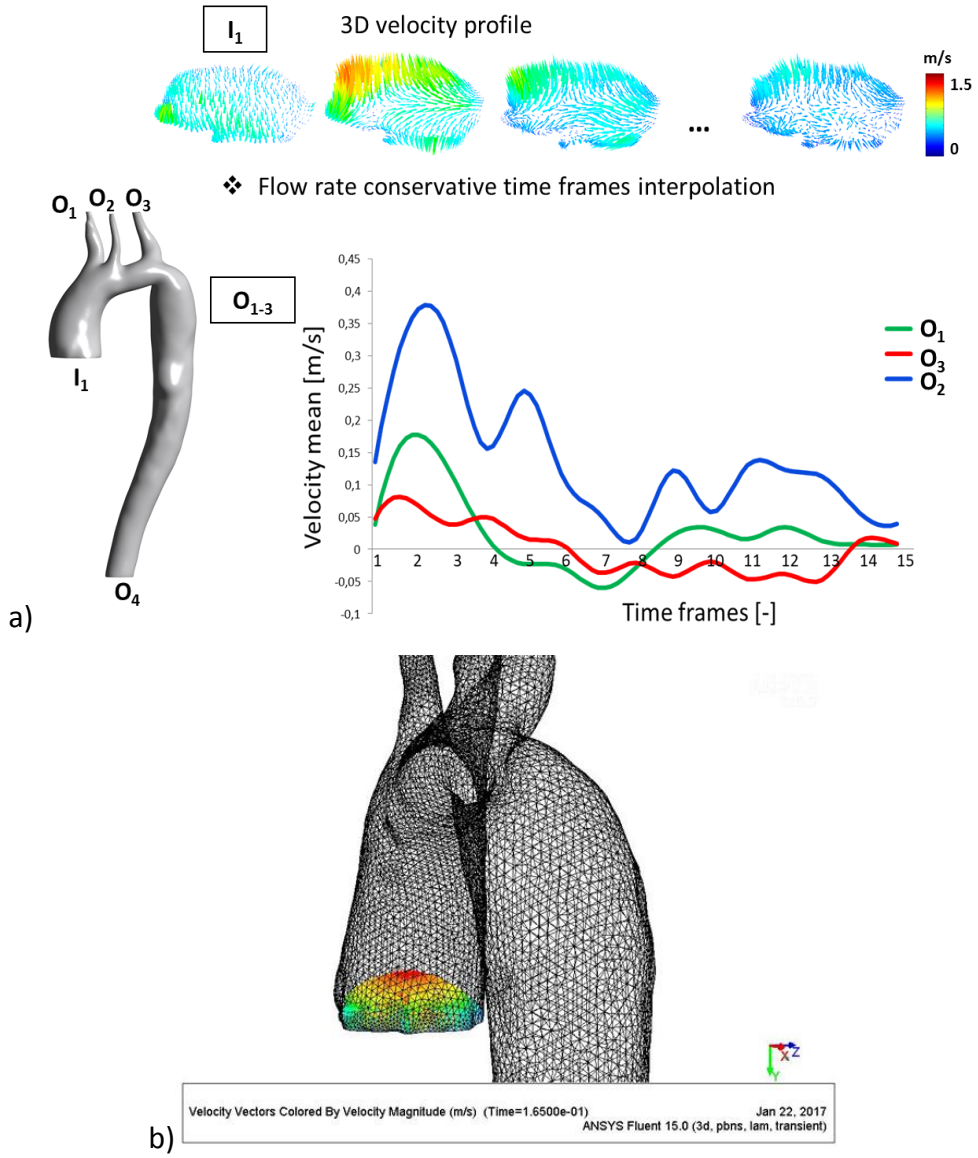

Figure 7.5: a) To obtain realistic CFD simulations 4D Flow-based boundary conditions were used with Inlet 3D velocity profiles after flow-rate conservative temporal interpolation. Velocity at the three supra aortic branches, while zero-pressure in the descending aorta were adopted as boundary condition. b) Example of 3D profile in the inlet of the CFD domain.

The inlet profiles were reproduced from 4D flow data to UDF using the Gaussian function (see Appendix B2). 2D Gaussian function was applied for each point of the

inlet grid and the final applied function was the summation of all the Gaussian functions.

7.2.6.1. Gaussian function

To explain the principle of gaussina function we show in Figure 7.6 , 1D and 2D gaussina function . The graph of a Gaussian forms the characteristic symmetric "bell curve" shape of the Gaussian/normal distribution, and has the general form in 1D and 2D respectivly:

1D Gaussian function

$$f(x) = A \exp\left(-\left(\frac{(x-x_0)^2}{2\sigma_x^2}\right)\right) \quad (7.1)$$

2D Gaussian function

$$f(x,y) = A \exp\left(-\left(\frac{(x-x_0)^2}{2\sigma_x^2} + \frac{(y-y_0)^2}{2\sigma_y^2}\right)\right) \quad (7.2)$$

A is the Amplitude (correspond to Vz velocity component in our case and similarly for Vx and Vy components).

x_0, y_0 are the center coordinates (corresponds to the cells centers in the inlet CFD grid in our case)

σ_x, σ_y Are the x and y spreads of the Gaussian blob

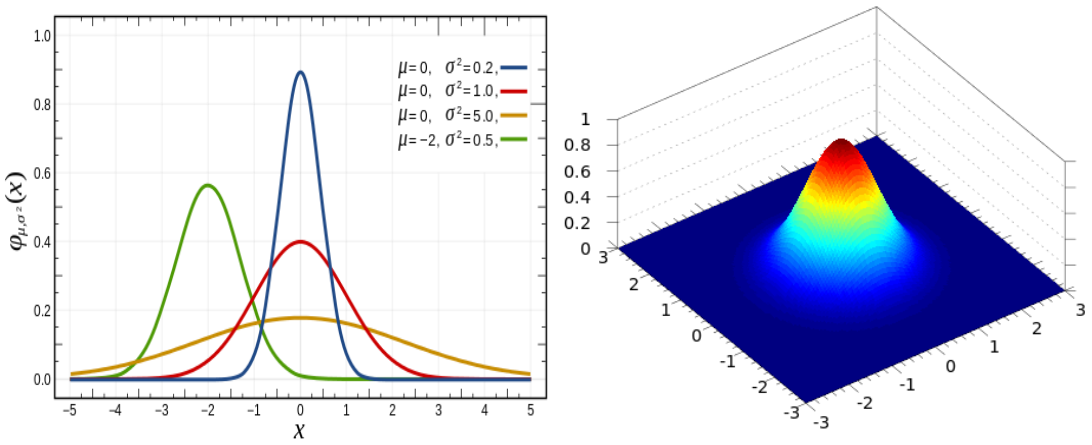

a) b)

Figure. 7.6: a) 1D Gaussian function b) 3D plot of a Gaussian function with a 2D domain [167].

In our work, we exploited the characteristic of the Gaussian function where we could attribute an exact value at the dome center, and zero value in the remaining regions of the 2D surface giving the possibility to apply for each cell center of the inlet surface a corresponding 2D Gaussian function where the amplitude A of the function corresponds to the through-plane component of the velocity value

extracted from *in-vivo* data (4D flow). Using this methodology it was possible to have for each cell of the inlet surface three velocity components Vx Vy and Vz (head to foot H-F, posterior to anterior P-A and left to right L-R). A MATLAB script was developed to prepare and write automatically the adequate *in-vivo*-based equations necessary for the user_defined_function.

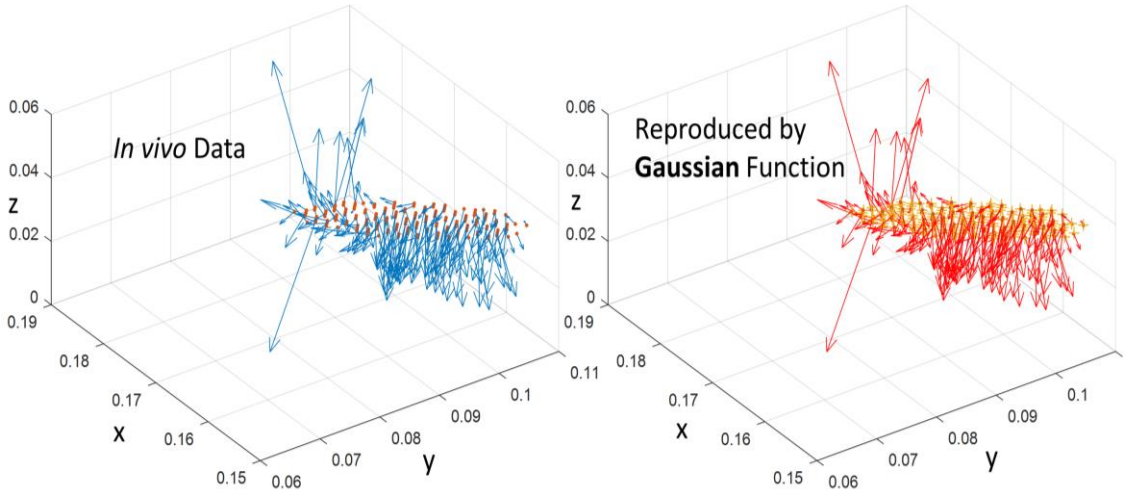

Figure. 7.7: Example of real 3D profile (*in-vivo*) (right column in blue arrows) and *in-silico* (red arrows) used in the CFD simulations (right column) at one time frame of the cardiac cycle. Brown points correspond to the mesh cells' centers at the inlet surface.

The script developed is able to optimise the reproduced real 3D profile as it can be seen in figures 7.7 and 7.8, showing the *in-vivo* (real) 3D profile and the reproduced profile at different time frames of the cardiac cycle. A quantitative comparison is shown in Table 7.3 confirming the precision of our UDF based on Gaussian function.

Table 7.3: Quantitative comparison between *in-vivo* data (4D Flow) and reproduced *in-silico* data used in the UDF as an inlet boundary condition to launch the CFD simulations.

	4D Flow	**Gaussian (UDF)**	**Difference /4D Flow (%)**
Vmag_max [m/s]	0.43499	0.43497	0.003 %
Vmag_mean [m/s]	0.15898	0.15949	0.32 %

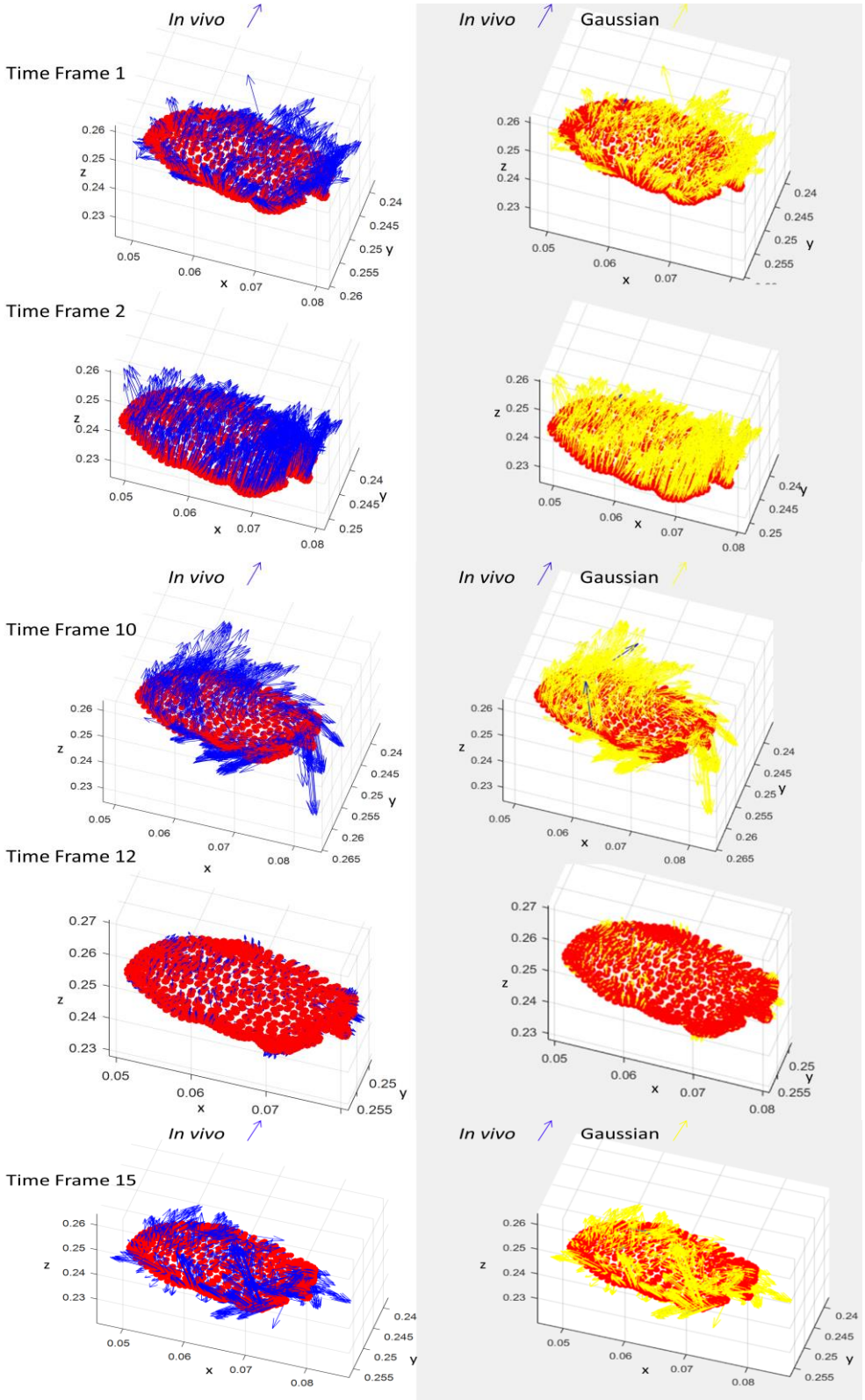

Figure 7.8: Real 3D profile (*in-vivo*) (right column in blue arrows) and *in-vivo* (blue arrows) vs reproduce profile (yellow arrows) used in the CFD simulations (right column) at different time frames of the cardiac cycle. Red points correspond to the mesh cells centers at the inlet surface.

7.3. RESULTS AND DISCUSSION

Simulated systolic fluid dynamics well compared with ground-truth 4D Flow data, reporting a qualitatively similar pattern of the blood velocity field. Computed streamlines highlighted the persistence of a high-velocity jet passing across the coarctation region from mid to late systole (Figure 7.9). Consistently with 4D Flow data, recirculation zones were observed proximal to the coarctation jet as well as in the concavity of the ascending aorta. The top view is also shown in Figure 7.10.

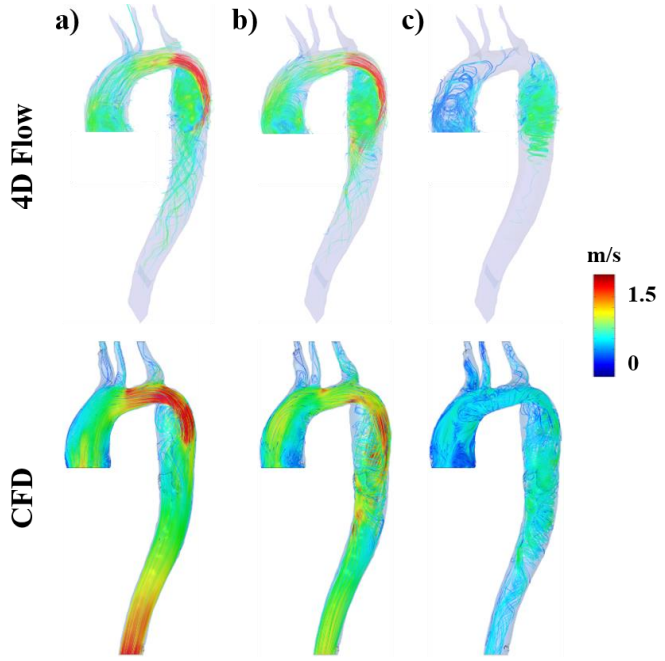

Figure 7.9: Representation of streamlines colour-coded by velocity magnitude for CFD simulations and 4D Flow measurements of CoA patient at Peak- mid- and late systole respectively (from left to right). The streamlines show a qualitatively similar pattern of blood velocity fields.

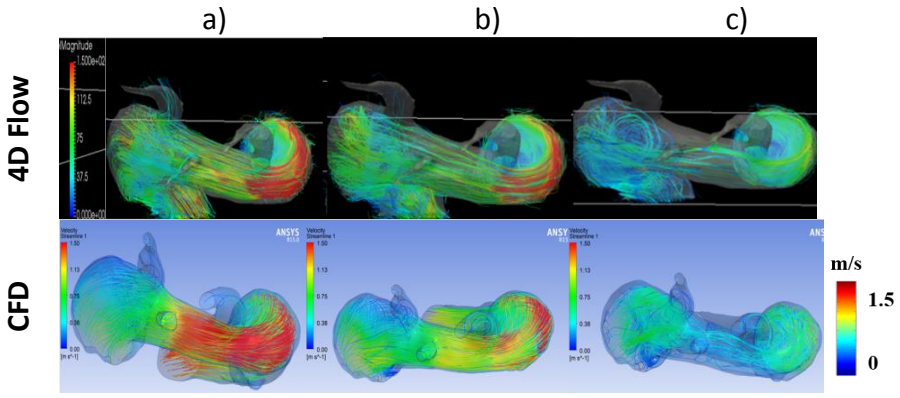

Figure 7.10: Top view of Streamlines computed at the time-frames corresponding to peak (a), mid (b) and late (c) systole.

At peak systole, we quantitatively compared CFD results and 4D Flow data on three different aortic cross sections: i) in the proximal ascending aorta close to pulmonary trunk plane 1 (P1), ii) downstream of the aortic arch plane 2 (P2) and iii) in the distal descending aorta plane 3 (P3) (Table 7.4).

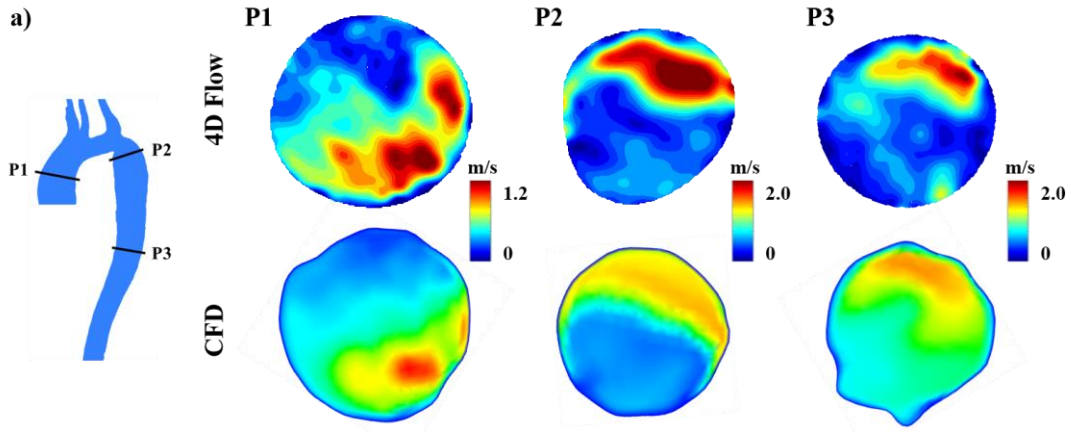

Figure 7.11: Velocity distributions in three selected cross-sectional planes along the aorta the studied for the CoA patient. Comparison between 4D Flow measurements and CFD results. In general, an excellent agreement is found between the measurements and the simulations at every plane.

On all the selected cross-sections, the CFD analysis captured the patterns of the velocity field reported by the 4D Flow processing (Figure 7.11). However, CFD underestimated peak velocity values ($|v|max$) by 2% and 24% in the ascending and descending aorta, respectively (Table 7.4). The length of the blood jet passing across the coartaction was comparable and equal to about 53 mm. When focusing on the wall shear stress (WSS) field, the CFD model well-captured the high- WSS region downstream of the coartaction, as visible in the 4D Flow dataset, even if the computed WSS peak values were an order of magnitude higher than the ones estimated with 4D Flow data (Figures 7.12 and 7.13). Of note, this result is in accordance with previous evidences [166, 168]. This is an open issue and different techniques are now being tested to enrich 4D Flow data and extract more reliable derivative quantities [166,169-172].

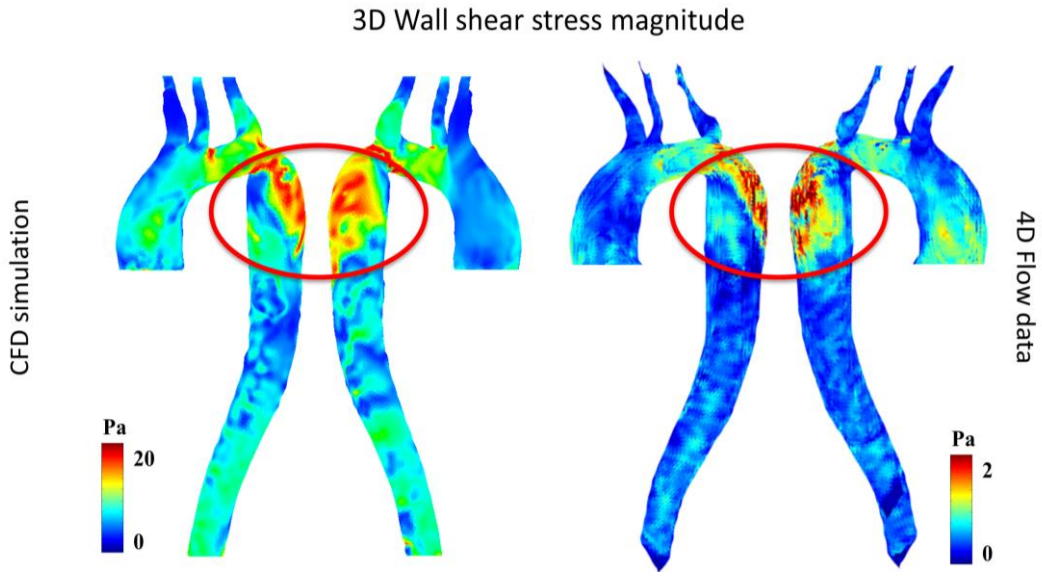

Figure 7.12: Visualization of Wall shear stress distributions in CoA patients using 4D Flow measurements and CFD simulations at peak systole. The computed CFD WSS peak values are an order of magnitude higher than the ones estimated with 4D Flow data.

Table 7.4: Results of 4D Flow post-processing and of CFD simulation

	4D Flow	**CFD**
$\|v\|_{max,\,Tps}$ ***(m/s)***		
Plane 1	1.34	1.32 (-1.5%)
Plane 2	2.23	1.70 (-23.8%)
Plane 3	2.01	1.81 (-9.9%)
L_{Jet} ***(mm)***	52.9	53.3 (+0.7%)
$\|WSS\|_{max,\,Tps}$ ***(Pa)***	2.3	22.9
L_{WSS} ***(mm)***	58.6	60.1 (+2.6%)

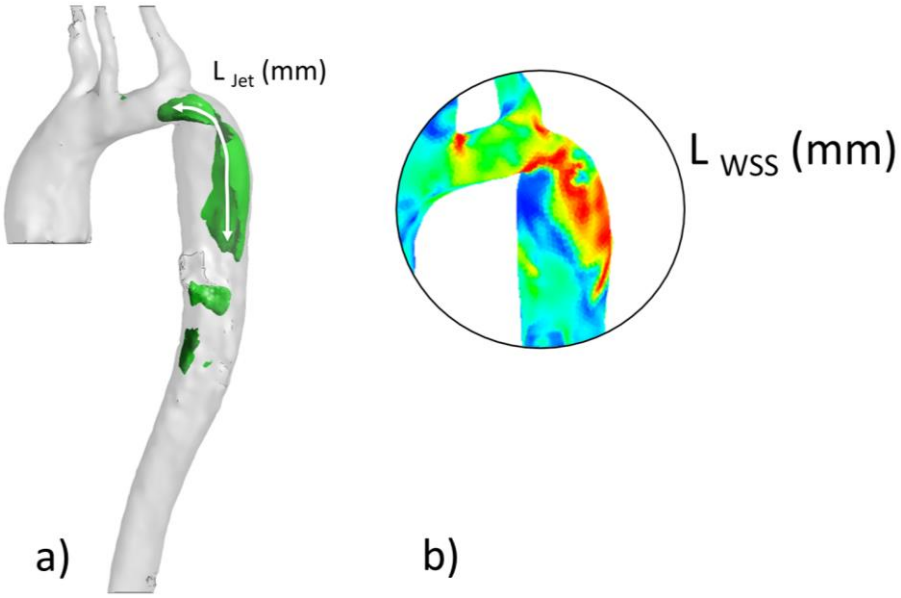

Figure 7.13: 4D Flow post-processing and CFD simulation results. Geometrical parameters related to the jet propagation, jet length (L_{jet}) (a) and related wall shear stress distribution (L_{WSS}) (b). Percentage variations of CFD results with respect to those obtained by 4D Flow are reported in table 7.4.

7.4. CONCLUSION

In this work, the importance of the use of *in-vivo* and *in-silico* data to facilitate diagnosis, risk stratification, treatment and understanding of cardiovascular diseases in general and in the case of the management of patients suffering from aortic coarctation (CoA) was explained. The verification and the cross-validation of the two techniques were also checked, thus suggesting that the main features were well captured. Our workflow is going to be refined to confirm the feasibility and to further enhance and obtain more accurate computation results. The use of CFD results provides insights into the 3D blood flow and wall parameters with a high spatial and temporal resolution which is very important in the management of patients suffering from cardiovascular diseases. As suggested by our preliminary results, the realism and reliability of CFD simulations can be assessed by comparison with ground-truth *in-vivo* 4D Flow data. Also, comparisons between more refined variables, e.g. WSS, owing to their improved estimation from 4D Flow data [165], may contribute to evaluating the outcomes of CFD models, which would allow, if further optimized to obtain more accurate computations of the considered variables.

General Conclusions and Perspectives

GENERAL CONCLUSIONS

Cardiovascular diseases could affect children as they can affect elderly persons, they could be either acquired or congenital. The mortality rate from cardiovascular disease is higher in middle- and low-income countries compared to developed countries [1]. In Algeria surveys and statistical analysis are usually conducted by different institutions, hospitals and laboratories; however, studies related to the management of cardiovascular diseases, the integration and the use of the newest technologies in the management of patients are still lacking.

With the development of computing capabilities and high-performance calculations, the use of complex numerical models with lower time consumption become possible in the aim to understand the physiopathology and the altered hemodynamic conditions in cardiovascular disease. To reproduce complex flow behavior and mimic the realistic data medical imaging resources are needed. This technological development led the Food and Drug Administration FDA to approve for the first time the use of computational fluid dynamic models in clinical use [61]. Furthermore, computational fluid dynamic methods present the advantage of giving the possibility to investigate noninvasively the cardiovascular disease and consequently present a good tool for clinicians.

In this thesis, we focus on two diseases which affect the aorta the main artery in the cardiovascular system. Abdominal aortic aneurysm AAA and aortic coarctation CoA will be studied in this thesis.

The current clinical guidelines suggest considering the maximum diameter as a criterion for planning and surgical intervention for patients with AAA; this approach is too simplistic. Numerical methods could help in addition to overlooking other morphological parameters that are associated with the risk of rupture in the management of patients and to better stratify the risk for AAA rupture by determining additional criteria to help surgeons make clinical decisions regarding surgical intervention.

The main objective of using numerical simulations in the study of AAA is to understand the hemodynamics in this disease and consequently define the relationship between on one hand geometric parameters of AAAs and on the other

hand wall shear stress derivatives and wall strain. In chapter 5 the effect of the asymmetry of AAA is studied using CFD. A detailed parametric analysis of flow dynamics using five virtual AAA models was performed. Flow behaviour and wall shear stress derivatives (time-averaged wall shear stress TAWSS, and oscillating shear stress OSI) were investigated.

In this study, numerically; the spatial distribution and the temporal evolution of wall shear stresses were also studied. In addition, hemodynamic parameters such as OSI and TAWSS were analyzed to define the effect of AAA asymmetry on the possible risk of rupture and on the promotion of thrombus formation. The presented results show that the symmetric aneurysm is subjected to low and oscillating wall shear stresses, which could favour intraluminal thrombus (ILT) deposition, and growth and endothelial dysfunction. Although the studied symmetric and asymmetric AAA models have an equal maximum diameter, the asymmetry of AAA has a clear impact on the flow behaviour and WSS derivatives values which could favour their susceptibility to rupture and the formation of ILT. This study confirms the necessity to define other morphological parameters as a supplemental criterion in decision-making and endorses similar studies.

Chapter 6 is devoted to investigating the co-localization and relationship between ILT and WSS-based hemodynamic parameters (TAWSS, OSI, Transversal WSS transWSS, relative residence time RRT and Endothelial cell activation potential ECAP). Computed Tomography CT data of three AAA patients were used. CFD simulations with the pulsatile flow were performed and blood was modelled as non-Newtonian using the Carreau-Yasuda model. The model was validated against in-vitro data. CFD simulations enabled non-invasively the evaluation of clinically relevant hemodynamic indicators. A new approach was suggested approach in the aim to predict ILT deposition and growth based on WSS indexes in the thin and thick ILT areas. This tool could support clinicians' assessment and management of AAA patients.

An accurate prediction of fluid dynamics-related quantities in aortic coarctation is pivotal to support clinicians in the decision-making process and post-operative treatment planning. To date two possible approaches are possible; CFD and 4D flow. CFD allows for a high-resolution calculation of fluid dynamic quantities but its

accuracy is strongly dependent on the assumption of the model (e.g. boundary condition, geometry); 4Dflow provides true in-vivo data of the analyzed patient, but with spatial and temporal resolution which doesn't allow for accurate quantification of hemodynamics. In Chapter 7, a workflow combining in-vivo (4D flow MR) and in-silico (CFD) data in the case of patients suffering from aortic coarctation (CoA) was explained. The adopted methodology allowed for capturing the main features of the CFD model. The verification and the cross-validation of the two techniques were also checked, this study confirms the robustness of CFD to mimic realistic 3D blood flow and wall parameters with a high spatial and temporal resolution which is very important in the management of a patient suffering from cardiovascular diseases. As suggested by our preliminary results, the realism and reliability of CFD simulations can be assessed by comparison with ground-truth in-vivo 4D Flow data. Also, comparisons between more refined variables, e.g. WSS, owing to their improved estimation from 4D Flow data [165], may contribute to evaluating the outcomes of CFD models, which would allow, if further optimized to obtain more accurate computations of the considered variables.

PERSPECTIVES

The main objective of using numerical simulations in the study of AAA is to understand the hemodynamics in this disease and consequently define the relationship between on one hand geometric parameters of AAAs and on the other hand wall shear stress derivatives and wall strain. To endorse our results found in Chapter 5 and the approach suggested in Chapter 6, a future study incorporating fluid-structure interaction (FSI) patient-specific boundary conditions (BCs) to feed patient-tailored simulations is needed. Further verification of current results is required, and a replication of this analysis should be performed using a multicenter and larger sample size of patients is necessary, along with the acquisition of a follow-up CT scan to develop a clinical tool for the management of AAA patients to confirm these findings.

Similarly to AAA, for aortic coarctation CoA, future work including large size of patients is conceivable in perspective. In this study, we chose to focus on flow

parameters and the wall shear stress acting on the wall. However, in CoA pressure gradient prediction is the clinical gold standard by clinicians to diagnose CoA and is measured through invasive catheterization. CFD guided by 4D flow MRI and validated by comparison with the in-vivo flow behaviour could be a good alternative and non-invasive tool to estimate the pressure drop (PD) in the diagnosis of CoA.

In addition to CFD and FSI modelling, artificial neural network ANN, and physics-informed neural network PINN learned and fed by CFD and FSI results are of interest in guiding clinicians in the management of patients with cardiovascular diseases.

Appendix A

Detailed Numerical Method for Solving Navier-Stokes Equations in ANSYS Fluent

A.1. SOLVING THE LINEAR SYSTEM

The discretized transport equation of the scalar (see equation 4.2 in Chapter 4) contains the unknown scalar variable Φ at the center of the cell, as well as the unknown values in surrounding neighboring cells. This equation, in general, is non-linear with respect to these variables. A linearized form of equation 4.2 can be written as follows:

$$a_p \Phi = \sum_{nb} a_{nb} \Phi_{nb} + b \qquad (A.1)$$

Where the index nb refers to neighboring cells, and a_p and a_{nb} are the linearized coefficients for Φ and Φ_{nb} .

The number of neighbors of each cell depends on the grid topology, but generally it is equal to the number of faces surrounding the cell (boundary cells being the exception).

Analogous equations can be written for each grid cell. This results in a set of algebraic equations. For scalar equations, FLUENT solves this linear system using an implicit point (Gauss-Seidel) linear equation solver in conjunction with an algebraic multi-grid (AMG) method.

A.2. IMPLICIT TIME INTEGRATION (CORRESPONDS TO THE PRESSURE-BASED SCHEME)

One of the methods consists in evaluating F(ϕ) at the future time step:

$$\frac{\Phi^{n+1} - \Phi^n}{\Delta t} = F(\Phi^{n+1}) \qquad (A.2)$$

This is an implicit integration of the fact that Φ^{n+1} in a given cell is connected to neighboring cells through $F(\Phi^{n+1})$.

$$\Phi^{n+1} = \Phi^n + \Delta t\, F(\Phi^{n+1}) \qquad (A.3)$$

This implicit equation can be solved iteratively at each time step before proceeding to the next step.

The advantage of this scheme is that it is totally implicit and that it is unconditionally stable whatever the time step.

A.3. GRADIENTS AND DERIVATIVES EVALUATION

Gradients are not only needed to construct scalar values on cell faces, but also to calculate secondary scattering terms and velocity derivatives. The gradient of a variable ϕ is used to discretize the convection and diffusion terms in the flow conservation equations.

Gradients in FLUENT are calculated using three methods:

- Green-gauss cell-based
- Green–gauss node-based
- Least squares cell-based

A.3.1. Green-Gauss theorem

When the Green-Gauss theorem is used to calculate the gradients of a scalar ϕ at the center of cell c0, the following discrete form is used:

$$(\nabla\Phi)_{c0} = \frac{1}{V_{c0}} \sum_{f} \overline{\Phi_f} \ \overrightarrow{A_f} \qquad (\mathrm{A}.4)$$

Where ϕf is the value of Φ at the center of the cell calculated as will be seen below. The summation is done over all the cells surrounding the considered cell.

Among the three methods existing under Fluent and cited above, we opted for the cell-based model mainly because of its high accuracy in the case of unstructured meshes.

A.3.2. Green-Gauss Cell-Based Gradient Evaluation

By default, the nominal value, $\overline{\Phi_f}$ in equation A.4 is taken from the arithmetic mean of the values at the centers of neighboring cells centers, i.e.,

$$\overline{\Phi_f} = \frac{\Phi_{c0} + \Phi_{c1}}{2} \qquad (A.5)$$

A.4. DISCRETIZATION OF THE MOMENTUM EQUATION

The discretization schemes seen previously in the discretization section are used to discretize the momentum equation. For example, for the momentum equation along x, we set ϕ=u, and we obtain:

$$a_p\, u = \sum_{nb} a_{nb}\, u_{nb} + \sum p_f\, A\, .\, i + +S \qquad (A.6)$$

If the mass fluxes on the faces and the pressure are known, the previous equation can be solved in the same way as the one we saw previously and a velocity field is obtained. However, the mass fluxes on the faces and the pressure are not known in advance and must be obtained as part of the solution; this is an important issue with regard to the storage of pressure and the discretization of pressure gradients; this is what we will see in what follows.

FLUENT uses a co-located scheme. In this diagram, the pressure and the velocity are stored at the center of the cells.

However, the previous equation requires knowing the value of the pressure on the face between cells c0 and c1; therefore, an interpolation scheme is necessary to calculate the values of the pressure at the faces of the cells.

A.4.1. Pressure interpolation Schemes

The default interpolation scheme interpolates the pressure on the face using the coefficients from the momentum equation:

$$p_f = \frac{\frac{p_{co}}{a_{p.co}} + \frac{p_{co}}{a_{p.co}}}{\frac{1}{a_{p.co}} + \frac{1}{a_{p.co}}} \qquad (A.7)$$

This procedure works well as long as the pressure variation between cell centers is smooth. When there are jumps or large gradients in the momentum source terms between control volumes, the pressure profile has a large gradient at the face of the cells, and cannot be interpolated using this scheme. If this scheme is used, an anomaly appears in the predictions of the cell velocity.

Flows for which this standard pressure interpolation scheme will not work include flows with large body forces, strongly rotational flows, and high Rayleigh number natural convection. In these cases, it is necessary to compact the cells in the regions of high gradients to resolve the pressure variation adequately.

Another source of error is that FLUENT assumes that the pressure gradient normal to the walls is zero. This is allowable for boundary layers, but not in the presence of body forces or curvatures. Again, the inability to properly account for the wall

pressure gradient is manifested by inward/outward pointing velocity vectors of the walls.

Several alternative methods are available for cases where the standard pressure interpolation scheme is incorrect:

- The linear scheme calculates the pressure on the face as the average of the pressure values in the adjacent cells.
- The second-order scheme reconstructs the pressure on the face in the same way as that used for the second-order convection terms (see spatial discretization section). This scheme can bring some improvement over the standard and linear schemes, but it can have certain disadvantages if it is used at the beginning of a calculation or with a bad mesh. The second-order diagram could not be applied for flows with discontinuous pressure gradients imposed by the presence of a porous medium or by the use of the model VOF or the Mixing Model for Multiphase Flows.
- The body-force-weighted scheme calculates pressure on the face assuming that the normal gradient of the difference between pressure and body forces is constant. This works well if the body forces are known a priori in the momentum equations (e.g. buoyancy, buoyancy and axisymmetric swirl calculations).
- The PRESTO! (PREssure STaggering Option) uses discrete continuity for a "staggered" control volume to calculate the pressure. This procedure is likened in spirit to the staggered-grid schemes used with structured meshes. For triangular, tetrahedral, hybrid and polyhedral, similar accuracy is achieved using similar algorithms. The PRESTO scheme is available for all meshes.

By comparing the different existing methods, we had the choice between the PRESTO scheme and the second-order scheme. We used the second for its lower numerical cost compared to the first scheme.

A.5. DISCRETIZATION OF THE CONTINUITY EQUATION

The continuity equation discretized on the control volume leads to:

$$\sum_{f}^{N_{faces}} J_f \; A_f \; = 0 \qquad (\mathrm{A}.8)$$

where J_f is the mass flux through face f

In order to progress, we need to relate the velocity value on the face, with the velocity values stored in the center of the cell. Linear interpolation of cell-centred velocities results in a non-physical pressure checker-boarding. FLUENT uses a procedure similar to that described by Rhie and Chow (1983) (see ANSYS Fluent user guide to check this reference) to avoid checker-boarding. The velocity value across the face is not linearly averaged; instead, a momentum-weighted average using the weighting factors based on the coefficient a_p from the above equation (equation A.6) is used. Using this procedure J_f is written as the form :

$$J_f = \rho_f \frac{a_{p,co}\ v_{n,co} + a_{p,c1}\, v_{n,c1}}{a_{p,co} + a_{n,c1}}\ d_f\big((p_{c0} + (\nabla p)_{co} .\overrightarrow{r_o}) - (p_{c1} + (\nabla p)_{c1} .\overrightarrow{r_1})\big)$$
$$= \widehat{J_f} + d_f(p_{co} - p_{c1}) \qquad (A.9)$$

Where $p_{c0}, p_{c1}, v_{n,co}, v_{n,c1}$ are the pressures and normal velocities, respectively between the two cells on each side of the face, and $\widehat{J_f}$ contains the velocity influences in these cells (see figure 4.6 in Chapter 4). The term d_f, is a function of $\overline{a_p}$, the average of the coefficients a_p of the momentum equation in the cells on each side of the face f.

A.6. SIMPLE ALGORITHM

The SIMPLE algorithm uses a relationship between velocity and pressure corrections to apply the conservation of mass and obtain the pressure field.

If the momentum equation is solved with an assumed pressure field p^*, the resulting face flux, J_f^*, is calculated from Equation $(A.9)$.

$$J_f^* = \widehat{J_f^*} + d_f(p_{c0}^* - p_{c1}^*) \qquad (A.10)$$

does not satisfy the continuity equation. Therefore, a correction J_f' is added to the face flux J_f^*so that the corrected face flux, J_f

$$J_f = J_f^* + J_f' \qquad (A.11)$$

satisfies the continuity equation. The SIMPLE algorithm postulates that J_f' is written

$$J_f' = d_f(p_{c0}' - p_{c1}') \qquad (A.12)$$

Where p' is the cell pressure correction.

The SIMPLE algorithm substitutes the flow correction equations (Equations $(\mathrm{A}.11)$ and $(\mathrm{A}.12)$) into the discrete continuity equation (Equation $(\mathrm{A}.8)$) to obtain a discrete equation for the pressure correction p' in the cell :

$$a_p\, p' = \sum_{nb} a_{nb}\, p'_{nb} + b \qquad (\mathrm{A}.13)$$

where the source term b is the net flow in the cell:

$$b = \sum_{f}^{N_{faces}} J_f^*\ A_f \qquad (\mathrm{A}.14)$$

The pressure correction equation (Equation$(\mathrm{A}.13)$) can be solved using the Algebraic Multigrid (AMG) method. Once a solution is obtained, the cell pressure and face flux are corrected using

$$p = p^* + \alpha_p p' \qquad (\mathrm{A}.15)$$

$$J_f = J_f^*\ + d_f(p'_{c0} - p'_{c1}) \qquad (\mathrm{A}.16)$$

Here α_p is the under-relaxation factor for pressure (In a simple form, the new value of the variable Φ within a cell depends upon the old value,Φ_{old} , the computed change in Φ , $\Delta\Phi$, and the under-relaxation factor, α, as follows: $\Phi = \Phi_{old} + \alpha\Delta\Phi$). The corrected face flux, J_f, satisfies the discrete continuity equation identically at each iteration.

A.7. PISO SEPARATE ALGORITHM

The PISO pressure-velocity coupling algorithm is from the SIMPLE family. It is based on a high degree of approximation relationship between the pressure and velocity corrections. One of the limitations of the SIMPLE and SIMPLEC algorithms is that the new velocity and the corresponding fluxes do not satisfy the momentum balance after solving the pressure correction equation. Therefore, the calculation should be repeated until the balance is satisfied. To improve the efficiency of this calculation, the PISO algorithm performs two additional rectifications: neighborhood correction and skew correction.

The PISO algorithm takes slightly more CPU time per iteration of the solver, but it can significantly reduce the number of iterations needed for convergence, especially for transient problems. Additionally, PISO skewness correction allows FLUENT to

obtain a solution on a highly skewed mesh in approximately the same number of iterations as required for a more orthogonal mesh.

For meshes with a high degree of asymmetry, the simultaneous coupling of neighbor and asymmetry (skewness) corrections to the same pressure correction equation source can lead to divergence or a lack of robustness. Another, albeit more expensive, method of handling neighborhood and skewness corrections within the PISO algorithm is to apply one or more skewness correction iterations for each distinct neighbor correction iteration. For each individual iteration of the classical PISO algorithm, this technique allows a more precise adjustment of the face mass flux correction according to the normal pressure correction gradient.

Appendix B

C++ scripts

APPENDIX B1 (Boundary Conditions used in Chapter 5) :

Fourier series are used to reproduce the temporal variations of the physiological velocity inlet condition in a waveform as shown in Figure 5.2a (see Chapter 5). To get the harmonics a MATLAB script was used and the results show that 16^{th} harmonics are suitable to fit the physiological waveform. The Fourier series function is then implemented in the processing through a User_Defined_Function (UDF) called DEFINE_PROFILE using C++.

C++ script:

```
#include "udf.h"
DEFINE_PROFILE(unsteady_velocity, thread, position)
{
face_t f;
real t = CURRENT_TIME;
begin_f_loop(f, thread)
{
F_PROFILE(f, thread, position) =((5.84)+(((-1.861724)*cos(2*3.14159*(t+0.01)))+
(2.366494*sin(2*3.14159*(t+0.01)))+( (-0.8464147)*cos(2*3.14159*2*(t+0.01)))+
((-2.597306)*sin(2*3.14159*2*(t+0.01)))+( 2.261833*cos(2*3.14159*(t+0.01)*3))+
(0.5455418*sin(2*3.14159*(t+0.01)*3))+
( (-0.8357277)*cos(2*3.14159*(t+0.01)*4))+
(0.7784028*sin(2*3.14159*(t+0.01)*4))+
( (-0.6328353)*cos(2*3.14159*(t+0.01)*5))+
((-0.2359725)*sin(2*3.14159*(t+0.01)*5))+
( 0.4011518*cos(2*3.14159*(t+0.01)*6))+
((-0.5395101)*sin(2*3.14159*(t+0.01)*6))+
( 0.4362277*cos(2*3.14159*(t+0.01)*7))+
(0.6074085*sin(2*3.14159*(t+0.01)*7))+
( (-0.5395451)*cos(2*3.14159*(t+0.01)*8))+
(-6.0490195e-02*sin(2*3.14159*(t+0.01)*8))+
( 2.2358865e-02*cos(2*3.14159*(t+0.01)*9))+
((-0.2770012)*sin(2*3.14159*(t+0.01)*9))+
( 0.2721851*cos(2*3.14159*(t+0.01)*10))+
(1.3501522e-02*sin(2*3.14159*(t+0.01)*10))+
( (-0.1614565)*cos(2*3.14159*(t+0.01)*11))+
(0.3356538*sin(2*3.14159*(t+0.01)*11))+
( -9.0932406e-02*cos(2*3.14159*(t+0.01)*12))+
((-0.3159903)*sin(2*3.14159*(t+0.01)*12))+
```

```
( 0.2058507*cos(2*3.14159*(t+0.01)*13))+
(3.2725684e-02*sin(2*3.14159*(t+0.01)*13))+
( -3.6538206e-02*cos(2*3.14159*(t+0.01)*14))+
(0.1096759*sin(2*3.14159*(t+0.01)*14))+
( (-0.1185898)*cos(2*3.14159*(t+0.01)*15))+
(-3.9283533e-02*sin(2*3.14159*(t+0.01)*15))+
( 0.1185699*cos(2*3.14159*(t+0.01)*16))+
(-5.6332495e-02*sin(2*3.14159*(t+0.01)*16)))/0.485)*0.01 ;
}
end_f_loop(f, thread)
}
```

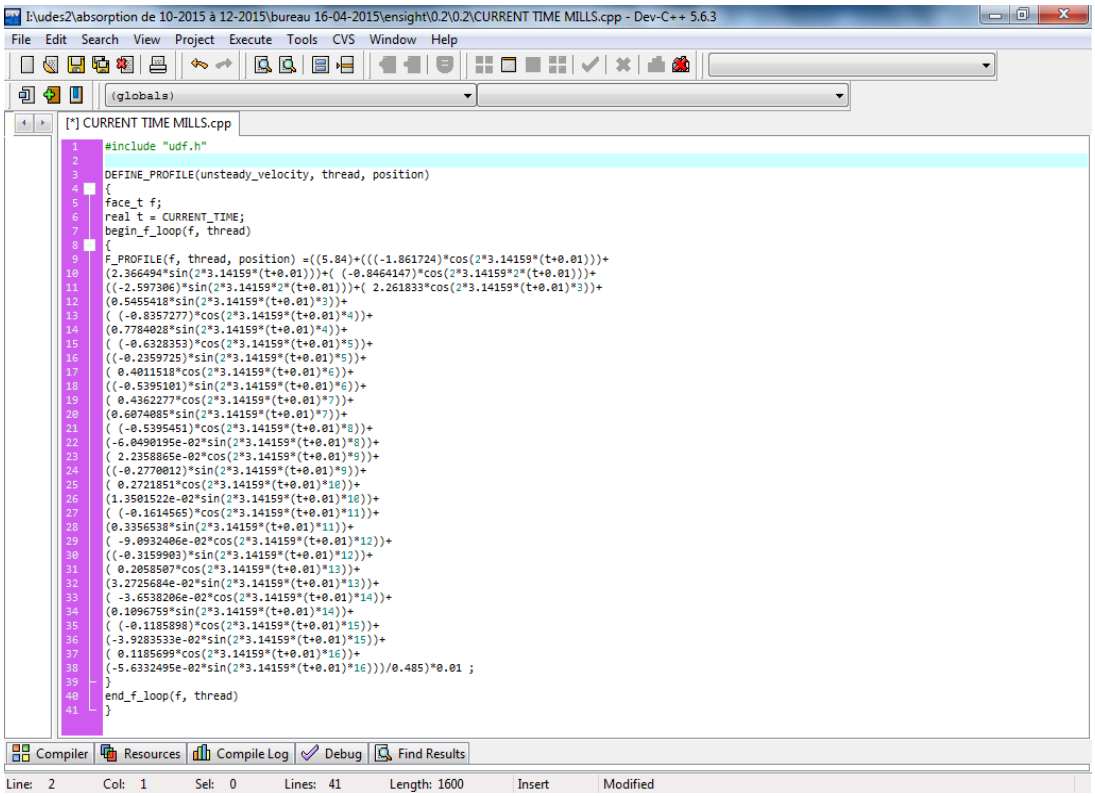

Figure B.1.1: C++ script used to have the inlet boundary condition used in Chapter5 (see Figure 5.2.a).

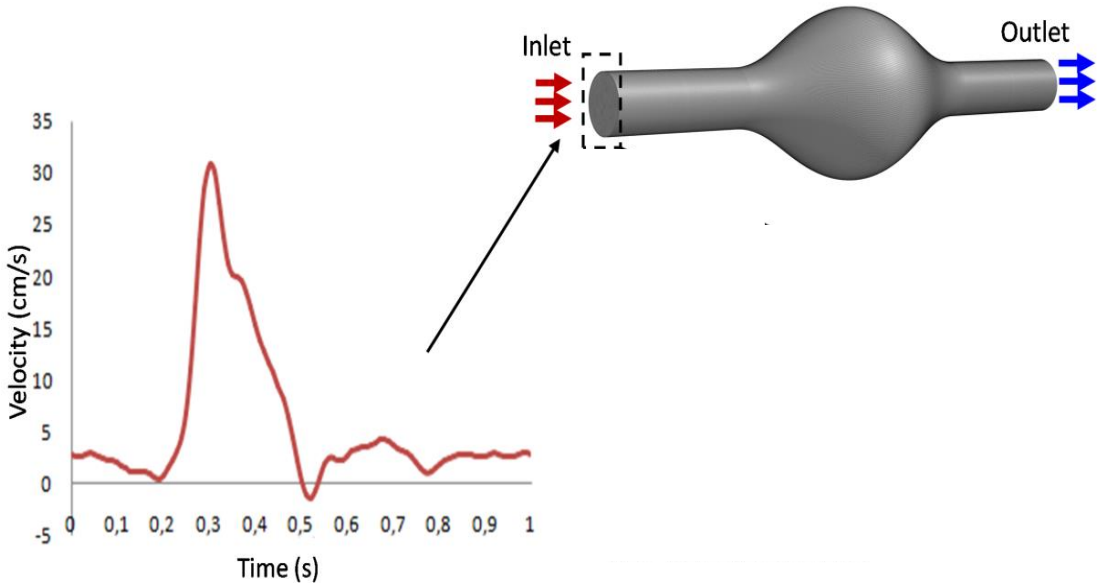

Figure B.1.2: waveform reproduced by Fourier series and implemented as velocity inlet boundary condition using the UDF in ANSYS Fluent (see Figure B.1.1).

REMARK:

A similar methodology is followed to reproduce the inlet velocity boundary condition for Chapter 6. As it was mentioned in this chapter, PC-MRI-based volumetric flow at the infrarenal artery [156] is converted to a corresponding velocity inlet waveform for each patient (an example is shown for Patient 1 in Figure 6.3). Where similarly to the example shown earlier (Figs B.1.1 & B.1.2) to get the harmonics a MATLAB script was used and a Fourier series function, then this function is implemented in the processing through a User_Defined_Function (UDF) called DEFINE_PROFILE using C++ for each patient.

APPENDIX B2 (Boundary Conditions used in Chapter 7 –Inlet-)

C++ Script

Here we show some parts of the C++ script used to reproduce the in-vivo velocity profile extracted from 4D flow MRI data used in Chapter 7. Here we are limited to showing the velocity function in the x direction (Vx). As it could be seen in the following figure the script contains 708 lines with more than 6.10^6 in length (see red squares).

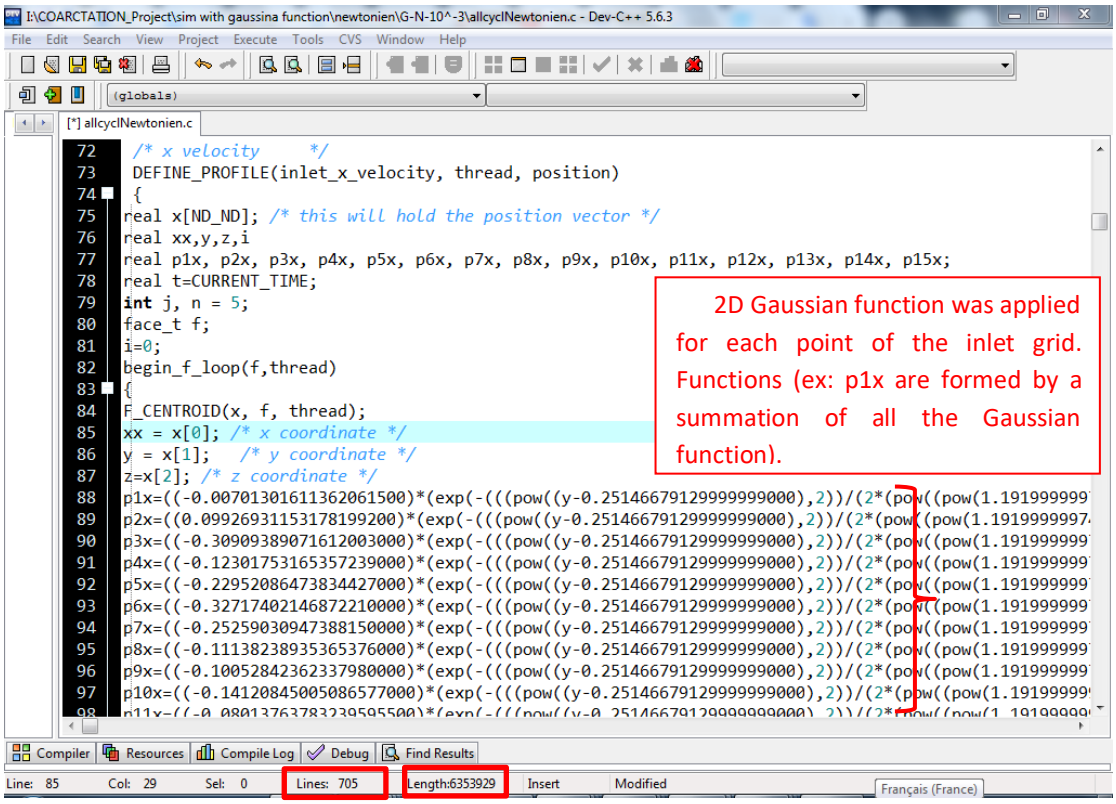

a)

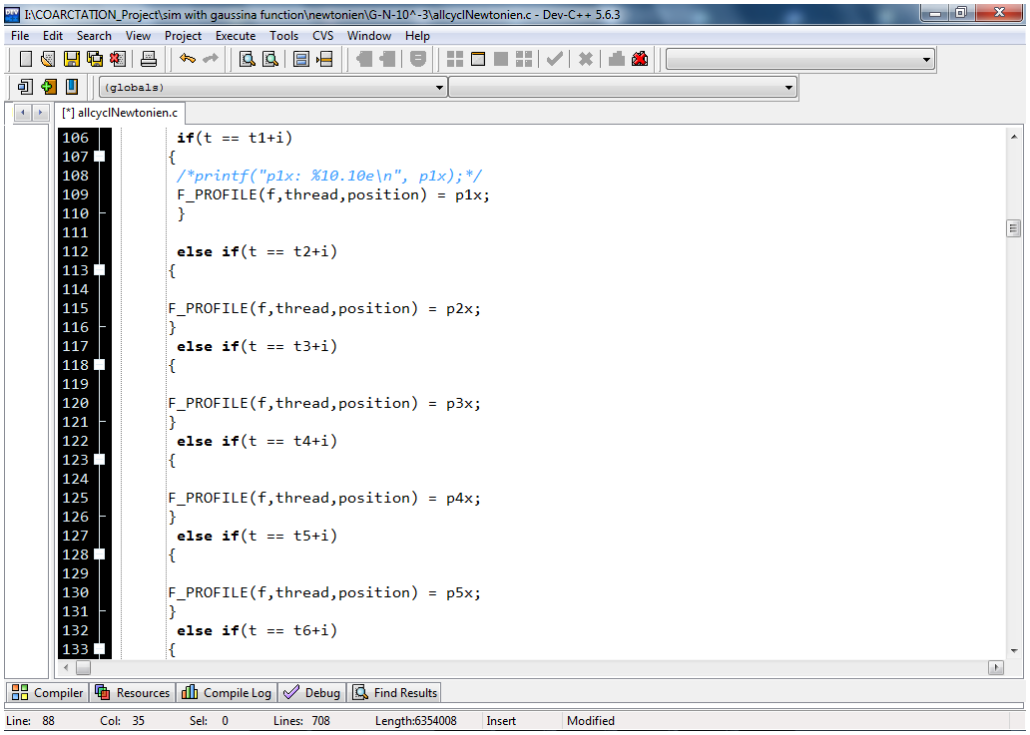

b)

Figure B.2.1: Part of C++ script used to reproduce the real inlet velocity profile used as an inlet boundary condition in Chapter 7. (Gaussian function in the time frame of the cycle where in-vivo data are provided -see Chapter 7 section 7.2.6-).

Interpolation part:

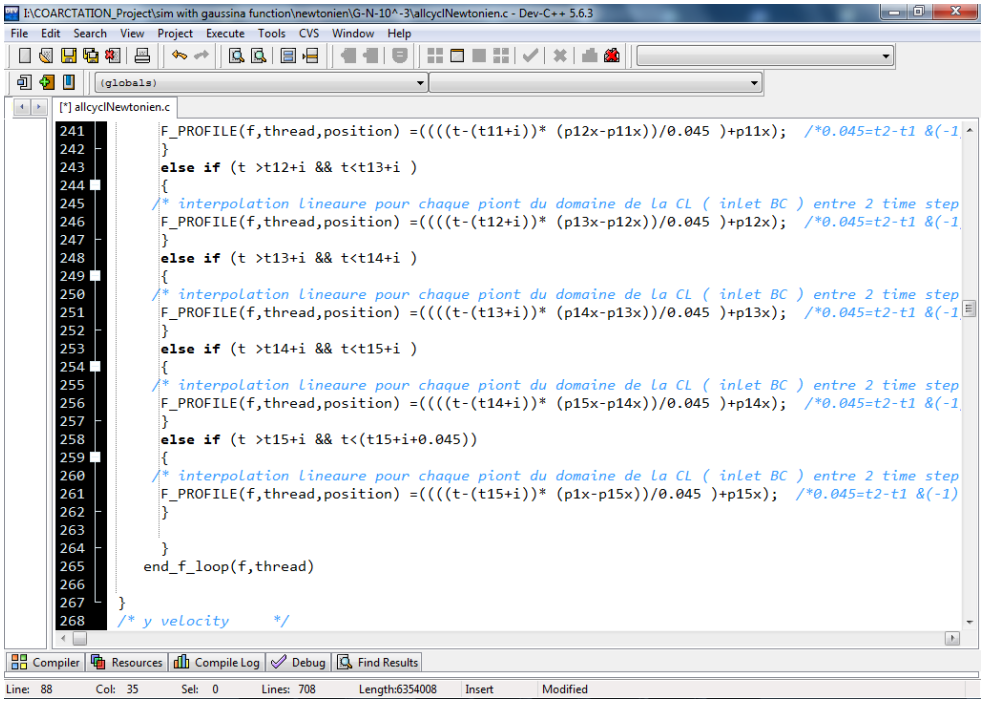

Figure B.2.2: Part of C++ script where the interpolation is applied, in time steps between the time frames provided by *in-vivo* data.

This part of the algorithm allows the implementation of the boundary condition in the following format (see Figure B.2.3 for more details check Chapter 7 section 7.2.6 and Figures 7.5 to 7.8).

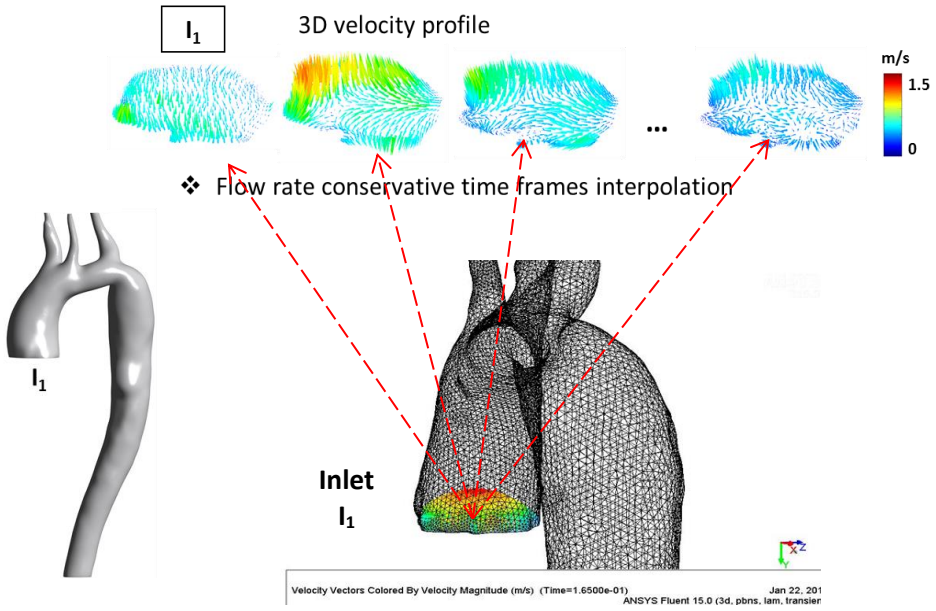

Figure B.2.3: 4D Flow-based boundary conditions used with Inlet 3D velocity profiles obtained after flow-rate conservative temporal interpolation and implemented in the processing through a User_Defined_Function (UDF).

APPENDIX B3: (Boundary Conditions used in Chapter 7 –Outlets at the three supra-aortic branches -)

A similar methodology as in Appendix B1 was used in this part of the script; here we used the Fourier series to reproduce the in-vivo velocity at the three supra-aortic branches.

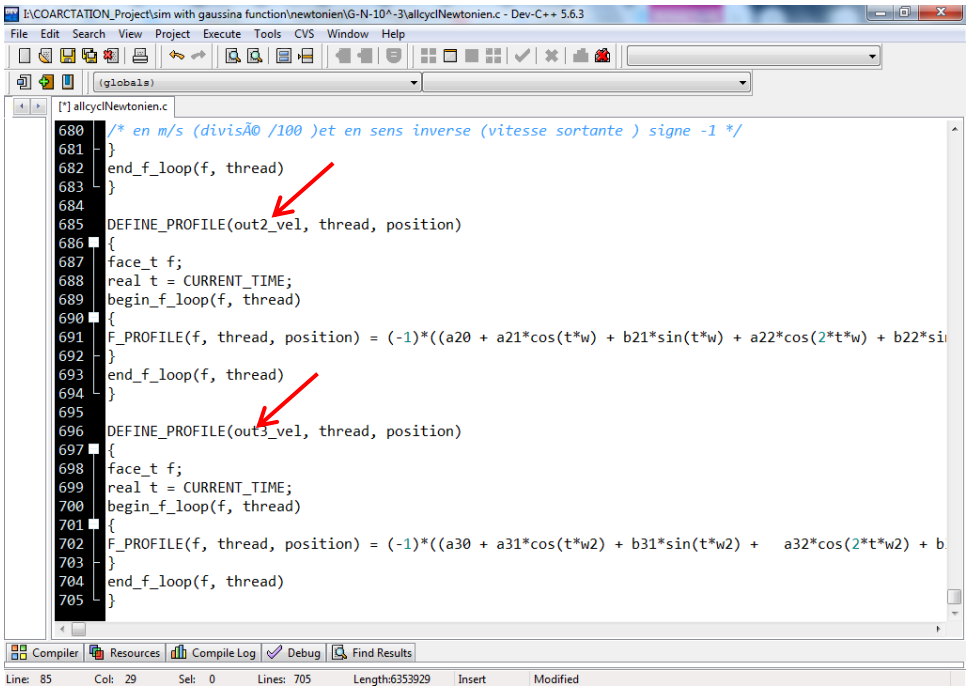

Figure B.3.1: The Velocity boundary conditions used in the supra-aortic branches.

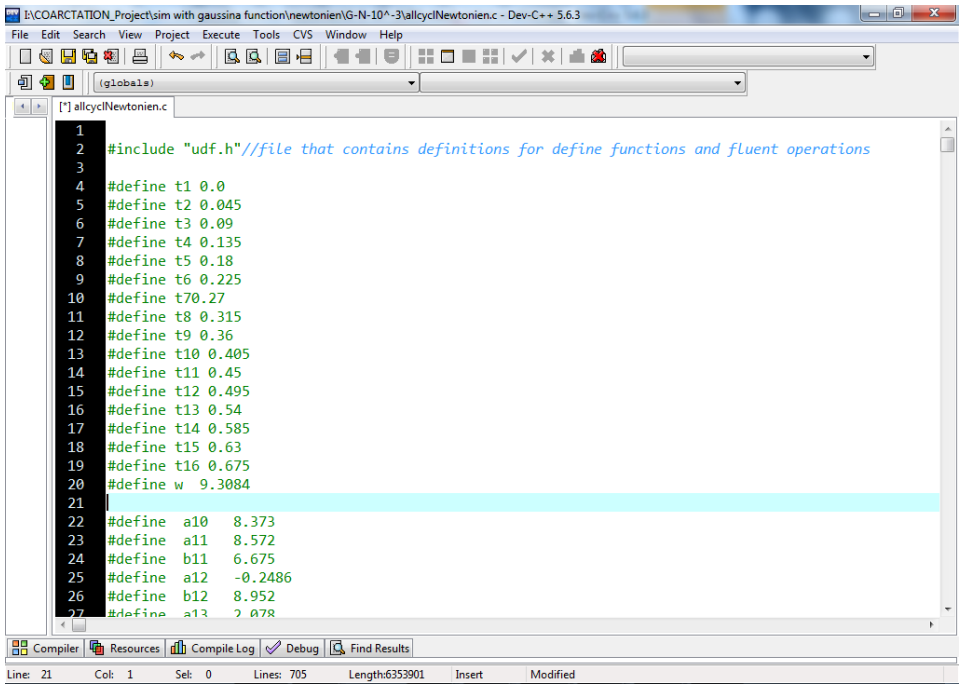

Figure B.3.2: Part of the C++ script where the harmonics values are defined (at the beginning of the script).

This part of the algorithm allows the implementation of the boundary condition in the following format (see Figure B.3.3).

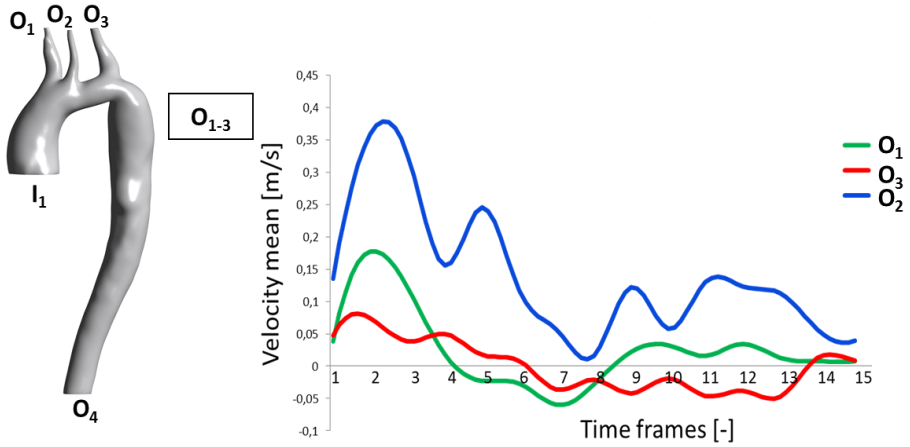

Figure B.3.3: Boundary condition (Velocity waveform) applied at the three supra aortic branches O1 O2 and O3 , while zero-pressure in the descending aorta is applied.

REMARK:

We didn't show all the C++ scripts in this part of the thesis. Also, it should be noticed that for each C++ script, multiple MATLAB scripts are developed as mentioned in the flowcharts showing the methodology adopted in Chapters 5, 6 and 7 (see respectively Figures 4.2, 4.3 and 4.3 in Chapter 4). All the developed materials are available under request.

Appendix C

Ethical approval statement

SARL CENTRE D'IMAGERIE MEDICALE MAHDI
Cité AMMARA 2, Ilot 105, section 04, Chéraga – Alger
Tel : 0 23.39.55.26/54.93 Fax : 023.39.54.81
Email : contact@cimcheraga.com
RC : 16/00-1008348 B 14
NIF : 001416100834889
Art : 16520626592
Compte Al Salam Bank RIB : 03801601000801000173

Ethical approval statement :

Date : 14/11/2021
Name : Djelloul Belkacemi
University : Hassiba ben Bouali university of Chlef
Number: 00064

Computed tomography CT-scan data of three patients presenting with Abdominal Aortic Aneurysm were used after ethical approval by our institution. The scans' data were acquired between the 3rd and 17th of February, 2021.
Patients' details :

Patient	*Age (years)*	*Gender M/F*
Patient 1	*70*	*M*
Patient 2	*76*	*M*
Patient 3	*60*	*M*

Cité Ammara 02, Ilot 105, Section 4, Chéraga- Alger Tel : 0 23.39.55.26/54.93 Tel/Fax : 023.39.54.81
Email : contact@cimcheraga.com

BIBLIOGRAPHY

[1] Baptista, E.A., Queiroz, B.L. Spatial analysis of cardiovascular mortality and associated factors around the world. BMC Public Health 22, 1556 (2022). https://doi.org/10.1186/s12889-022-13955-7

[2] G.A. Roth, G.A. Mensah, C.O. Johnson, G. Addolorato, E. Ammirati, L.M. Baddour, ... & GBD-NHLBI-JACC Global Burden of Cardiovascular Diseases Writing Group. (2020). Global burden of cardiovascular diseases and risk factors, 1990–2019: update from the GBD 2019 study. Journal of the American College of Cardiology, 76(25), 2982-3021.
https://doi.org/10.1016/j.jacc.2020.11.010

[3] B.J. Doyle, A. Callanan, P.E. Burke, P.A. Grace, M.T. Walsh, D.A. Vorp, & T.M. McGloughlin, (2009).Vessel asymmetry as an additional diagnostic tool in the assessment of abdominal aortic aneurysms. Journal of Vascular Surgery, 49(2), 443-454. https://doi.org/10.1016/j.jvs.2008.08.064

[4] Salsac, Anne-Virginie, Steven R. Sparks, and Juan C. Lasheras. "Hemodynamic Changes Occurring during the Progressive Enlargement of Abdominal Aortic Aneurysms." Annals of Vascular Surgery 18, no. 1 (January 2004): 14–21. https://doi.org/10.1007/s10016-003-0101-3.

[5] Peattie, Robert A., Tiffany J. Riehle, and Edward I. Bluth. "Pulsatile Flow in Fusiform Models of Abdominal Aortic Aneurysms: Flow Fields, Velocity Patterns and Flow-Induced Wall Stresses." Journal of Biomechanical Engineering 126, no. 4 (August 1, 2004): 438–46.
https://doi.org/10.1115/1.1784478.

[6] Scotti CM, Shkolnik AD, Muluk SC, Finol EA. Fluid-structure interaction in abdominal aortic aneurysms: Effects of asymmetry and wall thickness. Biomed Eng Online. 2005;4.

[7] Fraser KH, Li MX, Lee WT, Easson WJ, Hoskins PR. Fluid-structure interaction in axially symmetric models of abdominal aortic aneurysms. Proc Inst Mech Eng H J Eng Med. 2009;223(2):195-209.

[8] Wang X, Li X. A fluid-structure interaction-based numerical investigation on the evolution of stress, strength and rupture potential of an abdominal aortic aneurysm. Comput Methods Biomech Biomed Engin. 2013;16(9):1032-9.

[9] Deplano, Valérie, Clark Meyer, Carine Guivier-Curien, and Eric Bertrand. "New Insights into the Understanding of Flow Dynamics in an in Vitro Model for Abdominal Aortic Aneurysms." Medical Engineering & Physics 35, no. 6 (June 1, 2013): 800–809.
https://doi.org/10.1016/j.medengphy.2012.08.010.

[10] Javadzadegan, A., Simmons, A., Behnia, M., & Barber, T. (2017). Computational modelling of abdominal aortic aneurysms: effect of suprarenal vs infrarenal positions. European Journal of Mechanics-B/Fluids, 61, 112-124.

[11] Drewe, Corey J., Louis P. Parker, Lachlan J. Kelsey, Paul E. Norman, Janet T. Powell, and Barry J. Doyle. "Haemodynamics and Stresses in Abdominal Aortic Aneurysms: A Fluid-Structure Interaction Study into the Effect of Proximal Neck and Iliac Bifurcation Angle." Journal of Biomechanics 60 (July 2017): 150–56. https://doi.org/10.1016/j.jbiomech.2017.06.029.

[12] Jafarzadeh, Sina, Arsalan Nasiri Sadr, Ehsan Kaffash, Sahar Goudarzi, Ehsan Golab, and Arash Karimipour. "The Effect of Hematocrit and Nanoparticles Diameter on Hemodynamic Parameters and Drug Delivery in Abdominal Aortic Aneurysm with Consideration of Blood Pulsatile Flow." Computer Methods and Programs in Biomedicine 195 (October 1, 2020): 105545.
https://doi.org/10.1016/j.cmpb.2020.105545.

[13] Philip, Nimmy Thankom, B. S. V. Patnaik, and B. J. Sudhir. “Hemodynamic Simulation of Abdominal Aortic Aneurysm on Idealised Models: Investigation of Stress Parameters during Disease Progression.” Computer Methods and Programs in Biomedicine 213 (January 1, 2022): 106508. https://doi.org/10.1016/j.cmpb.2021.106508.

[14] Di Achille, P., G. Tellides, C. A. Figueroa, and J. D. Humphrey. “A Haemodynamic Predictor of Intraluminal Thrombus Formation in Abdominal Aortic Aneurysms.” Proceedings of the Royal Society A: Mathematical, Physical and Engineering Sciences 470, no. 2172 (December 8, 2014): 20140163. https://doi.org/10.1098/rspa.2014.0163.

[15] Seman, Che Mohammad Hafizal Muzammil Che, Nur Ayuni Marzuki, Nofrizalidris Darlis, Noraini Marsi, Zuliazura Mohd Salleh, Izuan Amin Ishak, Ishkrizat Taib, and Safra Liyana Sukiman. "Comparison of Hemodynamic Performances Between Commercial Available Stents Design on Stenosed Femoropopliteal Artery." CFD Letters 12, no. 7 (2020): 17-25. https://doi.org/10.37934/cfdl.12.7.1725.

[16] Finol EA, Amon CH. Flow dynamics in anatomical models of abdominal aortic aneurysms: Computational analysis of pulsatile flow. Acta Cientifica Venezolana. 2003;54(1):43-9.

[17] Finol EA, Keyhani K, Amon CH. The effect of asymmetry in abdominal aortic aneurysms under physiologically realistic pulsatile flow conditions. J Biomech Eng. 2003;125(2):207-17.

[18] Khanafer KM, Bull JL, Upchurch GR, Berguer R. Turbulence significantly increases pressure and fluid shear stress in an aortic aneurysm model under resting and exercise flow conditions. Ann Vasc Surg. 2007 2007/01/01/;21(1):67-74.

[19] O'Rourke MJ, McCullough JP. A comparison of the measured and predicted flow field in a patient-specific model of an abdominal aortic aneurysm. Proc Inst Mech Eng H J Eng Med. 2008;222(5):737-50.

[20] Otsuki, Y., Minh, N. B., Ohtake, H., Watanabe, G., & Matsuzawa, T. (2013). Research Article Preliminary Computational Hemodynamics Study of Double Aortic Aneurysms under Multistage Surgical Procedures: An Idealised Model Study.

[21] Vinoth R, Kumar D, Adhikari R, Devaprasad D, Kaliyamoorthy D. Computational investigation of blood flow in fusiform models of aortic aneurysms: A steady state analysis. Int J Biomed Eng Technol. 2015;19(1):70-91.

[22] Wang X, Li X. Computational simulation of aortic aneurysm using FSI method: Influence of blood viscosity on aneurismal dynamic behaviors. Comput Biol Med. 2011;41(9):812-21.

[23] Arzani A, Les AS, Dalman RL, Shadden SC. Effect of exercise on patient specific abdominal aortic aneurysm flow topology and mixing. Int J Numer Methods Biomed Eng. 2014;30(2):280-95.

[24] Arzani A, Suh G-Y, Dalman RL, Shadden SC. A longitudinal comparison of hemodynamics and intraluminal thrombus deposition in abdominal aortic aneurysms. Am J Physiol Heart Circ Physiol. 2014;307(12):H1786-H95.

[25] Suh GY, Les AS, Tenforde AS, Shadden SC, Spilker RL, Yeung JJ, et al. Quantification of particle residence time in abdominal aortic aneurysms using magnetic resonance imaging and computational fluid dynamics. Ann Biomed Eng. 2011;39(2):864-83.

[26] Suh GY, Les AS, Tenforde AS, Shadden SC, Spilker RL, Yeung JJ, et al. Hemodynamic changes quantified in abdominal aortic aneurysms with increasing exercise intensity using MR exercise imaging and image-based computational fluid dynamics. Ann Biomed Eng. 2011;39(8):2186-202.

[27] Les AS, Shadden SC, Figueroa CA, Park JM, Tedesco MM, Herfkens RJ, et al. Quantification of hemodynamics in abdominal aortic aneurysms during rest and exercise using magnetic resonance imaging and computational fluid dynamics. Ann Biomed Eng. 2010;38(4):1288-313.

[28] Kung EO, Les AS, Medina F, Wicker RB, McConnell MV, Taylor CA. In vitro validation of finite-element model of AAA hemodynamics incorporating realistic outlet boundary conditions. J Biomech Eng. 2011;133(4):041003-.

[29] Doyle BJ, McGloughlin TM, Kavanagh EG, Hoskins PR. From detection to rupture: a serial computational fluid dynamics case study of a rapidly expanding, patient-specific, ruptured abdominal aortic aneurysm. Doyle B, Miller K, Wittek A, Nielsen PMF, editors. New York, NY: Springer New York; 2014 2014//. 53-68 p.

[30] Chen, C. Y., Antón, R., Hung, M. Y., Menon, P., Finol, E. A., & Pekkan, K. (2014). Effects of intraluminal thrombus on patient-specific abdominal aortic aneurysm hemodynamics via stereoscopic particle image velocity and computational fluid dynamics modeling. Journal of biomechanical engineering, 136(3). https://doi.org/10.1115/1.4026160

[31] Boutsianis E, Guala M, Olgac U, Wildermuth S, Hoyer K, Ventikos Y, et al. CFD and PTV steady flow investigation in an anatomically accurate abdominal aortic aneurysm. J Biomech Eng. 2009;131(1).

[32] Lozowy RJ, Kuhn DCS, Ducas AA, Boyd AJ. The relationship between pulsatile flow impingement and intraluminal thrombus deposition in abdominal aortic aneurysms. Cardiovasc Eng Technol. 2017 2017//;8(1):57-69.

[33] Arzani A, Shadden SC. Characterizations and correlations of wall shear stress in aneurysmal flow. J Biomech Eng. 2016;138(1):0145031-01450310. PubMed PMID: PMC4844249.

[34] Filardi V. CFD analysis to evaluate hemodynamic parameters in a growing abdominal aortic aneurysm. Vasc Dis Manage. 2015;12(5):84-95.

[35] Hansen KB, Arzani A, Shadden SC. Mechanical platelet activation potential in abdominal aortic aneurysms. J Biomech Eng. 2015;137(4).

[36] Ene F, Delassus P, Morris L. The influence of computational assumptions 662 on analyzing abdominal aortic aneurysm haemodynamics. Proc Inst Mech Eng H J Eng Med. 2014;228(8):768-80.

[37] Chandra S, Raut SS, Jana A, Biederman RW, Doyle M, Muluk SC, et al. Fluid-structure interaction modeling of abdominal aortic aneurysms: The impact of patient-specific inflow conditions and fluid/solid coupling. J Biomech Eng. 2013;135(8).

[38] Soudah E, Ng EYK, Loong TH, Bordone M, Pua U, Narayanan S. CFD modelling of abdominal aortic aneurysm on hemodynamic loads using a realistic geometry with CT. Comp Math Methods Med. 2013;2013.

[39] Hardman D, Doyle BJ, Semple SI, Richards JM, Newby DE, Easson WJ, et al. On the prediction of monocyte deposition in abdominal aortic aneurysms using computational fluid dynamics. Proc Inst Mech Eng H J Eng Med. 2013;227(10):1114-24.

[40] O'Rourke MJ, McCullough JP, Kelly S. An investigation of the relationship between hemodynamics and thrombus deposition within patient-specific models of abdominal aortic aneurysm. Proc Inst Mech Eng H J Eng Med. 2012;226(7):548-64.

[41] Hardman D, Semple SI, Richards JM, Hoskins PR. Comparison of patient-specific inlet boundary conditions in the numerical modelling of blood flow in abdominal aortic aneurysm disease. Int J Numer Methods Biomed Eng. 2013;29(2):165-78. https://doi.org/10.1002/cnm.2535

[42] Shabestari RM, Hassani K, Izadi F. Modeling of abdominal aorta aneurysm and study of the pathology using computational fluid dynamics method. Biomed Eng Appl Basis Commun. 2011;23(4):295-305.

[43] Biasetti J, Gasser TC, Auer M, Hedin U, Labruto F. Hemodynamics of the normal aorta compared to fusiform and saccular abdominal aortic aneurysms with emphasis on a potential thrombus formation mechanism. Ann Biomed Eng. 2010;38(2):380-90.

[44] Di Martino ES, Guadagni G, Fumero A, Ballerini G, Spirito R, Biglioli P, et al. Fluid structure interaction within realistic three-dimensional models of the aneurysmatic aorta as a guidance to assess the risk of rupture of the aneurysm. Med Eng Phys. 2001;23(9):647-

[45] Poelma C, Watton PN, Ventikos Y. Transitional flow in aneurysms and the computation of haemodynamic parameters. J R Soc Interface. 2015;12(105).

[46] Piccinelli M, Vergara C, Antiga L, Forzenigo L, Biondetti P, Domanin M. Impact of hemodynamics on lumen boundary displacements in abdominal aortic aneurysms by means of dynamic computed tomography and computational fluid dynamics. Biomech Model Mechanobiol. 2013 2013//;12(6):1263-76.

[47] Veshkina N, Zbicinski I, Stefańczyk L. 2D FSI determination of mechanical stresses on aneurismal walls. Bio-Med Mater Eng. 2014;24(6):2519-26.

[48] Wolters BJBM, Rutten MCM, Schurink GWH, Kose U, De Hart J, Van De Vosse FN. A patient-specific computational model of fluid-structure interaction in abdominal aortic aneurysms. Med Eng Phys. 2005;27(10):871-83.

[49] Borghi A, Wood NB, Mohiaddin RH, Xu XY. Fluid–solid interaction simulation of flow and stress pattern in thoracoabdominal aneurysms: A patient-specific study. J Fluid Struct. 2008 2//;24(2):270-80.

[50] Bluestein D, Dumont K, De Beule M, Ricotta J, Impellizzeri P, Verhegghe B, et al. Intraluminal thrombus and risk of rupture in patient specific abdominal aortic aneurysm– FSI modelling. Comput Methods Biomech Biomed Engin. 2009;12(1):73-81.

[51] Scotti CM, Jimenez J, Muluk SC, Finol EA. Wall stress and flow dynamics in abdominal aortic aneurysms: Finite element analysis vs. fluid-structure interaction. Comput Methods Biomech Biomed Engin. 2008;11(3):301-22.

[52] Kelly S, O'Rourke M. Fluid, solid and fluid-structure interaction simulations on patient635 based abdominal aortic aneurysm models. Proc Inst Mech Eng H J Eng Med. 2012;226(4):288-304.

[53] Lin S, Han X, Bi Y, Ju S, Gu L. Fluid-structure interaction in abdominal aortic aneurysm: effect of modeling techniques. Biomed Res Int. 2017;2017:10.

[54] Macek Jilkova, Z., Deplano, V., Verdier, C., Toungara, M., Geindreau, C., & Duperray, A. (2013). Wall shear stress and endothelial cells dysfunction in the context of abdominal aortic aneurysms. Computer Methods in Biomechanics and Biomedical Engineering, 16(sup1), 27-29. https://doi.org/10.1080/10255842.2013.815959

[55] Dalman, R. L., Tedesco, M. M., Myers, J., & Taylor, C. A. (2006). AAA disease: mechanism, stratification, and treatment. Annals of the New York Academy of Sciences, 1085(1), 92-109.

[56] Wan Ab Naim, W. N., Ganesan, P. B., Sun, Z., Chee, K. H., Hashim, S. A., & Lim, E. (2014). A perspective review on numerical simulations of hemodynamics in aortic dissection. The Scientific World Journal, 2014. https://doi.org/10.1155/2014/652520

[57] Ziegler, M., Welander, M., Lantz, J., Lindenberger, M., Bjarnegård, N., Karlsson, M., ... & Dyverfeldt, P. (2019). Visualizing and quantifying flow stasis in abdominal aortic aneurysms in men using 4D flow MRI. Magnetic Resonance Imaging, 57, 103-110. https://doi.org/10.1016/j.mri.2018.11.003

[58] Wang, Y., Joannic, D., Patrick, J., Keromnes, A., Aurélien, M., Lalande, A., & Fontaine, J. F. (2016). Comparison of Flow Measurement by 4D Flow Magnetic Resonance Imaging and by Particles Image Velocimetry on Phantom of Abdominal Aortic Aneurysm. SM Vascular medecine.

[59] Hardman, D., Doyle, B. J., Semple, S. I., Richards, J. M., Newby, D. E., Easson, W. J., & Hoskins, P. R. (2013). On the prediction of monocyte deposition in abdominal aortic aneurysms using computational fluid dynamics. Proceedings of the Institution of Mechanical Engineers, Part H: Journal of Engineering in Medicine, 227(10), 1114-1124. https://doi.org/10.1177/0954411913494

[60] Kung, E. O., Les, A. S., Medina, F., Wicker, R. B., McConnell, M. V., & Taylor, C. A. (2011). In vitro validation of finite-element model of AAA hemodynamics incorporating realistic outlet boundary conditions. Journal of biomechanical engineering, 133(4).
https://doi.org/10.1115/1.4003526

[61] Habibi, M., Dawson, S. T., & Arzani, A. (2020). Data-driven pulsatile blood flow physics with dynamic mode decomposition. Fluids, 5(3), 111. https://doi.org/10.3390/biology10030185

[62] Piatti, F., Belkacemi, D., Caimi, A., Sturla, F., Greiser, A., Pluchinotta, F., & Redaelli, A. (2017, September). On the potential of 4D Flow in guiding CFD analyses: a case study of aortic coartaction. In Proceedings VII Meeting Italian Chapter of the European Society of Biomechanics (ESB-ITA 2017) (pp. 28-29).

[63] Arzani, A., Wang, J. X., & D'Souza, R. M. (2021). Uncovering near-wall blood flow from sparse data with physics-informed neural networks. Physics of Fluids, 33(7), 071905.
https://doi.org/10.1063/5.0055600

[64] Malek, A.M., Alper, S.L., & Izumo, S. (1999). Hemodynamic shear stress and its role in atherosclerosis. Jama, 282(21), 2035-2042. https://doi.org/10.1001/jama.282.21.2035

[65] Boyd A.J., Kuhn D.C., Lozowy R.J., & Kulbisky G.P., (2016). Low wall shear stress predominates at sites of abdominal aortic aneurysm rupture. Journal of vascular surgery, 63(6), 1613-1619. https://doi.org/10.1016/j.jvs.2015.01.040

[66] Tzirakis, K., Kamarianakis, Y., Metaxa, E., Kontopodis, N., Ioannou, C. V., & Papaharilaou, Y. (2017). A robust approach for exploring hemodynamics and thrombus growth associations in abdominal aortic aneurysms. Medical & Biological Engineering & Computing, 55(8), 1493-1506.
https://doi.org/10.1007/s11517-016-1610-x

[67] Zambrano, B. A., Gharahi, H., Lim, C. Y., Lee, W., & Baek, S. (2022). Association of vortical structures and hemodynamic parameters for regional thrombus accumulation in abdominal aortic aneurysms. International Journal for Numerical Methods in Biomedical Engineering, 38(2), e3555. https://doi.org/10.1002/cnm.3555

[68] Colciago, C. M., Deparis, S., Domanin, M., Riccobene, C., Schenone, E., & Quarteroni, A. (2020). Analysis of morphological and hemodynamical indexes in abdominal aortic aneurysms as preliminary indicators of intraluminal thrombus deposition. Biomechanics and Modeling in Mechanobiology, 19(3), 1035-1053. https://doi.org/10.1007/s10237-019-01269-4

[69] Zambrano, B.A., Gharahi, H., Lim, C., Jaberi, F.A., Choi, J., Lee, W., & Baek, S. (2016). Association of intraluminal thrombus, hemodynamic forces, and abdominal aortic aneurysm expansion using

longitudinal CT images. Annals of biomedical engineering, 44(5), 1502-1514. https://doi.org/10.1007/s10439-015-1461-x

[70] Qiu, Y., Wang, Y., Fan, Y., Peng, L., Liu, R., Zhao, J., ... & Zheng, T. (2019). Role of intraluminal thrombus in abdominal aortic aneurysm ruptures: a hemodynamic point of view. Medical Physics, 46(9), 4263-4275. https://doi.org/10.1002/mp.13658

[71] Forneris, A., Marotti, F. B., Satriano, A., Moore, R. D., & Di Martino, E. S. (2020). A novel combined fluid dynamic and strain analysis approach identified abdominal aortic aneurysm rupture. Journal of Vascular Surgery Cases, Innovations and Techniques, 6(2), 172-176. https://doi.org/10.1016/j.jvscit.2020.01.014

[72]https://www.aps.dz/sante-science-technologie/119636-les-maladies-cardiovasculaires-premiere-cause-de-mortalite-en-algerie#:~:text=%22Les%20maladies%20cardiovasculaires%20sont%20la,du%20Groupe%20H%C3%B4tellerie%2C%20Tourisme%20et. Website accessed on 27-07-2022

[73] Survey of INSP 2016 (Institut National De La Santé Publique).

[74]: Human Physiology From Cells to Systems: Lauralee Sherwood seventh edition Department of Physiology and Pharmacology School of Medicine West Virginia University-USA- Brooks/Cole, Cengage Learning ISBN-10: 0-495-39184-0 (2010)

[75] https://my.clevelandclinic.org/

[76] Hutchison, S. J. (2008). Aortic Diseases E-Book: Clinical Diagnostic Imaging Atlas. Elsevier Health Sciences. ISBN: 978-1-4160-5270-8 ,by Saunders Elsevier, Philadelphia USA.

[77] https://www.healthdirect.gov.au/aortic-aneurysm . Website accessed on 28-07-2022

[78] M. Abbasi, A. N. Esfahani, E. Golab, O. Golestanian, N. Ashouri, S.M. Sajadi, ... & A. Karimipour, (2021). Effects of Brownian motions and thermophoresis diffusions on the hematocrit and LDL concentration/diameter of pulsatile non-Newtonian blood in abdominal aortic aneurysm. Journal of Non-Newtonian Fluid Mechanics, 294, 104576. https://doi.org/10.1016/j.jnnfm.2021.104576

[79] B.W. Ullery, R.L. Hallett, & D. Fleischmann, (2018). Epidemiology and contemporary management of abdominal aortic aneurysms. Abdominal Radiology, 43(5), 1032-1043. https://doi.org/10.1007/s00261-017-1450-7

[80] A. Wanhainen, F. Verzini, I. Van Herzeele, E. Allaire, M. Bown, T. Cohnert, ... & H. Verhagen, (2019). Clinical practice guidelines on the management of abdominal aorto-iliac artery aneurysms. Eur J Vasc Endovasc Surg, 57(1), 8-93. https://doi.org/10.1016/j.ejvs.2018.09.020

[81] P.A. Cosford, G.C. Leng, & J. Thomas, (2007). Screening for abdominal aortic aneurysm. The Cochrane Library. https://doi.org/10.1002/14651858.CD002945.pub2

[82] Kavanagh, E. G., Grace, P. A., McGloughlin, T. M., & Doyle, B. J. (2014). The biaxial mechanical behaviour of abdominal aortic aneurysm intraluminal thrombus: classification of morphology and the determination of layer and region specific properties. Journal of biomechanics, 47(6), 1430-1437.

[83] da Silva, E. S., Rodrigues, A. J., de Tolosa, E. M. C., Rodrigues, C. J., do Prado, G. V. B., & Nakamoto, J. C. (2000). Morphology and diameter of infrarenal aortic aneurysms: a prospective autopsy study. Cardiovascular surgery, 8(7), 526-532.

[84] Gasser, T.C.; Görgülü, G.; Folkesson, M.; Swedenborg, J. Failure properties of intraluminal thrombus in abdominal aortic aneurysm under static and pulsating mechanical loads. J. Vasc. Surg. 2008, 48, 179–188

[85] Cardiology Essentials in Clinical Practice, Gabriel A. Adelmann Springer London eBook Packages, Springer-Verlag London Limited 2011 Hardcover ISBN978-1-84996-304-6 Softcover ISBN978-1-4471-5739-7 eBook ISBN978-1-84996-305-3 https://doi.org/10.1007/978-1-84996-305-3

[86] LaDisa, J.F., Jr., Alberto Figueroa, C., Vignon-Clementel, I.E., Kim, H.J., Xiao, N., Ellwein, L.M., Chan, F.P., Feinstein, J.A., Taylor, C.A., 2011a. Computational simulations for aortic coarctation: representative results from a sampling of patients. J Biomech Eng 133, 091008.

[87] Erbel, R., Aboyans, V., Boileau, C., Bossone, E., Bartolomeo, R.D., Eggebrecht, H., Evangelista, A., Falk, V., Frank, H., Gaemperli, O., Grabenwoger, M., Haverich, A., Iung, B., Manolis, A.J., Meijboom, F., Nienaber, C.A., Roffi, M., Rousseau, H., Sechtem, U., Sirnes, P.A., Allmen, R.S., Vrints, C.J., 2014. 2014 ESC Guidelines on the diagnosis and treatment of aortic diseases: Document covering acute and chronic aortic diseases of the thoracic and abdominal aorta of the adult. The Task Force for the Diagnosis and Treatment of Aortic Diseases of the European Society of Cardiology (ESC). Eur Heart J 35, 2873-2926.

[88] Coarctation of the aorta – Wikipedia https://en.wikipedia.org/wiki/Coarctation_of_the_aorta

[89] Garcia, J., Barker, A.J., Markl, M., 2019. The Role of Imaging of Flow Patterns by 4D Flow MRI in Aortic Stenosis. JACC: Cardiovascular Imaging 12, 252-266

[90] Dyverfeldt, P., Bissell, M., Barker, A. J., Bolger, A. F., Carlhäll, C. J., Ebbers, T., ... & Hope, M. D. (2015). 4D flow cardiovascular magnetic resonance consensus statement. Journal of Cardiovascular Magnetic Resonance, 17(1), 72.

[91] Harloff, A., Nußbaumer, A., Bauer, S., Stalder, A. F., Frydrychowicz, A., Weiller, C., ... &Markl, M., 2010. In vivo assessment of wall shear stress in the atherosclerotic aorta using flow sensitive 4D MRI. Magnetic Resonance in Medicine: An Official Journal of the International Society for Magnetic Resonance in Medicine, 63(6), 1529-1536.

[92] Markl, M., Schnell, S., Wu, C., Bollache, E., Jarvis, K., Barker, A. J., ... & Rigsby, C. K. (2016). Advanced flow MRI: emerging techniques and applications. Clinical radiology, 71(8), 779-795.

[93] Miyazaki, S., Itatani, K., Furusawa, T., Nishino, T., Sugiyama, M., Takehara, Y., & Yasukochi, S. (2017). Validation of numerical simulation methods in aortic arch using 4D Flow MRI. Heart and vessels, 32(8), 1032-1044.

[94] Abbas, M. Ali, Y. Q. Bai, M. M. Rashidi, And M. M. Bhatti. “Application Of Drug Delivery In Magnetohydrodynamics Peristaltic Blood Flow Of Nanofluid In A Non-Uniform Channel.” Journal of Mechanics in Medicine and Biology 16, no. 04 (June 2016): 1650052.
https://doi.org/10.1142/s0219519416500524.

[95] Human Physiology From Cells to Systems: Lauralee Sherwood seventh edition Department of Physiology and Pharmacology School of Medicine West Virginia University- USA- Brooks/Cole, Cengage Learning ISBN-10: 0-495-39184-0 (2010).

[96] Steinman, D. A. (2012). Assumptions in modelling of large artery hemodynamics. Modeling of physiological flows, 1-18.

[97] Westerhof, Nicolaas, Nikolaos Stergiopulos, Mark I.M. Noble, and Berend E. Westerhof. Snapshots of Hemodynamics. Cham: Springer International Publishing, 2019.

https://doi.org/10.1007/978-3-319-91932-4.

[98] Cho, Y. I., & Kensey, K. R. (1991). Effects of the non-Newtonian viscosity of blood on flows in a diseased arterial vessel. Part 1: Steady flows. Biorheology, 28(3-4), 241-262. https://doi.org/10.3233/BIR-1991-283-415

[99] Barnes, H. A. (1996). Rheology: Principles, Measurements and Applications: by Christopher W. Macosko, published by VCH Publishers, Weinheim, Germany, 550 pp.,£ 66.00, ISBN 1-56081-579-5.

[100] Vahidkhah, K., Balogh, P. & Bagchi, P. Flow of Red Blood Cells in Stenosed Microvessels. Sci Rep 6, 28194 (2016). https://doi.org/10.1038/srep28194

[101] SECOMB, T. W. (1992). Mechanics of blood flow in capillaries. In vitro, 1, 2.

[102] Fung, Y. C. Biomechanics: Circulation. (Springer-Verlag, 1993).

[103] D. Belkacemi, F. Piatti, M. Tahar Abbes, A. Caimi, F. Sturla, C. Geppert, D. Giese, F. Pluchinotta, M. Carminati, S. Chouaki, B. Laribi and A. Redaelli. Combined 4D Flow MRI and CFD Simulation in Aortic Coarctation. First International Conference on Innovation in Biomechanics and Biomaterials ICIBAB-2019. Oran, 10-11 Avril 2019.

[104] Al-Azawy, Mohammed Ghalib, Saleem Khalefa Kadhim, and Azzam Sabah Hameed. "Newtonian and Non-Newtonian Blood Rheology Inside a Model of Stenosis." *CFD Letters* 12, no. 11 (2020): 27-36. https://doi.org/10.37934/cfdl.12.11.2736.

[105] Pedley, T. J., and Y. C. Fung. "The Fluid Mechanics of Large Blood Vessels." Yetl.yabesh.ir, November 1, 1980. https://doi.org/10.1115/1.3138235.

[106] K. Yasuda, R.C. Armstrung; R.E. Cohen (1981) Shear flow properties of concentrated solutions of linear and shear branched polystyrenes. *Reol Acta* 20:163-178. https://doi.org/10.1007/BF01513059

[107] K, Ramakrishnan, and Shailendhra K. "Hydromagnetic Blood Flow through a Uniform Channel with Permeable Walls Covered by Porous Media of Finite Thickness." Www.sid.ir 6, no. 1 (January 1, 2013): 39–47. https://doi.org/10.36884/jafm.6.01.19479.

[108] Marrero, V. L., Tichy, J. A., Sahni, O., & Jansen, K. E. (2014). Numerical study of purely viscous non-Newtonian flow in an abdominal aortic aneurysm. Journal of biomechanical engineering, 136(10), 101001. https:// doi.org/10.1115/1.4027488

[109] Tzirakis, K., Kamarianakis, Y., Kontopodis, N., & Ioannou, C. V. (2023). Classification of Blood Rheological Models through an Idealized Symmetrical Bifurcation. Symmetry, 15(3), 630. https://doi.org/10.3390/sym15030630

[110] J. C. Weddell, J. Kwack, P. I. Imoukhuede, & A. Masud, (2015). Hemodynamic analysis in an idealized artery tree: differences in wall shear stress between Newtonian and non-Newtonian blood models. PloS one, 10(4), e0124575. https://doi.org/10.1371/journal.pone.0124575

[111] ANSYS Fluent user guide.

[112] X. He, & D.N. Ku, (1996). Pulsatile flow in the human left coronary artery bifurcation: average conditions. *Journal of biomechanical engineering*, 118(1), 74-82. https://doi.org/10.1115/1.2795948

[113] V. Peiffer, S.J. Sherwin, & P.D. Weinberg, (2013). Computation in the rabbit aorta of a new metric–the transverse wall shear stress–to quantify the multidirectional character of disturbed blood flow. *Journal of biomechanics*, *46*(15), 2651-2658.

https://doi.org/10.1016/j.jbiomech.2013.08.003

[114] H.A. Himburg, D.M. Grzybowski, A.L. Hazel, J.A. LaMack, X.M. Li, & M.H. Friedman, (2004). Spatial comparison between wall shear stress measures and porcine arterial endothelial permeability. *American Journal of Physiology-Heart and Circulatory Physiology*, 286(5), H1916-H1922. https://doi.org/10.1152/ajpheart.00897.2003

[115] Stather, P. W., D. A. Sidloff, I. A. Rhema, E. Choke, M. J. Bown, and R. D. Sayers. "A Review of Current Reporting of Abdominal Aortic Aneurysm Mortality and Prevalence in the Literature." European Journal of Vascular and Endovascular Surgery 47, no. 3 (March 1, 2014): 240–42. https://doi.org/10.1016/j.ejvs.2013.11.007.

[116] Schermerhorn, Marc. "A 66-Year-Old Man with an Abdominal Aortic Aneurysm." JAMA 302, no. 18 (November 11, 2009): 2015. https://doi.org/10.1001/jama.2009.1502.

[117] Bouferrouk, A., S. Boutamine, and A. Mekarnia. "Dépistage Opportuniste de l'Anévrisme de l'Aorte Abdominale Lors d'Une Écho-Cardiographie Transthoracique Chez Des Patients Sélectionnés : Expérience d'Un Centre Algérien." Journal Des Maladies Vasculaires 40, no. 5 (September 1, 2015): 312. https://doi.org/10.1016/j.jmv.2015.07.101.

[118] Hallin, A, D Bergqvist, and L Holmberg. "Literature Review of Surgical Management of Abdominal Aortic Aneurysm." European Journal of Vascular and Endovascular Surgery 22, no. 3 (September 1, 2001): 197–204. https://doi.org/10.1053/ejvs.2001.1422.

[119] Scheer, Margot L.J., Robert A. Pol, Jan Willem Haveman, Ignace F.J. Tielliu, Eric L.G. Verhoeven, Jan J.A.M. Van Den Dungen, Maarten W. Nijsten, and Clark J. Zeebregts. "Effectiveness of Treatment for Octogenarians with Acute Abdominal Aortic Aneurysm." Journal of Vascular Surgery 53, no. 4 (April 2011): 918–25. https://doi.org/10.1016/j.jvs.2010.10.072.

[120] McPhee, James T., Joshua S. Hill, and Mohammad H. Eslami. "The Impact of Gender on Presentation, Therapy, and Mortality of Abdominal Aortic Aneurysm in the United States, 2001-2004." Journal of Vascular Surgery 45, no. 5 (May 2007): 891–99. https://doi.org/10.1016/j.jvs.2007.01.043.

[121] Sakalihasan, N, R Limet, and OD Defawe. "Abdominal Aortic Aneurysm." The Lancet 365, no. 9470 (April 2005): 1577–89. https://doi.org/10.1016/s0140-6736(05)66459-8.

[122] Vorp, David A. "Biomechanics Of Abdominal Aortic Aneurysm." Journal of Biomechanics 40, no. 9 (2007): 1887–1902. https://doi.org/10.1016/j.jbiomech.2006.09.003.

[123] Chaikof, Elliot L., David C. Brewster, Ronald L. Dalman, Michel S. Makaroun, Karl A. Illig, Gregorio A. Sicard, Carlos H. Timaran, Gilbert R. Upchurch, and Frank J. Veith. "The Care of Patients with an Abdominal Aortic Aneurysm: The Society for Vascular Surgery Practice Guidelines." Journal of Vascular Surgery 50, no. 4 (October 2009): S2–49. https://doi.org/10.1016/j.jvs.2009.07.002.

[124] Lim, Sheh Hong, Mohd Azrul Hisham Mohd Adib, Mohd Shafie Abdullah, Nur Hartini Mohd Taib, Radhiana Hassan, and Azian Abd Aziz. "Study of Extracted Geometry Effect on Patient-Specific Cerebral Aneurysm Model with Different Threshold Coefficient (Cthres)." *CFD Letters*, 12, no. 10 (2020): 1-14.https://doi.org/10.37934/cfdl.12.10.114

[125] Vande Geest, Jonathan P., David E. Schmidt, Michael S. Sacks, and David A. Vorp. "The Effects of Anisotropy on the Stress Analyses of Patient-Specific Abdominal Aortic Aneurysms." Annals of Biomedical Engineering 36, no. 6 (April 9, 2008): 921–32. https://doi.org/10.1007/s10439-008-9490-3.

[126] Raut, Samarth S., Santanu Chandra, Judy Shum, and Ender A. Finol. "The Role of Geometric and Biomechanical Factors in Abdominal Aortic Aneurysm Rupture Risk Assessment." Annals of Biomedical Engineering 41, no. 7 (March 19, 2013): 1459–77. https://doi.org/10.1007/s10439-013-0786-6.

[127] Algabri, Y. A., Chatpun, S., & Taib, I. (2019). An investigation of pulsatile blood flow in an angulated neck of abdominal aortic aneurysm using computational fluid dynamics. Journal of Advanced Research in Fluid Mechanics and Thermal Sciences, 57(2), 265-274.

[128] Jafarzadeh, Sina, Arsalan Nasiri Sadr, Ehsan Kaffash, Sahar Goudarzi, Ehsan Golab, and Arash Karimipour. "The Effect of Hematocrit and Nanoparticles Diameter on Hemodynamic Parameters and Drug Delivery in Abdominal Aortic Aneurysm with Consideration of Blood Pulsatile Flow." Computer Methods and Programs in Biomedicine 195 (October 1, 2020): 105545. https://doi.org/10.1016/j.cmpb.2020.105545.

[129] Hegde, P., Barboza, A. B. V., Khader, S. A., Pai, R., Tamagawa, M., Prabhu, R., & Rao, D. S. (2021). Numerical Analysis on A Non-Critical Stenosis in Renal Artery. Journal of Advanced Research in Fluid Mechanics and Thermal Sciences, 88(3), 31-48. https://doi.org/10.37934/arfmts.88.3.3148

[130] Wen, Jun, Ding Yuan, Qingyuan Wang, Yao Hu, Jichun Zhao, Tinghui Zheng, and Yubo Fan. "A Computational Simulation of the Effect of Hybrid Treatment for Thoracoabdominal Aortic Aneurysm on the Hemodynamics of Abdominal Aorta." Scientific Reports 6, no. 1 (March 31, 2016).https://doi.org/10.1038/srep23801.

[131] Salsac, A.-V., S. R. Sparks, J.-M. Chomaz, And J. C. Lasheras. "Evolution of the Wall Shear Stresses during the Progressive Enlargement of Symmetric Abdominal Aortic Aneurysms." Journal of Fluid Mechanics 560 (July 20, 2006): 19. https://doi.org/10.1017/s002211200600036x.

[132] Soudah, E., G. Vilalta, M. Bordone, F. Nieto, J. A. Vilalta, and C. Vaquero. "Estudio Paramétrico de Tensiones Hemodinámicas En Modelos de Aneurismas de Aorta Abdominal." Revista Internacional de Métodos Numéricos Para Cálculo Y Diseño En Ingeniería 31, no. 2 (April 1, 2015): 106–12. https://doi.org/10.1016/j.rimni.2014.02.003.

[133] Finol, E. A., K. Keyhani, and C. H. Amon. "The Effect of Asymmetry in Abdominal Aortic Aneurysms under Physiologically Realistic Pulsatile Flow Conditions." Journal of Biomechanical Engineering 125, no. 2 (April 1, 2003): 207–17. https://doi.org/10.1115/1.1543991.

[134] Zambrano, Byron A., Hamidreza Gharahi, ChaeYoung Lim, Farhad A. Jaberi, Jongeun Choi, Whal Lee, and Seungik Baek. "Association of Intraluminal Thrombus, Hemodynamic Forces, and Abdominal Aortic Aneurysm Expansion Using Longitudinal CT Images." Annals of Biomedical Engineering 44, no. 5 (October 1, 2015): 1502–14. https://doi.org/10.1007/s10439-015-1461-x.

[135] Stefanov, Florian, Sherif Sultan, Liam Morris, Ala Elhelali, Edel P. Kavanagh, Violet Lundon, Mohamed Sultan, and Niamh Hynes. "Computational Fluid Analysis of Symptomatic Chronic Type B Aortic Dissections Managed with the Streamliner Multilayer Flow Modulator." Journal of Vascular Surgery 65, no. 4 (April 2017): 951–63. https://doi.org/10.1016/j.jvs.2016.07.135.

[136] Azriff, A., Khader, S. M. A., Pai, R., Zubair, M., Ahmad, K. A., & Prakashini, K. (2018). Haemodynamics study in subject-specific abdominal aorta with renal bifurcation using CFD-a case study. Journal of Advanced Research in Fluid Mechanics and Thermal Sciences, 50(2), 118-121.

[137] Zakaria, M. S., Ismail, F., Tamagawa, M., Azi, A. F. A., Wiriadidjaya, S., Basri, A. A., & Ahmad, K. A. (2018). Computational fluid dynamics study of blood flow in aorta using OpenFOAM. Journal of Advanced Research in Fluid Mechanics and Thermal Sciences, 43(1), 81-89.

[138] Mills, C. J., I. T. Gabe, J. H. Gault, D. T. Mason, J. Ross, E. Braunwald, and J. P. Shillingford. "Pressure-Flow Relationships and Vascular Impedance in Man." Cardiovascular Research 4, no. 4 (October 1, 1970): 405–17. https://doi.org/10.1093/cvr/4.4.405.

[139] Budwig, R., D. Elger, H. Hooper, and J. Slippy. "Steady Flow in Abdominal Aortic Aneurysm Models." Journal of Biomechanical Engineering 115, no. 4A (November 1, 1993): 418–23. https://doi.org/10.1115/1.2895506.

[140] Deplano, Valerie, Yannick Knapp, Eric Bertrand, and Emmanuel Gaillard. "Flow Behaviour in an Asymmetric Compliant Experimental Model for Abdominal Aortic Aneurysm." Journal of Biomechanics 40, no. 11 (January 2007): 2406–13. https://doi.org/10.1016/j.jbiomech.2006.11.017.

[141] Jeong, Jinhee, and Fazle Hussain. "On the Identification of a Vortex." Journal of Fluid Mechanics 285 (February 1, 1995): 69–94. https://doi.org/10.1017/S0022112095000462.

[142] Formaggia, Luca, Alfio Quarteroni, and Allesandro Veneziani. Cardiovascular Mathematics: Modeling and Simulation of the Circulatory System. Google Books. Springer Science & Business Media, 2010.
https://books.google.com/books?hl=fr&lr=&id=BQpm2VDN3kcC&oi=fnd&pg=PR5&dq=Formaggia

[143] Qiu, Yue, Ding Yuan, Jun Wen, Yubo Fan, and Tinghui Zheng. "Numerical Identification of the Rupture Locations in Patient-Specific Abdominal Aortic Aneurysmsusing Hemodynamic Parameters." Computer Methods in Biomechanics and Biomedical Engineering 21, no. 1 (December 18, 2017): 1–12. https://doi.org/10.1080/10255842.2017.1410796.

[144] DA SILVA, Erasmo Simão, Aldo Junqueira RODRIGUES, Erasmo Magalhães Castro DE TOLOSA, Consuelo Junqueira RODRIGUES, Gladys Villas Boas DO PRADO, and João Carlos Nakamoto. "Morphology and Diameter of Infrarenal Aortic Aneurysms: A Prospective Autopsy Study." Cardiovascular Surgery 8, no. 7 (December 1, 2000): 526–32. https://doi.org/10.1016/S0967-2109(00)00060-0.

[145] Kelsey, Lachlan J., Janet T. Powell, Paul E. Norman, Karol Miller, and Barry J. Doyle. "A Comparison of Hemodynamic Metrics and Intraluminal Thrombus Burden in a Common Iliac Artery Aneurysm." International Journal for Numerical Methods in Biomedical Engineering 33, no. 5 (September 8, 2016): e2821. https://doi.org/10.1002/cnm.2821.

[146] D.A. Vorp, M.L. Raghavan, & M.W. Webster, (1998). Mechanical wall stress in abdominal aortic aneurysm: influence of diameter and asymmetry. *Journal of vascular surgery*, 27(4), 632-639. https://doi.org/10.1016/S0741-5214(98)70227-7

[147] A. Karthikesalingam, A. Vidal-Diez, P.J. Holt, I.M. Loftus, M.L. Schermerhorn, P.A. Soden, ... & M.M. Thompson, (2016). Thresholds for abdominal aortic aneurysm repair in England and the United States. *New England Journal of Medicine*, 375(21), 2051-2059.
https://doi.org/10.1056/NEJMoa1600931

[148] A. Updegrove, N.M. Wilson, J. Merkow, H. Lan, A.L. Marsden, & S.C. Shadden, (2017). SimVascular: an open source pipeline for cardiovascular simulation. *Annals of biomedical engineering*, *45*(3), 525-541. https://doi.org/10.1007/s10439-016-1762-8

[149] N.B. Wood, (1999). Aspects of fluid dynamics applied to the larger arteries. *Journal of theoretical biology*, *199*(2), 137-161. https://doi.org/10.1006/jtbi.1999.0953

[150] E.S. Di Martino, A. Bohra, J.P.V. Geest, N. Gupta, M.S. Makaroun, & D.A. Vorp, (2006). Biomechanical properties of ruptured versus electively repaired abdominal aortic aneurysm wall tissue. *Journal of vascular surgery*, *43*(3), 570-576. https://doi.org/10.1016/j.jvs.2005.10.072

[151] M.L. Raghavan, J. Kratzberg, de E.M.C. Tolosa, M.M. Hanaoka, P. Walker, & da E.S. Silva, (2006). Regional distribution of wall thickness and failure properties of human abdominal aortic aneurysm. *Journal of biomechanics*, *39*(16), 3010-3016. https://doi.org/10.1016/j.jbiomech.2005.10.021

[152] Y. Wang, K. Luo, Y. Qiao, & J. Fan, (2021). An integrated fluid-chemical model toward modeling the thrombus formation in an idealized model of aortic dissection. *Computers in Biology and Medicine*, 136, 104709. https://doi.org/10.1016/j.compbiomed.2021.104709

[153] R. Perinajová, J.F. Juffermans, J.J. Westenberg, R.L. van der Palen, P.J. van den Boogaard, H.J. Lamb, & S. Kenjereš, (2021). Geometrically induced wall shear stress variability in CFD-MRI coupled simulations of blood flow in the thoracic aortas. *Computers in Biology and Medicine*, 133, 104385.https://doi.org/10.1016/j.compbiomed.2021.104385

[154] C.H. Armour, B. Guo, S. Saitta, S. Pirola, Y. Liu, Z. Dong, & X.Y. Xu, (2022). Evaluation and verification of patient-specific modelling of type B aortic dissection. *Computers in Biology and Medicine*, 140, 105053. https://doi.org/10.1016/j.compbiomed.2021.105053

[155] F. Joly, G. Soulez, D. Garcia, S. Lessard, & C. Kauffmann, (2018). Flow stagnation volume and abdominal aortic aneurysm growth: Insights from patient-specific computational flow dynamics of Lagrangian-coherent structures. *Computers in biology and medicine*, 92, 98-109. https://doi.org/10.1016/j.compbiomed.2017.10.033

[156] A.S. Les, J.J. Yeung, G.M. Schultz, R.J. Herfkens, R.L. Dalman, & C.A. Taylor, (2010). Supraceliac and infrarenal aortic flow in patients with abdominal aortic aneurysms: mean flows, waveforms, and allometric scaling relationships. *Cardiovascular engineering and technology*, *1*(1), 39-51. https://doi.org/10.1007/s13239-010-0004-8

[157] D.B. McClarty, D.C. Kuhn, & A.J. Boyd, (2021). Hemodynamic Changes in an Actively Rupturing Abdominal Aortic Aneurysm. *Journal of Vascular Research*, *58*(3), 172-179. https://doi.org/10.1159/000514237

[158] U. Morbiducci, D. Gallo, D. Massai, F. Consolo, R. Ponzini, L. Antiga, ... & A. Redaelli, (2010). Outflow conditions for image-based hemodynamic models of the carotid bifurcation: implications for indicators of abnormal flow. Journal of biomechanical engineering, 132(9). https://doi.org/10.1115/1.4001886

[159] N. Kaewchoothong, Y.A. Algabri, T. Assawalertsakul, C. Nuntadusit, & S. Chatpun, (2022). Computational Study of Abdominal Aortic Aneurysms with Severely Angulated Neck Based on Transient Hemodynamics Using an Idealized Model. Applied Sciences, 12(4), 2113. https://doi.org/10.3390/app12042113

[160] T. Suess, J. Anderson, L. Danielson, K. Pohlson, T. Remund, E. Blears, ... & P. Kelly, (2016). Examination of near-wall hemodynamic parameters in the renal bridging stent of various stent graft configurations for repairing visceral branched aortic aneurysms. *Journal of vascular surgery*, *64*(3), 788-796. https://doi.org/10.1016/j.jvs.2015.04.421

[161] P.J. Roache, (1998). Verification and validation in computational science and engineering (Vol. 895, p. 895). Albuquerque, NM: Hermosa.

[162] E. Tedaldi, , C. Montanari, , K.I. Aycock, , F. Sturla, , A. Redaelli, , & K.B. Manning, (2018). An experimental and computational study of the inferior vena cava hemodynamics under respiratory-induced collapse of the infrarenal IVC. *Medical Engineering & Physics*, *54*, 44-55. https://doi.org/10.1016/j.medengphy.2018.02.003

[163] LaDisa Jr, J. F., Taylor, C. A., & Feinstein, J. A. (2010). Aortic coarctation: recent developments in experimental and computational methods to assess treatments for this simple condition. Progress in pediatric cardiology, 30(1-2), 45-49.

[164] : Stankovic, Z., Allen, B. D., Garcia, J., Jarvis, K. B., & Markl, M. (2014). 4D flow imaging with MRI. Cardiovascular diagnosis and therapy, 4(2), 173–192.

[165] Piatti, F., Sturla, F., Bissell, M. M., Pirola, S., Lombardi, M., Nesteruk, I., ... & Votta, E. (2017). 4D flow analysis of BAV-related fluid-dynamic alterations: Evidences of wall shear stress alterations in absence of clinically-relevant aortic anatomical remodeling. Frontiers in physiology, 8, 441.

[166] Piatti, F., Pirola, S., Bissell, M., Nesteruk, I., Sturla, F., Della Corte, A., ... & Votta, E., 2017c. Towards the improved quantification of in vivo abnormal wall shear stresses in BAV-affected patients from 4D-flow imaging: Benchmarking and application to real data. Journal of biomechanics, 50, 93-101.

[167] https://en.wikipedia.org/

[168] S. K. Atkins et al., “Bicuspid aortic valve hemodynamics induces abnormal medial remodeling in the convexity of porcine ascending aortas”, Biomech Model Mechanobiol, 2014, 13: pp. 1209-1225

[169] Annio, G., Torii, R., Ariff, B., O'Regan, D. P., Muthurangu, V., Ducci, A.,& Burriesci, G., 2019. Enhancing Magnetic Resonance Imaging With Computational Fluid Dynamics. Journal of Engineering and Science in Medical Diagnostics and Therapy, 2(4).

[170] Bauer, A., Wegt, S., Bopp, M., Jakirlic, S., Tropea, C., Krafft, A. J., ...& Egger, H., 2019. Comparison of wall shear stress estimates obtained by laser Doppler velocimetry, magnetic resonance imaging and numerical simulations. Experiments in Fluids, 60(7), 112.

[171] Bauer, A., Bopp, M., Jakirlic, S., Tropea, C., Krafft, A. J., Shokina, N., & Hennig, J., 2020.Analysis of the wall shear stress in a generic aneurysm under pulsating and transitional flow conditions. Experiments in Fluids, 61(2), 59.

[172] Callaghan, F. M., & Grieve, S. M., 2018. Normal patterns of thoracic aortic wall shear stress measured using four-dimensional flow MRI in a large population. American Journal of Physiology-Heart and Circulatory Physiology, 315(5), H1174-H1181.